Strål säkerhets myndigheten
Swedish Radiation Safety Authority

Author: Björn Thunell
Scanscot Technology AB, Lund

Research

2018:17

Assessment of structures subject to concrete pathologies (ASCET), phase 2

SSM perspective

Background

ASCET is an international research project initiated by WGIAGE[1] OECD[2] / NEA[3]. WGIAGE[4] Concrete subgroup is a working group within the OECD / NEA whose task is to address issues concerning

- the maintenance of the integrity of concrete structures,

- proposals for general principles to optimally handle the challenges of integrity, especially with regard to aging of concrete structures.

The aim of the ASCET project is to create a basis for general recommendations regarding management of ageing related concrete degradation in nuclear facilities.

Results

Phase 2 of the ASCET project consisted of a blind numerical simulation benchmark of a shear wall structure affected by concrete degradation, in this case ASR , tested under cyclic loading up to structural failure. The numerical simulations have been compared with experimental results. The numerical result revealed for example that the shear friction capacity, calculated as per section 6.2.5 in EC2, exceeds the experimentally derived capacity of the studied wall. The numerical simulation confirmed that structures effected by ASR can have a higher ultimate shear capacity despite having nominally weaker material properties. That is because the concrete expansion caused by ASR is prevented due to the concrete reinforcement.

The results from this phase is important in order to create a basis for general recommendations regarding management of ageing related concrete degradation in nuclear facilities.

Objectives

Degradation of concrete structures important to safety has been identified by SSM as a potential problem area as the Swedish nuclear facilities are getting older. The results from this research project together with the next phase are therefore valuable when it comes to ageing management and radiation safety assessments of degraded concrete structures in nuclear facilities.

Need for further research

Further research is performed in ASCET phase 3 where numerical simulations will be performed with access to previous experimental results. The aim of ASCET is to provide comprehensive recommendations for numerical simulations of concrete degradation mechanisms.

---

[1] Working Group on Integrity and Ageing of Components and Structures
[2] Organization for Economic Co-operation and Development
[3] Nuclear Energy Agency
[4] Alkali-silica reactions

Project information
Contact person SSM: Sofia Lillhök
Reference: SSM 2015-1013 / 7030051-00

Strål säkerhets myndigheten

Swedish Radiation Safety Authority

Author: Björn Thunell
Scanscot Technology AB, Lund

2018:17

Assessment of structures subject to concrete pathologies (ASCET), phase 2

This report concerns a study which has been conducted for the Swedish Radiation Safety Authority, SSM. The conclusions and viewpoints presented in the report are those of the author/authors and do not necessarily coincide with those of the SSM.

Executive summary

This report summarizes the work carried out by the independent consultancy company Scanscot Technology within the framework of Phase 2 of the OECD/NEA/CSNI CAPS called ASCET.

The ASCET (Assessment of Nuclear Structures Subject to Concrete Pathologies) initiative aims to create a basis for general recommendations regarding management of ageing related issues in nuclear facilities exposed to concrete pathologies (material degradation mechanisms). This subject is of great interest for the nuclear industry internationally, as concrete degradation mechanisms (e.g. alkali-aggregate reaction, delayed ettringite formation, irradiated concrete, sulfate attack, rebar steel corrosion, freezing and thawing cycles) have been detected in nuclear facilities in several OECD member states [1], and might very likely affect structural performance and residual lifetime in the future. The content of the ASCET Phase 2 benchmark is a blind numerical simulation benchmark of a shear wall structure affected by alkali-silica reactions (ASR), tested under cyclic loading, up to structural failure [2]. Several specimens with different levels of advanced ASR, as well as reference specimens with sound aggregate, were experimentally tested to compare the ultimate capacity, displacements and failure modes.

The final purpose of the work documented in this report aim at ensuring safe Long Term Operation of Nuclear Power Plants. The focus area is primarily safety-related issues regarding nuclear reactor containments, and the work is based on national research needs in Sweden [3]. The main incentive to involve in projects like this is in the end for the purpose of structural assessments. The objective being to maintain stipulated safety criteria, taking eventual ageing effects, and actual conditions into account. In practice, this transfers to a need to evaluate the structural capacity compared to safety criteria for accidental design, and beyond design, loading conditions. The question of how margins change when ageing effects are considered, or if some sort of anomaly or defect is found, is therefore pursued.

The general-purpose finite element program ABAQUS [4] was used for the numerical simulations summarized in this report. Simulation results were compared against available experimental results from shear wall specimens loaded primarily in shear. In summary, numerical results from the blind phase of the benchmark revealed that:

1. The concrete damaged plasticity material model in ABAQUS proved reasonably appropriate for numerical simulation of the studied squat reinforced concrete wall loaded in shear, for monotonic loads, as experimentally determined shear capacity compare well to simulation results.
2. Numerical simulation results confirm the experimental observation that the ASR affected specimen, although having nominally weaker material properties, may possess a higher ultimate shear capacity than a regular structure, due to confining effects resulting from the concrete material expansion.
3. For the studied reinforced concrete wall, it is concluded that shear friction code equation capacity, calculated per section 6.2.5 in EC2,

exceeds the experimentally derived shear capacity of the studied wall.

Sammanfattning

Allt fler kärnkraftverk runt om i världen närmar sig just nu skedet långtidsdrift av sin operativa fas. Som ett resultat har hantering av åldersrelaterade fenomen blivit en viktig fråga i kärnkraftsindustrin.

Programmet ASCET (Assessment of Nuclear Structures Subject to Concrete Pathologies) initierades av WGIAGE OECD/NEA/CSNI under 2013 och är ett internationellt forskningsprogram inriktat på nedbrytningsmekanismer av kompositen armerad betong i kärntekniska anläggningar. Programmet syftar till att skapa en grund för allmänna råd för hantering av åldrandefrågor för betongkonstruktioner i kärntekniska anläggningar som utsätts för nedbrytningsmekanismer av materialet. Forskningsprogrammet fokuserar speciellt på frågeställningar kring alkali-silika reaktioner (ASR). Målet är att på sikt kunna ge rekommendationer för degraderingarnas kapacitetsförändring av materialet. Den typ av utredningar som krävs för att förstå och utvärdera betongens förhållanden bestäms av varje medlemsland baserad på forskningsbehov och identifierad känslighet för skador.

Denna rapport sammanfattar det oberoende konsultföretaget Scanscots bidrag till ASCET-programmets fas 2, vilken utgörs av ett internationellt benchmarkprojekt som innefattar numeriska simuleringar av en skjuvväggskonstruktion belastad med cyklisk last.

Det officiella syftet med programmet är att studera degraderade (ASR/AAR) betongkonstruktioners beteende under starkt olinjär och cyklisk last (jordbävning). Detta område bedöms mindre intressant för svenska förhållanden, eftersom svenska kärnkraftverk inte rapporterats skadade av ASR [5]. Vinklingen undersöks, men tonvikten inom projektet ligger på att undersöka förmåga att simulera oskadade (normala) betongkonstruktioner som utsätts för cyklisk skjuvande belastning och svarar med olinjär respons i materialet. Detta för att kunna tillgodose de behov svensk myndighet och anläggningsägare kan komma att ha.

Sammanfattningsvis visade numeriska resultat att:

1. Använd materialmodell (Concrete Damage Plasticity) i programmet ABAQUS visade sig vara relativt väl lämpad för simulering av de studerade skjuvbelastade betongväggarna, för monotoniska belastningar.
2. Numeriska simuleringsresultat bekräftar experimentella observationer som visar att struktur påverkad av ASR kan, trots nominellt svagare materialegenskaper, kan ha en högre skjuvkrafts-överförande kapacitet än en normal struktur. Detta tillskrivs de omslutningseffekter på grund av materialets expansion som uppstår då expansionen förhindras (här genom armeringen).
3. För den studerade betongväggen överskattas skjuvkapaciteten, beräknad enligt avsnitt 6.2.5 i Eurocode 2, jämfört med resultat från experimentella tester.

Content

Nomenclature

d_t	concrete tension damage [-]
E	modulus of elasticity [MPa]
E_0	initial modulus of elasticity used in ABAQUS [MPa]
f_c	compressive cylinder strength of concrete [MPa]
f_{ck}	characteristic compressive cylinder strength of concrete [MPa]
f_{cm}	mean value of concrete cylinder compressive strength [MPa]
$f_{c,cube}$	compressive cube strength of concrete [MPa]
$f_{ck,cube}$	characteristic compressive cube strength of concrete [MPa]
$f_{cm,cube}$	mean value of concrete cube compressive strength [MPa]
f_{ct}	tensile strength of concrete [MPa]
f_{ctk}	characteristic tensile strength of concrete [MPa]
f_{ctm}	mean value of tensile strength of concrete [MPa]
G_F	fracture energy [N/m]
u_t^{ck}	cracking displacement [m]
u_{t0}^{ck}	cracking displacement at which complete loss of strength takes place [m]
ϵ	flow potential eccentricity used in ABAQUS
ε_c	total strain [-]
ε_{0c}^{el}	elastic strain corresponding to undamaged material [-]
ε_c^{in}	inelastic strain [-]
ε_{max}	maximum strain [-]
μ	viscosity parameter or coefficient of friction [-]
ν	Poisson's ratio [-]
ψ	dilation angle [deg]
ρ	density [kg/m^3]
σ_{cu}	ultimate compressive stress used in ABAQUS [MPa]
σ_{c0}	uniaxial initial compressive yield stress used in ABAQUS [MPa]

σ_{b0} initial equibiaxial compressive yield stress used in ABAQUS [MPa]

σ_{t0} failure stress in tension used in ABAQUS [MPa]

List of acronyms

AAR	Alkali Aggregate Reaction
ASCET	Assessment of Nuclear Structures Subject to Concrete Pathologies
ASR	Alkali Silica Reaction
CAPS	CSNI Activity Proposal Sheet (OECD)
CDP	Concrete Damaged Plasticity (ABAQUS)
CEA	Alternative Energies and Atomic Energy Commission (France)
CNSC	Canadian Nuclear Safety Commission
CRP	Co-ordinated Research Programme/Projects
CSNI	Committee on the Safety of Nuclear Installations (OECD)
DEF	Delayed Ettringite Formation
EDF	Electricity of France
IAEA	International Atomic Energy Agency
IRSN	Radioprotection and Nuclear Safety Institute (France)
LTO	Long Term Operation
NEA	Nuclear Energy Agency (OECD)
NPP	Nuclear Power Plant
OECD	Organization for Economic Co-operation and Development
ORNL	Oak Ridge National Lab (USA)
RC	Reinforced Concrete
SSC	Systems, Structures and Components
SSM	Swedish Radiation Safety Authority (Sweden)
STUK	Radiation and Nuclear Safety Authority (Finland)
VTT	Technical Research Centre of Finland
WGIAGE	Working Group on Integrity and Ageing of Components and Structures

x

1. Introduction

1.1. Background of the ASCET CAPS

Many Nuclear Power Plants (NPP) around the world are at the moment approaching, or in, their Long-Term Operation (LTO) stage of their operational life time. In addition, several NPPs have recently been carrying out uprate and life extension projects and comprehensive maintenance work including the exchange of components important to safety, in order to extend their lifetime. As a result, ageing management has emerged as one of the main concerns of the nuclear community.

For concrete structures, material degradation due to Alkali Aggregate Reactions (AAR) is one focus area. Concrete swelling is a consequence of several concrete degradation mechanisms of concrete structures (alkali aggregate reaction, delayed ettringite formation, irradiated concrete) and it is important to asses and to quantify the ultimate and serviceability limit states of structures built with such a concrete. The chemical reactions are concluded to be reasonably well understood [2], however the changes in structural mechanical properties, and implications for structural assessments, are yet to be established. At present time, neither established industry standards, nor regulatory requirements, address this type of material degradation. In particular, in the case of concrete with degradation mechanisms, current design code equations, using material properties based on concrete samples, are not in accordance with structural element testing [1].

In addition, there is a need for reliable numerical tools to predict the structural behavior of structures with concrete degradation mechanisms. There is also a need to establish recommendations for reliable numerical simulations of concrete structures, with and without concrete material degradations, up to the load level leading to structural failure [1]. This information is essential in order to get high level of confidence in simulation for load levels lower than failure level. Developing guidelines on numerical modelling of reinforced concrete structures loaded in shear, for the purpose of structural verification, is consequently of interest. Therefore, validation of numerical models should be performed using structural testing. In many cases reduced scale test structures cannot provide correct information related to the full-scale structures in normal conditions, therefore it is necessary to continue with both reduced and full scale testing. In addition, there is a need for model validation and quantification of uncertainties in input data and the results.

The ASCET (Assessment of Nuclear Structures Subject to Concrete Pathologies) CAPS were proposed by the OECD/NEA/CSNI in 2013, and is an international research initiative targeted at degradation of the concrete material in nuclear facilities. The ASCET initiative aims to create a basis for general recommendations regarding management of ageing issues in nuclear facilities exposed to concrete pathologies (material degradation mechanisms). The type of investigations necessary to understand and

evaluate relevant concrete degradations are determined by each member country, based on research needs and damage sensitivity. To survey member status and needs in the area of concrete pathologies, an initial phase of the ASCET initiative were dedicated to summarize current situation [1]. The safety significance of the CAPS is described as: "Determination of the impact of concrete degradation on serviceability and ultimate limit state of nuclear facilities taking into account long term operation, especially containment structures and interim storage buildings." The ASCET lead and coordination organizations are the Canadian Nuclear Safety Commission (CNSC) and the United States Nuclear Regulatory Commission (US NRC). The CSNI technical goals covered are; to promote the safe operation of current nuclear installations; to understand and quantify the mechanisms of ageing of components and structures; to assess and predict their impact on the safety of nuclear installations and; to identify the corresponding means of detection and control.

1.2. Aim and scope of ASCET Phase 2

Following the initial phase of ASCET, a second phase was proposed to serve as a blind simulation benchmark for validation of numerical models to be used in assessments of AAR affected structures.

An experimental campaign, including several nominally identical shear wall specimens with various stages of advanced AAR, were manufactured and tested at the University of Toronto. The aim was assessing effects of Alkali-Silica Reactions on in-plane shear resistance of reinforced concrete walls. The experimental campaign was carried out as a part of a CNSC financed research program. The same transverse cyclic loading (simulating horizontal seismic loading), up to the wall failure, were applied to all of the structures. Reference wall specimens with regular concrete were tested as well, in order to compare the ultimate capacity, displacements and failure modes.

The goal of the ASCET Phase 2 benchmark is to predict the behavior, in terms of force versus displacement curve and ultimate capacity, of the walls tested after 30 months of accelerating curing. The blind predictions will be based on the experimental data from the wall specimens tested at age 8 months.

Programme goals of the Phase 2 benchmark is to study;

1) ability to predict the behavior of concrete elements with ASR,
2) the difference in failure modes between ASR and sound specimen,
3) the difference in ultimate shear capacity,
4) the difference in ultimate displacements.

The expected results and deliverables of the ASCET Phase 2, from participating teams in the simulation benchmark, is a series of simulations using a range of approaches and software. The ASCET initiative will summarize the results, and provide recommendation for numerical simulation of concrete pathologies/degradation mechanisms, which result in concrete swelling as a function of time, based on the deliverables of the benchmark teams. ASCET Phase 2 participants (individuals and

organizations) include IAGE member/organizations including CNSC, US NRC, IRSN, EDF, CEA, STUK, VTT, ORNL, and Scanscot Technology.

1.3. Aim and scope of this report

The primary aim of the work summarized in this report is to, from a Swedish nuclear industry need perspective, study the behavior of a reinforced concrete squat wall affected by shear load. The term squat is here used as the studied walls has low height to width ratio. A secondary aim is to do this for concrete having degraded mechanical material properties, which here means ASR reactive concrete. The motivation for decreased interest of the official ASCET aim, given in section 1.2, is given in section 1.5. A third aim of this work is to increase the understanding of how structural assessment of the ultimate capacity of squat reinforced concrete walls can be performed, using the chosen example structure. Issues of particular interest are major contributing circumstances to the structural capacity. An additional outcome of this work is comparisons of experimental results to selected relevant design codes.

Main activities within the participation of the ASCET Phase 2 benchmark have included;

1. Material issues concerning degraded concrete, including relationships of structural capacity compared to regular concrete.
2. Structural issues including evaluation of structural performance compared to regular concrete.
3. Summarize the experimental data given to the benchmark participants, and estimate of actual conditions at the experimental tests.
4. Numerical simulations of the experiments carried out.

The main purpose of the simulations performed is to study how well the used numerical method may simulate and predict the example shear wall problem chosen for the University of Toronto experiments. Comparisons and sensitivity studies related to existing design codes, for regular concrete, are also considered important.

The scope of the numerical simulations in this report are limited to macro scale finite element analyses. The term macro scale is used here to describe that concrete material properties are set as static input, and not derived in the simulations through an evolution of chemical changes over time, due to the environmental conditions. The reason for this approach is due to the fact that treating material properties as more or less predefined values is the standard procedure used by engineers in a design or requalification process. The numerical tool used within this work is the explicit ABAQUS solver [4].

1.4. Numerical modelling of squat concrete walls

For safety related concrete structures, ultimate capacity predictions of shear loaded walls may be of interest in assessments of severe earthquakes with low probability of occurrence. The structural response of squat reinforced concrete walls is complex, and numerical modelling of such structures

subjected to primary shear loading is still an open research area. Experimental research in this area have been active for several decades, often in combination with cyclic (seismic) loading. Numerical simulations of nonlinear responses of shear wall structures are still partly without established consensus, mainly due to a combination of very little structural ductility, in combination with nonlinear concrete material modeling challenges, and important and complex interactions between the concrete and the reinforcement.

A large part of this report is dedicated to sensitivity studies, and comparisons between numerical simulations and experimental data, with the final purpose to aid in developing guidelines for use of the numerical engineering tools in structural assessments.

1.5. AAR from a Swedish nuclear safety perspective

The effects of AAR on the concrete material, as well as structural capacity effects, are currently active research areas, and have been so for many years for large scale structures as roads, bridges and dams. Very few documented applications on safety significant nuclear type of structures [6], experimental structures [7], numerical studies [8], and summary reports [9] on the effects from this material degradation are however publicly available. The focus area of the work presented within this report is ultimate structural capacity, however in real structures effects on durability may be very important.

For Swedish conditions, compiled operational experiences [5] for nuclear reactor containments include only one instance of confirmed ASR, which was found at the decommissioned Barsebäck NPP. As a consequence, with current knowledge, AAR related problems are likely of no practical concern for nuclear reactor containments in Sweden. However, LTO programs aiming at concrete material assessments are currently being implemented, and historically reported instances of degraded concrete material to the regulator are few. In addition, concrete material property changes over time are natural processes, and degradation processes may exist or develop. The studies carried out on degradations of the concrete material, and the reinforced concrete composite, within the ASCET program are therefore interesting from a Swedish nuclear industry safety perspective. A continued observation of international activity and development within this field is therefore relevant for nuclear safety.

2. Laboratory shear wall experiments

2.1. Introduction

In this chapter information given to the ASCET Phase 2 benchmark participants concerning the experimental tests, carried out at the University of Toronto, are compiled. The official ASCET documents describing the tests were originally limited to [10], [11], and [12]. In addition, complementary information, from other referenced sources, and SMiRT-23 Transactions [2], [13], [14] and [15], are also included.

The laboratory test program conducted at the University of Toronto, aiming at assessing ASR effects on in-plane shear resistance of squat reinforced concrete (RC) walls, were financed by the Canadian Nuclear Safety Commission (CNSC), according to [7]. The test program included three main components; The material aspect of ASR, the structural aspect, and non-destructive testing possibilities. Squat RC shear walls are a typical structural element in nuclear facilities. Focus areas for the test program included destructive and non-destructive testing. The wall design, with barbells as boundary elements, were chosen based on previously performed tests in order to obtain a known failure mechanism. The walls are designed using code equations for shear-friction to obtain the failure through the wall, and to avoid failure on the wall and beam interface. The aim of the destructive testing was to determine mechanical characteristics such as;

1) ultimate resistance,
2) ultimate displacement,
3) ductility,
4) residual strength of walls with AAR (compared to sound walls), and
5) to correlate the level of damage in terms of crack spacing and crack width with the structural drift.

2.2. Shear wall specimens

Within the test program conducted at the University of Toronto, six nominally identical concrete walls were constructed [2]. The wall was designed using the French BAEL design code, and the experimental test specimens used are in reduced geometric scale. Two walls were originally to be tested at each of the three different points in time selected. Three of the walls were made from normal concrete, in order to be reference walls, and three were designed to study the effects of ASR, to be tested at three different reaction stages, see Table 2-1. The information in the table is compiled from the available sources of information, and may be different from the actual chain of events. For 5 specimens only have test time specifications been found.

The initial tests, named A-tests, were carried out after approximately 8 months after casting. The last two tests, named B-tests, were performed at

the expected time of the ASR reaction to be exhausted, after approximately 31 months of accelerated ageing. The damaged walls with exhausted reaction were then planned to be retrofitted using carbon fibers, and tested again using destructive and non-destructive examinations to assess the effectiveness of the retrofit measures. Retrofit measures are outside the scope of the ASCET Phase 2 benchmark.

Table 2-1 **Test series and age of 5 of the 6 test specimens according to [2], and informal information. Testing times mentioned in [2] seem to have been revised.**

Test	Description	Time (after casting) tested
A	REG A; Control specimen	240 days (in 2014)
	ASR A1; ASR reactive concrete specimen (Initial damage)	260 days (in 2014)
B	ASR B1; ASR reactive concrete specimen (Moderate damage)	615 days (in 2016)
	ASR B2; ASR reactive concrete specimen (Severe damage, exhausted reaction)	985 days (in 2017)
	REG B; Control specimen	985 days (in 2017)

Test specimens consist of the central wall of primary interest, stabilizing end columns, and bottom and top massive beams for anchoring of floor support and jack equipment. The central wall is 100 mm thick. Geometric dimensions of the test specimen are visualized in Figure 2-1. Construction sequence, if any, and division into casting parts, is unknown.
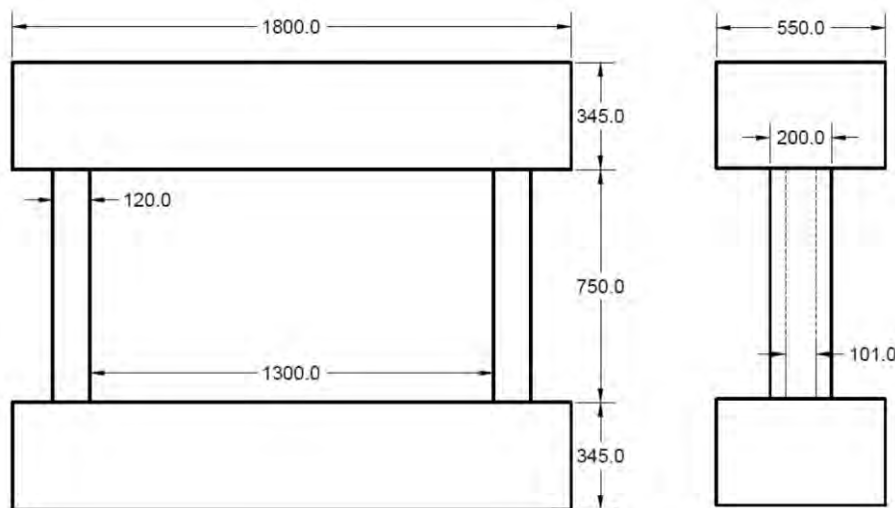
Figure 2-1 **Shear wall test specimen geometry [10].**

2.3. Concrete material properties

According to [10] and [7], small size concrete test specimens cast at the same time as the larger test wall specimens included; concrete cylinders (42), bending prisms (6), dog bone specimens (12), and expansion prisms (6). Mechanical properties of the concrete are shown in Table 2-2. The regular concrete material is concluded to, in all measured aspects (stiffness, and compressive and tensile strength), have superior mechanical properties to the ASR reactive concrete in these material tests. Figure 2-2 show concrete properties evolution of time.

Mix design for concrete walls are described in [12]. Concrete mix design was required to be based at ASTM C1293, with maximum aggregate size 19 mm. However, no actual aggregate curves are available from the concrete supplier [12]. Cement content for all concretes were 420 kg/m^3, with a w/c ratio of 0.44 and 0.46 for the ASR and regular concrete.

In using the material properties of the ASR concrete from the small test specimens listed here for the purpose of numerical simulations, it must be remembered that properties of the concrete are affected by the level of confinement, which is not included in Table 2-2Table nor Figure 2-2.

Table 2-2 **Measured mechanical properties of small size concrete specimens [11], casted simultaneously as the REG A and ASR A1 shear wall specimens[1).]**

Specimen / Type of test	Type of test specimen	REG A	ASR A1
Age (Days)	-	240	260
Compressive strength (MPa)	100 x 200 mm cylinder	79.0	63.7
Tensile strength (MPa)	Dog bone	4.76	3.24
Fracture energy (N/m)	Dog bone	179.3	120.2
Modulus of rupture (MPa)	150 x 150 x 520 mm According to ASTM-C78	7.26	4.64
Modulus of elasticity (GPa)	100 x 200 mm cylinder	47.15	35.75
Expansion (Length change in %)	75 x 75 x 285 mm According to ASTM-C1260	0.0332	0.185

[1)] Information obtained after the final benchmark workshop via [16] include the measured compressive strength for the REG B specimen (80.1 MPa), the ASR B1 specimen (67.1 MPa), and the ASR B2 specimen (63.0 MPa).
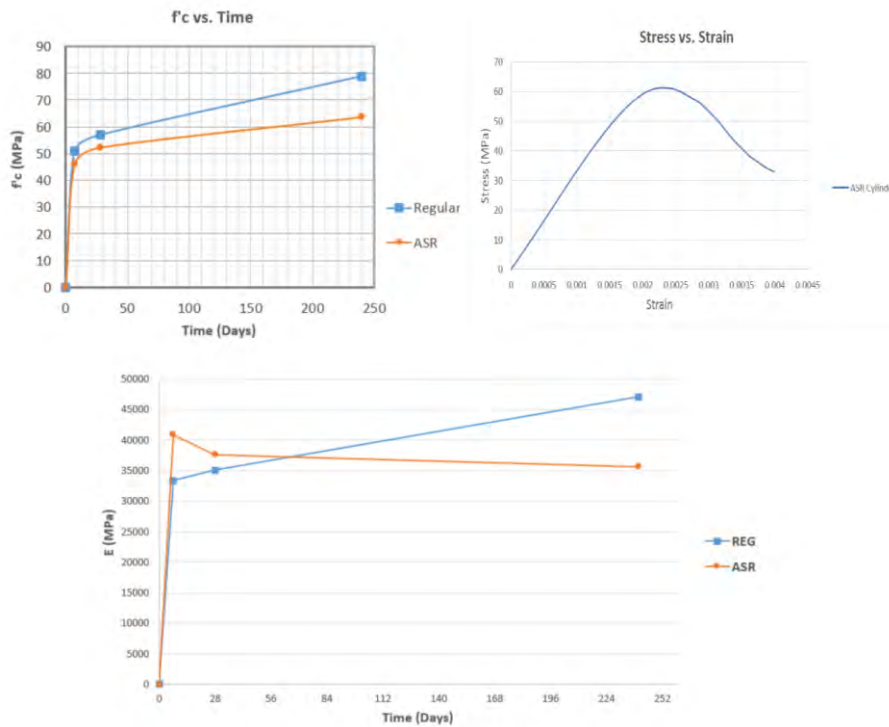
Figure 2-2   Concrete properties evolution over time [17].

2.3.1. Environmental curing conditions

Up to 28 days after casting the walls were assumed to be exposed to temperature 20 °C and relative humidity 100 % [17]. After that ASR walls were subjected to accelerated conditions in a specially built environmental chamber with temperature 50 °C and 95 % - 100 % relative humidity, see Figure 2-3. Figure 2-4 and Table 2-3 show delivered data of measured free swelling for small, unconfined, concrete samples. Table 2-1 list testing times, after casting, for the different specimens.

Figure 2-3   ASR test specimens in the acceleration chamber with increased temperature and humidity [16].

Table 2-3   Measured free swelling of small concrete samples [10].

Days	Free swelling of reactive (ASR) concrete (%)	Free swelling of regular (control) concrete (%)
0	0	0
7	0.0099	0.0181
28	0.0332	0.0249
90	0.1115	0.0264
150	0.1399	0.0309
180	0.1519	0.0329
250 (Day of testing for REG A and ASR A1)	0.1850	0.0332
610 (Day of testing for ASR B1 specimen)	0.215[1]	N/A
995 (Day of testing for REG B and ASR B2)	0.223[1]	0.0331[1]

[1] Information obtained after final benchmark workshop [16].
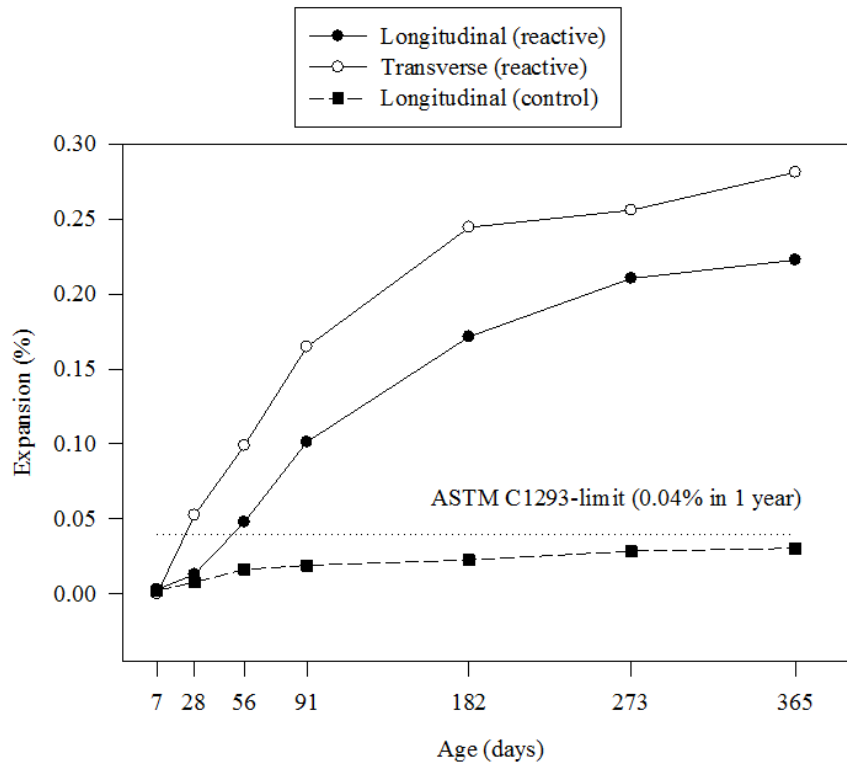
Figure 2-4   Measured free swelling of small concrete samples [17]. Reactive in the figure legend refer to ASR samples, and control to regular concrete samples.

2.4. Reinforcement steel properties

Steel reinforcement in the shear wall test specimen central wall include one, centered, layer of M10 grid reinforcement [10], spaced at 140 mm both vertically and horizontally. No type of additional shear reinforcement is present in the structure. Table 2-4 list nominal Canadian standard reinforcement bar cross section properties, and Table 2-5 list measured reinforcement steel mechanical properties.

The massive top and bottom beam elements were designed with high reinforcement ratios to ensure primarily elastic behavior in these regions.

Figure 2-5 show the derived steel reinforcement work curve for 10M bars. Specimen steel reinforcement layout, and reinforcement ratios, are shown in Figure 2-6.

Table 2-4   Nominal Canadian standard reinforcement bar cross section properties.

Rebar type	10M	20M
Area (mm^2)	100	300
Diameter (mm)	11.3	19.5

Table 2-5   Measured reinforcement steel mechanical properties [10].

Rebar type	10M	20M
Yield strength (MPa)	430	465
Ultimate strength (MPa)	638	550
Strain hardening (%)	0.8	1.5
Ultimate strain (%)	15	20
Elastic modulus (GPa)	182	190
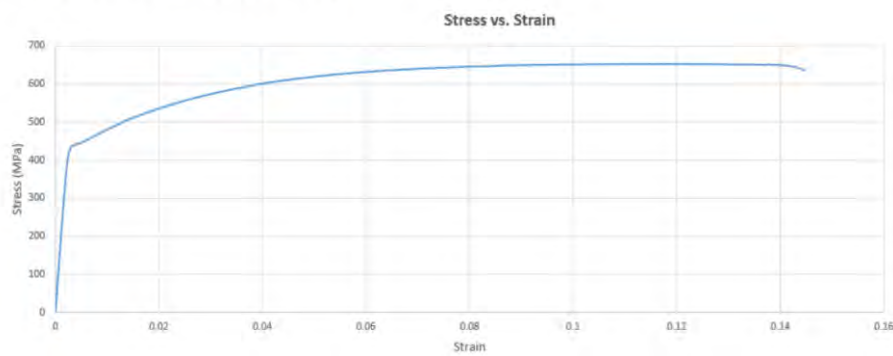
Figure 2-5   Steel reinforcement stress-strain relationship for 10M bars [17].
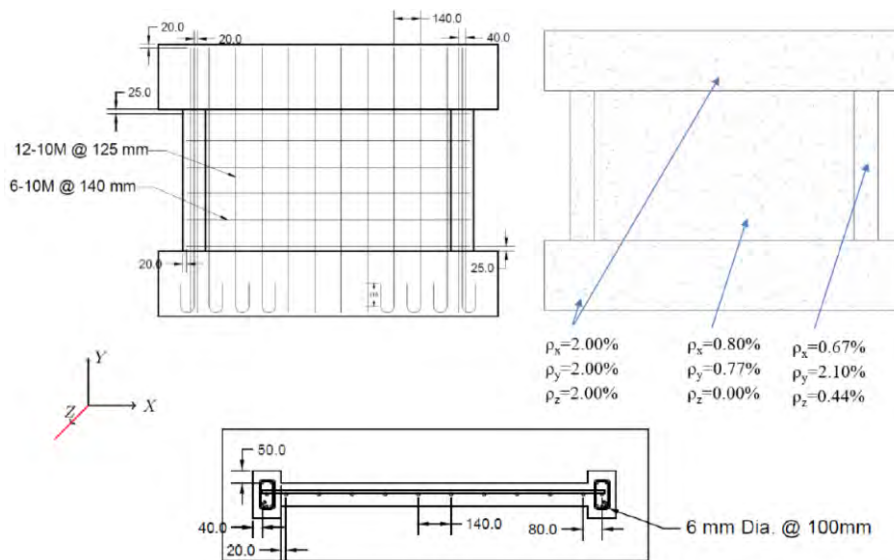
Figure 2-6   Steel reinforcement layout [10].

2.5. Experimental shear wall test setup

The experimental program was initiated to investigate the structural effects of ASR [7]. The test experimental setup information is visualized in Figure 2-7, showing horizontal and vertical hydraulic jacks used for the tests. The two horizontal actuators had a nominal capacity of 1000 kN each, as a shear capacity of 1200 kN were predicted prior to testing. A constant vertical force of 800 kN were aimed at during testing, using a hydraulic jack. The bottom beams of the test specimens were fixed by two large bolts to the "strong floor", and in addition restrained on both ends to prevent slippage.

Displacement measurements during the testing were limited to horizontal displacements at 7 positions, see Figure 2-8.

The intended lateral loading scheme, used for all the tests, is expressed in displacements, rather than force, and visualized in Figure 2-9. According to [7], the loading rate applied were initially 0.005 mm/second, and at some point increased to 0.15 mm/second. The intended loading scheme, according to [17] were; +/- 0.4, +/- 0.8, +/- 1.0, +/-1.4, +/- 1.8, +/- 2.0, +/- 2.5, etc., in steps of 0.5 mm increase until structural failure. The loading schemes described in the two references above are however not entirely identical. The failure point was defined as failure to maintain 40 % of the vertical load applied.

Additional information concerning the test setup, actual loading scheme, eventual rotations of top beam during tests, etc., are not available at present time.
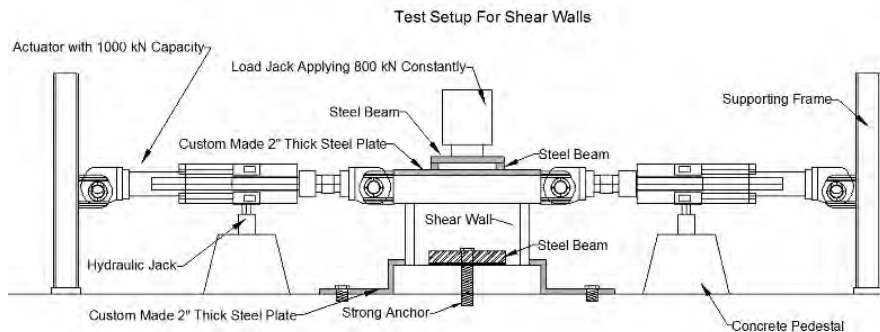
Figure 2-7   Overview visualization of the experimental shear wall test setup [17].
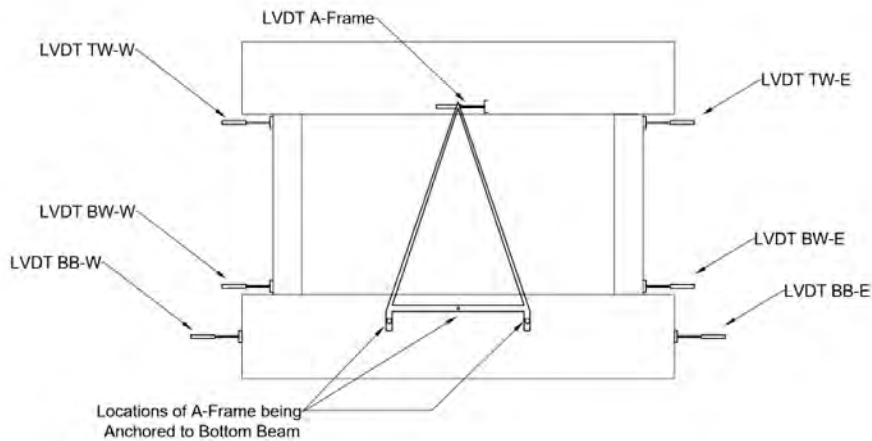
Figure 2-8   Experimental lateral displacement measurements [16].
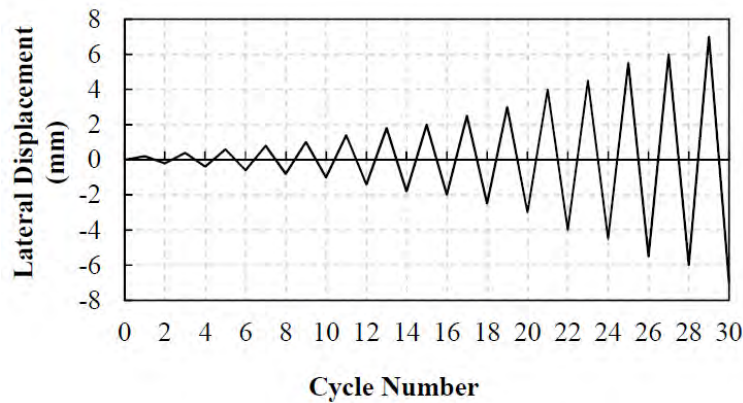
Figure 2-9   Experimental lateral loading scheme, according to [7].

2.6. Experimental results

The ASCET Phase 2 consist of blind numerical simulations of the experimental B-tests, in the form of a benchmark. The initial intentions were that benchmark participants should get access to the results from the experimental A-tests, in order to make informed decisions for the required numerical model input. However, in the end only a very limited amount of experimental results was released prior to the final workshop. The full set of results released to benchmark participants at this stage are presented in the two sub sections 2.6.1 and 2.6.2.

Crack patterns and progress during the tests were not documented, and is consequently not available for comparisons between experimental and numerical results. The second item of the ASCET Phase 2 goals, difference in failure modes as listed in section 1.2, is therefore not possible to, in detail, compare between experimental and numerical results.

From the test data presented below, and the tested mechanical material properties shown in section 2.3, it can be concluded that even though the material properties of the ASR reactive concrete seem negatively affected by

the reactions, the ASR A1 wall test specimen showed a higher structural capacity (approximately 15 %) than the control specimen with regular concrete, REG A. This observation is discussed later in this report.

In addition, the initial whole structure elastic stiffness of the ASR reactive concrete specimen, were also higher than the specimen with regular concrete. This is contradictory to the material properties specified shown in Table 2-2. The reason for this is without explanation at present time.

2.6.1. REG A specimen – Regular concrete after 240 days

The control specimen REG A (regular concrete) were tested 240 days after casting [10]. The lateral force as function of displacement during testing of wall specimen REG A is shown in Figure 2-10. Visual observations from the figure include a strong non-symmetrical behavior of the REG A specimen Figure 2-10. The reason for this behavior is however not known at present time. That this single test is truly representative of an ensemble of similar shear walls must be regarded as highly questionable, until further information is available.

A picture of wall specimen REG A at post failure, partly showing crack patterns, is shown in Figure 2-11. This information origin from [7], and is not part of the officially released ASCET Phase 2 experimental data.

Maximum Capacity (kN)	Corresponding Deflection (mm)
990.0	6.9

Maximum Capacity (kN)	Corresponding Deflection (mm)	Ultimate Displacement (mm)	Axial Load Capacity at Failure (kN)
1180.0	5.6	8.2	210
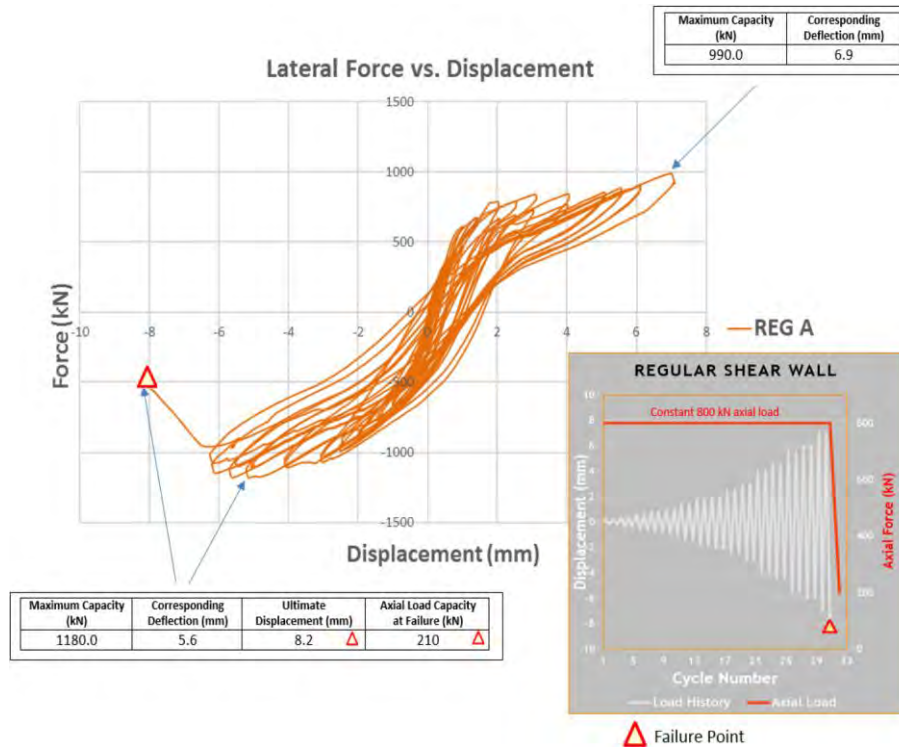
Figure 2-10 Lateral force as function of displacement during testing of wall specimen REG A (control specimen with normal concrete) [10].

14

Figure 2-11 Picture of wall specimen REG A (control specimen with normal concrete) at failure [7].

2.6.2. ASR A1 specimen – ASR reactive concrete after 260 days

The concrete specimen ASR A1 were tested 260 days after casting [10]. The lateral force as function of displacement during testing of wall specimen ASR A1 is shown in Figure 2-12.

A picture of wall specimen ASR A1 at failure, partly showing crack patterns in the wall, is shown in Figure 2-13. This information origin from [7], and is not part of the officially released ASCET Phase 2 experimental data.
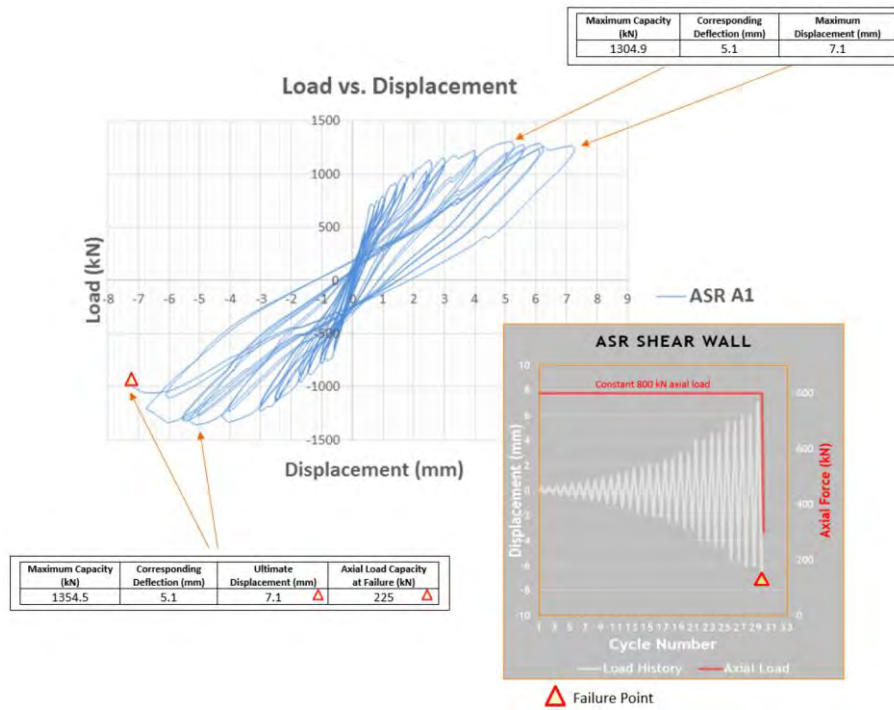
Figure 2-12 Lateral force as function of displacement during testing of wall specimen ASR A1 (specimen with ASR reactive concrete) [10].

Figure 2-13 Picture of wall specimen ASR A1 (specimen with ASR reactive concrete) at failure [7].

2.6.3. Additional information

Additional information released after the ASCET Phase 2 final benchmark workshop is here included in Table 2 6. It is noted that the final failure modes defined in [16] for regular concrete specimens are not visually confirmed in (for instance) Figure 2-11, and this require further investigation. It was also observed that the failures in the ASR specimen seemed more sudden than that of the regular concrete walls.

It was concluded in [16] that the ultimate shear capacity did not vary much between the walls.

Table 2-6 **Experimental results released after the benchmark final workshop [16]. It is noted that the final failure modes defined in [16] are not visually confirmed in (for instance) Figure 2-11, and this require further investigation.**

Test specimen	Peak force (kN)	Max. displ. (mm)	Final failure mode
REG A	1180	8.2	Sliding between wall panel and bottom beam
REG B	1187	7.3	Sliding between wall panel and bottom beam
ASR A1	1355	7.1	Diagonal
ASR B1	1240	4.9	Diagonal
ASR B2	1243	2.6	Diagonal

2.6.4. Experimental result discussion

To clarify differences in the experimental data between the different concrete configurations, in Figure 2-14 a comparison of enveloped experimental results for lateral load versus displacement relationship of both the Regular A and ASR A1 shear wall specimen are made. The experimental data in the figure is envelope force-displacement relations graphically interpreted from [7].

According to [18], it is common for ASR-affected reinforced concrete structures to have un-affected load bearing capacity, despite large expansions, extensive cracking, and decreased stiffness and strength. The effect is accredited the confinement effect of the structure as the concrete material expands, and the steel reinforcement act as a post tensioning system. However, the fact that the ASR affected wall in these particular experiments otherwise nominally identical to the wall with regular concrete, had stiffer structural behavior for the initial primarily elastic responses, despite the lower elastic material stiffness as shown in Table 2-2, raise the question of statistically determined results; Would this relation persist in case an ensemble of specimens of each type had been tested? Variations in de facto construction, as a result of workmanship and methods used, type of aggregates, material variability, and actual experimental conditions, are outside the scope of this experiment, as only one specimen of each kind

(regular concrete, ASR concrete, and three different points in time) were fabricated and tested. Such variations may however be important and are not captured in idealized numerical models created using nominal data. Testing of concrete specimens, particularly when loaded in shear, may result in a large result scatter, and statistical experimental aspects should not be neglected. In addition, the unexpected strong non-symmetrical behavior of the REG A specimen shown in Figure 2-10 may indicate experimental problems. This may possibly be the result of some form of boundary condition problem, or data acquisition, issue. No additional information concerning this is however available at present time, and further investigation of this is therefore not possible.
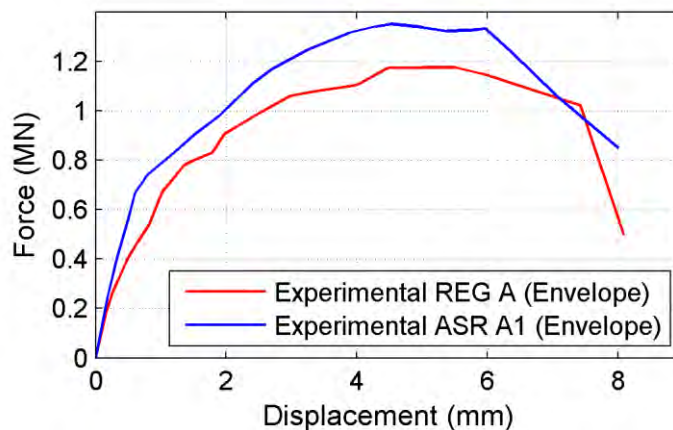
Figure 2-14 Comparison of experimental results for lateral load versus displacement relationship of Regular A and ASR A1 shear wall specimen. Envelope data from [7].

2.7. Aspects of the experimental tests compared to actual structures

The aim of the experimental campaign is, in the end, to study the structural effect of ASR with respect to actual structures in the nuclear industry. In this perspective, it should be mentioned that the studied scale models, 100 mm thick shear walls, used in the experiments include only a single layer of orthogonal web reinforcement, located at the wall center surface. No shear reinforcement, stirrups, are included in the test specimen structure due to this thin (scaled) wall thickness. For the ASR affected concrete walls in the experiments this may mean no, or very little, confining pressure in the wall thickness direction. This may differ from conventional concrete shear wall design in nuclear power plants.

It should also be noted that the laboratory experiments conducted do not include any environment or combined effects related to durability issues, as for example ASR in combination with repeated cycles of freeze-thaw. The experimental results may consequently be valid as indicators on the structural capacity due to material degradation due to ASR only, which is indeed already complex. However, this note is included to draw attention to the fact that concrete structures residing outside (PWR containments) may

experience important combined effects, and conclusions based on the experimental results, directly applied and valid to actual structures, may not be possible.

3. Numerical model

3.1. General

This chapter describe the numerical models used in the simulations of the reinforced concrete shear wall experiments presented in the previous chapter. The intentions are to present reasonable transparent modelling assumptions.

Numerical simulations within this work are performed using the Finite Element (FE) solver ABAQUS/Explicit, which is a well-known and, for many types of problems, thoroughly tested general purpose finite element program [4]. The concrete material model used in the numerical simulations is called Concrete Damaged Plasticity (CDP). A brief presentation of this constitutive model is given in section 3.4. Section 3.5 discuss general implementation of values necessary for defining the CDP material model. Both concrete (specimen central wall) and reinforcement are modelled using non-linear behavior.

Unfortunately, too little experimental results from the laboratory tests described in the previous chapter have been released to, in any way, assure that the numerical models simulate the actual experimental structures and setup in a satisfactory way. As a result, the numerical models used in this work are based on delivered nominal data only. This is an identified uncertainty which naturally, to an unknown extent, will affect the results and conclusions.

3.2. Introduction, context and previous work

Non-linear response of reinforced concrete shear walls subjected to cyclic loads is currently still an open and active research area internationally. However, despite much effort, no universally applicable constitutive model has been developed for numerical simulation of reinforced concrete. Instead, many different material models exist, and an appropriate model are to be chosen for each type of load scenario.

The type of numerical models normally developed and used for numerical assessments of laboratory experiment tests, often differ in level of details compared to the models used in assessments of actual nuclear structures. Depending on simulation purpose, and for practical reasons, models of actual nuclear structures often have less structural details included. Figure 3-1 show two such examples of numerical models of nuclear safety related concrete structures used in the post Fukushima structural stress test assessments. The aspect of numerical model refinement levels required to capture the studied shear failure mechanism, and ultimate load, is therefore also included as a separate study, presented in section 4.5.7 of this report.
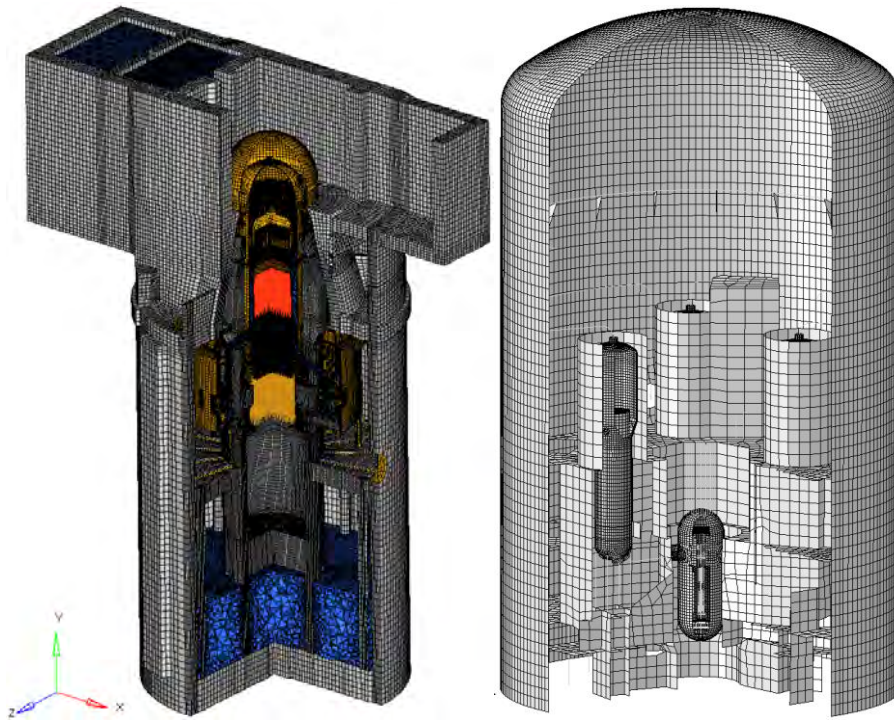
Figure 3-1   Visualization examples of numerical models of safety related concrete structures used in the post Fukushima structural stress test assessments.

3.3. Used numerical simulation software

The Finite Element software used for the numerical simulations are limited to the explicit wave front solver ABAQUS/Explicit [4]. The software is widely used, and well proven and validated, for a wide range of problems in many different industries.

The explicit solver is here favored, instead of the implicit solver, due to the large deformations, and non-linear material response. The implicit solver is concluded to give similar results for low level deformations, up to a certain limit where numerical convergence difficulties interrupt calculations.

3.4. Constitutive concrete model

Numerical simulations presented in this report has been carried out using the Concrete Damaged Plasticity (CDP) material model implementation in ABAQUS. The CDP model provides a general capability for modelling concrete (quasi-brittle) materials in all types of structure elements, e.g. beams, trusses, shells, and solids. The material model is described in detail in the software documentation [4]. The basic properties of the model are briefly discussed here, for the purpose of the simulations carried out.

The CDP material model is based on work carried out by [19] and [20], and is available in both the implicit and the explicit integration solver

(ABAQUS/Standard and ABAQUS/Explicit). The material model uses the concept of isotropic damaged elasticity in combination with isotropic tensile and compressive plasticity to represent the inelastic behavior of concrete. The model consists of the combination of non-associated multi-hardening plasticity and scalar (isotropic) damaged elasticity to describe the irreversible damage that occurs during the fracturing process. The model allows the definition of strain hardening in compression and can be defined to be sensitive to the straining rate, which resembles the behavior of concrete somewhat realistically.

3.4.1. Intended application area

According to [4]; "The model is a continuum, plasticity-based, damage model for concrete". The basic assumptions of the material model are that the main two failure mechanisms are tensile cracking and compressive crushing of the concrete material. The material model provides a general capability for modelling concrete and other quasi-brittle materials;

- uses concepts of isotropic damaged elasticity in combination with isotropic tensile and compressive plasticity to represent the inelastic behavior of concrete;
- is intended primarily for the analysis of reinforced concrete structures;
- is designed for applications in which concrete is subjected to monotonic, cyclic, and/or dynamic loading under low confining pressures;
- consists of the combination of non-associated multi-hardening plasticity and scalar (isotropic) damaged elasticity to describe the irreversible damage that occurs during the fracturing process;
- allows user control of stiffness recovery effects during cyclic load reversals.

3.4.2. Parameters to define concrete damaged plasticity

The basic parameters that need to be specified to define flow potential, yield surface, and viscosity parameters for the concrete damaged plasticity model, are listed in Table 3-1.

Table 3-1   Concrete damaged plasticity material model input parameters.

Parameter	Description	Default value
ψ	Dilation angle (in degrees)	User defined
ϵ	Flow potential eccentricity (defines the rate at which the hyperbolic flow potential approaches its asymptote)	0.1
σ_{b0}/σ_{c0}	Ratio of initial equibiaxial compressive yield stress to initial uniaxial compressive yield stress	1.16
K_c	Ratio of the second stress invariant on the tensile meridian to that on the compressive meridian at initial yield for any given value of the pressure invariant such that the maximum principal stress is negative	0.6667
μ	Viscosity parameter	0.0 in Standard N/A in Explicit

The CDP material model assumes non-associated potential plastic flow in which the Drucker-Prager hyperbolic function describes the flow potential G [4].

$$G = \sqrt{(\in \cdot \sigma_{t0} \cdot tan\psi)^2 + \bar{q}^2} - \bar{p} \cdot tan\psi \qquad \text{(Eq. 3-1)}$$

In equation 3-1, $\bar{q}$ denotes effective von Mises stress, and $\bar{p}$ the effective stress caused by hydrostatic pressure. The dilation angle ψ is measured in the p-q plane at high confining pressure and indicates the ratio between the volume change and the shear strain. The dilation angle value for concrete is commonly specified in the range of 30° to 40° [4]. The flow potential eccentricity ϵ defines the rate at which the function approaches the asymptote. With the default value of $\epsilon = 0.1$ the dilation angle is almost the same over a wide range of confining pressure stress values. The uniaxial failure tensile stress σ_{t0} is via the tension stiffening definition specified by the user [4]. The model provides the possibility to specify a non-circular yield surface in the deviatoric plane, see Figure 3-2.
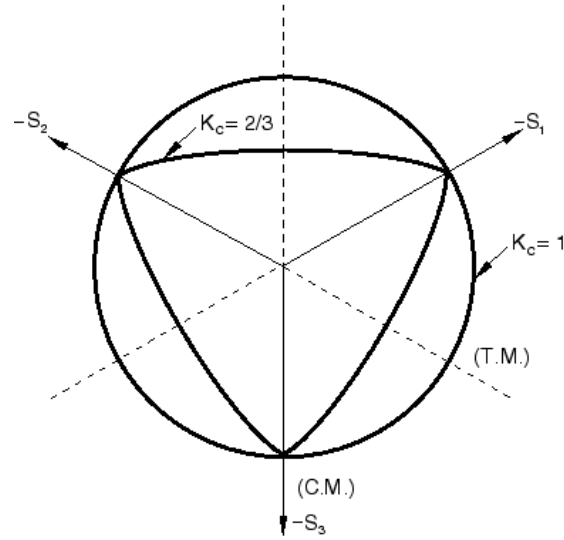
Figure 3-2   Yield surfaces in the deviatoric plane, corresponding to different values of K_c [4].
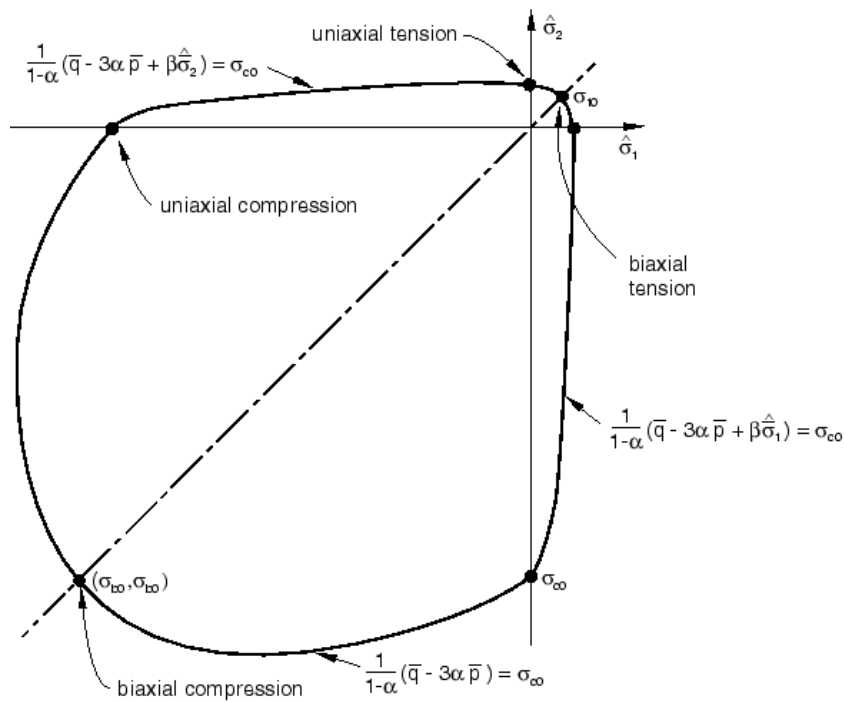
Figure 3-3   Yield surface in plane stress [4].

The third and fourth parameter stated in Table 3-1 is included in the yield function used in the CDP model, which in terms of effective stresses has the form:

$$F = \frac{1}{1-\alpha}(\bar{q} - 3\alpha\bar{p} + \beta(\tilde{\varepsilon}^{pl})\langle\hat{\bar{\sigma}}_{max}\rangle - \gamma\langle-\hat{\bar{\sigma}}_{max}\rangle) - \bar{\sigma}_c(\tilde{\varepsilon}_c^{pl}) = 0 \qquad \text{(Eq. 3-2)}$$

with

$$\alpha = \frac{(\sigma_{b0}/\sigma_{c0}) - 1}{2(\sigma_{b0}/\sigma_{c0}) - 1} \qquad \text{(Eq. 3-3)}$$

$$\beta = \frac{\bar{\sigma}_c(\tilde{\varepsilon}_c^{pl})}{\bar{\sigma}_t(\tilde{\varepsilon}_t^{pl})}(1 - \alpha) - (1 + \alpha) \qquad \text{(Eq. 3-4)}$$

$$\gamma = \frac{3(1 - K_c)}{2K_c - 1} \qquad \text{(Eq. 3-5)}$$

3.4.3. Model behavior in compression

The concrete material behavior in compression outside of the elastic regime is defined by the relation of yield stress σ_{c0} and inelastic strain, $\tilde{\varepsilon}_c^{in}$. The inelastic strain is defined as the total strain minus the elastic strain corresponding to the undamaged material, see equation 3-6 and [4].

$$\tilde{\varepsilon}_c^{in} = \varepsilon_c - \varepsilon_{0c}^{el} \qquad \text{(Eq. 3-6)}$$
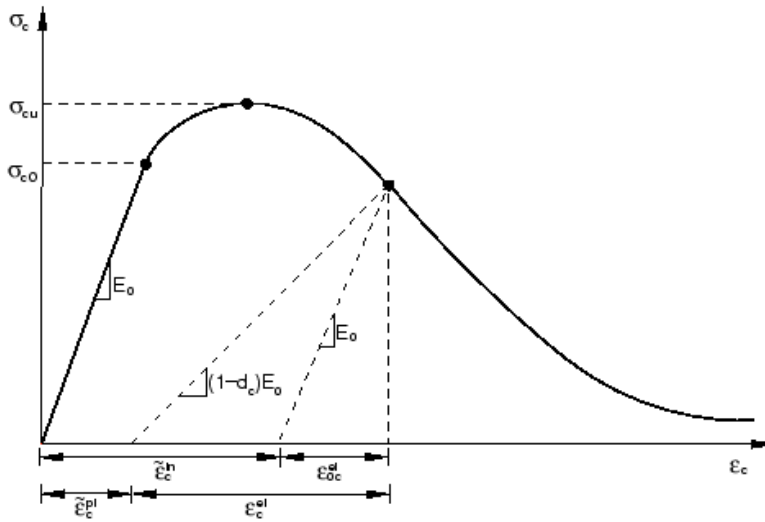
Figure 3-4   Model material response in uniaxial compressive loading [4].

The uniaxial initial yield stress value σ_{c0} is according to Eurocode 2 [21] defined as 40 % of the mean value of the cylinder ultimate compressive stress (f_{cm}), denoted σ_{cu} in the figure above. Corresponding strain is then calculated according to Hooke's law, i.e. $\varepsilon_{0c}^{el} = \frac{\sigma_{c0}}{E_0}$ and the maximum strain is taken as $\varepsilon_{max} = \varepsilon_{0c}^{el} \cdot 20$. The inelastic stress curve is defined according to [20] in the following manner:

$$\sigma_c = \sigma_{c0}\left[(1 + a) \cdot e^{-b \cdot \tilde{\varepsilon}_c^{pl}} - a \cdot e^{-2 \cdot b \cdot \tilde{\varepsilon}_c^{pl}}\right] \qquad \text{(Eq. 3-7)}$$

with

$$a = 2 \cdot \frac{f_{cm}}{\sigma_{c0}} - 1 + 2 \sqrt{\left(\frac{f_{cm}}{\sigma_{c0}}\right)^2 - \frac{f_{cm}}{\sigma_{c0}}}$$ (Eq. 3-8)

$$b = \frac{\left(\dfrac{d\sigma}{d\tilde{\varepsilon}_c^{pl}}\right)}{\sigma_{c0}(a-1)}$$ (Eq. 3-9)

The numerator in equation 3-9 describe the inclination of the curve at the initial yield stress value.

3.4.4. Model behavior in tension

In general, when using the CDP material model, the concrete behavior in uniaxial tension is defined as the relation between post failure stress and either of cracking strain, $\tilde{\varepsilon}_t^{ck}$, crack displacement, u_t^{ck}, or fracture energy, G_f. In the work carried out within current project the uniaxial tension behavior is given as the relation between post failure stress and cracking displacement as seen in Figure 3-5. This is due to the fact that models of non-reinforced structures are mesh sensitive when using the cracking strain definition. This mesh sensitivity is for most practical applications eliminated through the implementation of a characteristic element length associated with each integration point, when using cracking displacement input definition methods (*CONCRETE TENSION DAMAGE, TYPE=GFI and TYPE=DISPLACEMENT) [4].
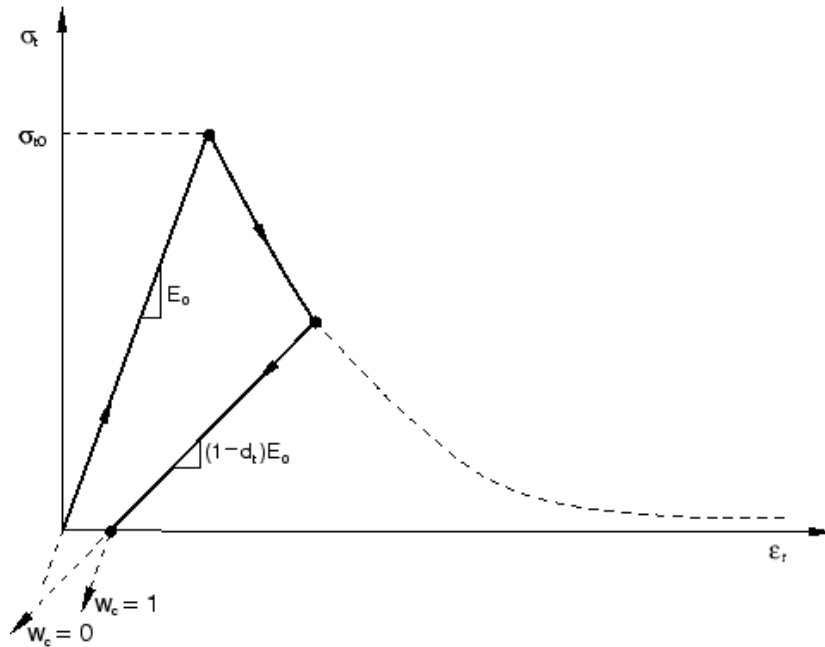
Figure 3-5   Model material response in uniaxial tension [4].

The relation between post failure stress and cracking displacement is calculated according to equation 3-10.

$$\frac{\sigma_t}{f_{ctm}} = f\big(u_t^{ck}\big) - \frac{u_t^{ck}}{u_{t0}^{ck}} \cdot f\big(u_t^{ck} = u_{t0}^{ck}\big) \qquad\qquad \text{(Eq.3-10)}$$

where

$$f(u_t^{ck}) = \left(1 + \left(\frac{C_1 \cdot u_t^{ck}}{u_{t0}^{ck}}\right)^3\right) \cdot e^{-C_2 \cdot u_t^{ck}/u_{t0}^{ck}} \qquad\qquad \text{(Eq.3-11)}$$

For a normal weight concrete the constants C1 and C2 given in equation 3-11 are 3 and 6.93 respectively. The concrete fracture energy is defined as the area underneath the graph seen in Figure 3-6. The cracking displacement at which complete loss of strength takes place u_{t0}^{ck}, may be determined by first establish a reasonable concrete fracture energy G_F and then integrate the combined expression of equation 3-10 and 3-11. For a normal weight concrete this gives following relation:

$$u_{t0}^{ck} = \frac{G_F}{0.195 \cdot f_{ctm}} \qquad\qquad \text{(Eq. 3-12)}$$

When using the CDP material model, the damage caused by strains is measured with a damage tension parameter denoted "concrete tension damage" d_t. The parameter may be visualized during post processing and indicates the status of the concrete after cracking has occurred, i.e. grade of impaired stiffness. In the work carried out within current project the concrete tension damage is linearly defined with a maximum of 0.9. This means that an element gets inactive when the cracking displacement u_{t0}^{ck} is reached and at this point the damage tension parameter has the value of 0.9.
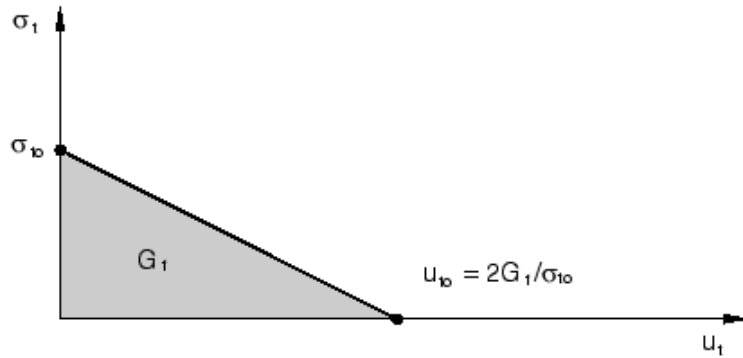
Figure3-6   Defining material model behavior in concrete tension stiffening, using definition type GFI, [4].

3.4.5. Material damage

The material point damage in tension and compression, d_t or d_c, are defined in tabular form. If damage relations are not defined, the model behaves as a plasticity model with $\tilde{\varepsilon}_t^{pl} = \tilde{\varepsilon}_t^{ck}$ and $\tilde{\varepsilon}_c^{pl} = \tilde{\varepsilon}_c^{in}$. Damage variables are each treated as non-repairable, always increasing, quantities.

3.4.6. Uniaxial cyclic loading model behavior

A user control of stiffness recovery effects during load reversals are available in the model. Stiffness recovery on crack closure is an important feature of the material model under cyclic loading conditions. This is implemented as a compressive stiffness recovery possibility as a crack is closed, as material response changes from tension to compression. The tensile stiffness is however not recovered as compression change to tension, after crushing cracking has occurred. The implementation is facilitated using the stiffness recovery factors, w_t and w_c. The behavior described above correspond to $w_t=0$ and $w_c=1$, which are the default stiffness recovery factor values. See Figure 3-7 for an illustration at uniaxial cyclic conditions.
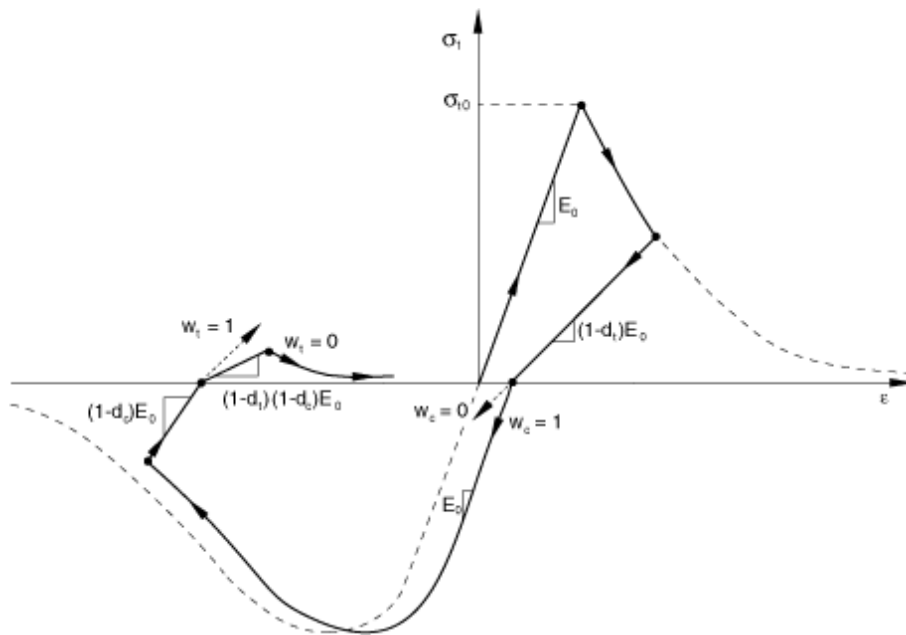
Figure 3-7   Uniaxial load cycle of the concrete damaged plasticity model when material response shifts signs [4].

3.4.7. Comparisons to actual concrete material behavior

The CDP material model has successfully been used in several application areas. It can be concluded that the material model has some features sometimes not entirely replicating, in some broad sense of the expression, "characteristic concrete behavior". For one, the model is a modified plasticity model, meaning that once inelastic in one material direction, all other material directions are also inelastic. This differ from that of a crack region in concrete and should, possibly more so for complex shear dominated response situations, result in a softer behavior than real concrete has.

The CDP material model differs from conventional von Mises plasticity by having, among other features, dis-similar definitions for tension and compression behavior. As tension behavior is much weaker than the compressional behavior, the cyclic response will in practice induce an

unphysical and artificial swelling of damaged material at load reversals. This effect is noticeable even for some monotonic loading conditions, and fairly pronounced for some cyclic loading conditions. One-element shear load tests performed has confirmed this unwanted feature.

3.5. Used material model input

Measured material strength values and properties derived within the experimental campaign are presented in sections 2.3 and 2.4. The following two sections present and discuss used input material parameters for the numerical models.

3.5.1. Concrete

Concrete material parameters for the base model used in simulations of the normal concrete test specimen, REG A (see Table 2-1), are summarized in Table 3-2. Some input parameters listed in the table are more or less to be considered as standard concrete material parameters, here either taken from the Eurocode 2 design standard [21], or experimentally measured values (presented in sections 2.3), whereas some of the input parameters are related to the specific implementation of the constitutive model. General motivations for each parameter are therefore included in the table. Since the analyses are performed with the ABAQUS/Explicit solver, the viscosity parameter μ is not in effect.

As a best estimate response is targeted in the numerical simulations carried out, the experimentally derived concrete material properties presented in section 2.3 are used as model input. Although it should be noted, for best estimate response, compression strength material model input from tests using cylinder specimens should not be used. Instead, compression strength measured from cube tests should preferably be used as input to the concrete material model in numerical simulations, because of their inherent characteristics coming to a higher degree from primarily material compression failure [22]. For compression tests of cylinder specimens, combined effects of both the material characteristics, and type of structure tested (and boundary conditions, friction), dictate the type of failure and the ultimate compression strength. Typically, the compression strength of a standard cylinder compression test is approximately 80 % of the value obtained using a standard cube test. See illustration of plausible cylinder compression test failure mode, for an idealized cylinder specimen numerically simulated, in Figure 3-8. It has not been possible, within the work presented in this report, to in detail investigate requirements on test data and relevant test methods for all the material input parameters needed. However, it is concluded that well informed decisions need to be made and justified for all material model input parameters. Using experimentally derived material parameters, it is important to be aware of what is an actual material parameter, appropriate as material model input, and what is merely considered to be a material property by force of conventional practice.
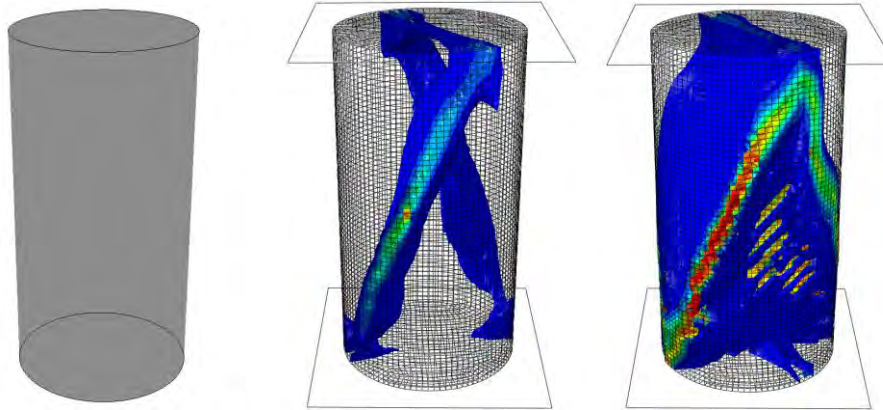
Figure 3-8   Cylinder compression test simulation, showing crack formation and failure mode, as a mean to study the type of concrete material data to be used as input for numerical simulations. Isosurfaces of compressive damage visualized in the figure at different displacements.

The concrete uniaxial behavior is specified in compression and tension according to Figure 3-9 and Figure 3-11. For tension behavior two options are pursued; the Two-parameter option, and tabular definition. Both options respect the same material parameters, ultimate tensional strength and (mode I) fracture energy. Figure 3-6 visualize the two-parameter option. This option is often used for problems where the shape of the function play a minor role, and the ultimate uniaxial tensional stress or the fracture energy is more important, as usually in pure tension or bending problems. For shear type of problems, the tabular definition may also need to be studied. Properties for closed tensional cracks include the ability to transfer compressive stress on load reversal and crack closure. However, cracks due to compression load will not transfer the full original tensional stress on load reversal, once cracking due to compression have occurred.

Table 3-2   Concrete material model input used in simulations of the intended normal (regular) concrete test specimen, REG A.

Parameter	Description	Value (@ T=20°C)
E	Initial, undamaged, modulus of elasticity (experimentally measured)	47.15 GPa
υ	Poisson's ratio (standard value)	0.2
ρ	Density (standard value without reinforcement steel)	2250 kg/m^3
ψ	Dilation angle, in degrees (chosen based on previous studies and [4])	38
ϵ	Flow potential eccentricity (default program value)	0.1
σ_{b0}/σ_{c0}	Ratio of initial equibiaxial compressive yield stress to initial uniaxial compressive yield stress (default program value)	1.16
K_c	Ratio of the second stress invariant on the tensile meridian to that on the compressive meridian at initial yield for any given value of the pressure invariant such that the maximum principal stress is negative (default program value)	0.667
σ_{cu}	Ultimate compressive stress, here set to stress at concrete crushing strain, 3.5‰ (experimentally measured)	79.0 MPa
σ_{t0}	Failure tensile stress (experimentally measured)	4.76 MPa
G_F	Fracture energy (experimentally measured)	179.3 N/m
d_c	Concrete compression damage	Figure 3-10
w_t	Recovery of tension after concrete compression damage (0 mean that after compressive failure, no matter the size, no tensional forces are transmitted through the crack)	0.0
-	Maximum value of concrete tension damage (default program value)	0.9 (linear variation from 0)
u_{t0}^{ck}	Crack displacement at maximum value of concrete tension damage	0.18 mm
w_c	Recovery of compression capability after concrete tension damage (1 mean that after failure initiation in tension, compressive forces are still transmitted through the crack)	1.0
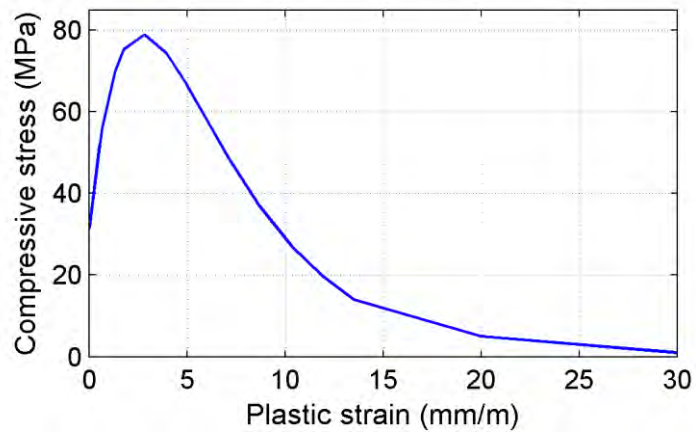
Figure 3-9   Concrete model behavior in uniaxial compression. The function is defined linear up to 40 % of the ultimate compression value, according to EC2 [21].
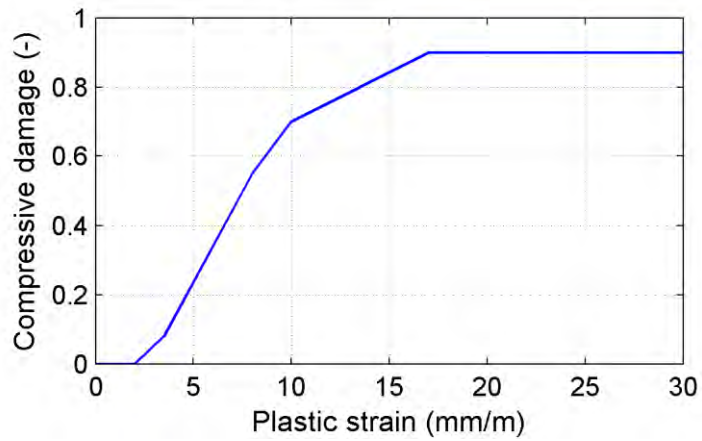
Figure 3-10 Concrete model compression damage definition (d_c).
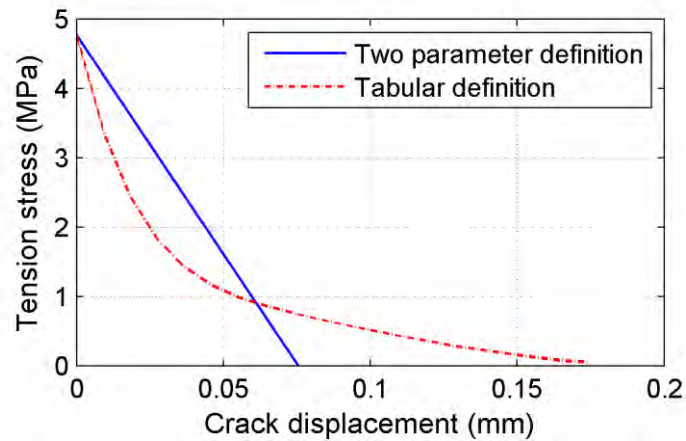
Figure 3-11   Concrete model behavior in uniaxial tension for the two different options; Two parameter (TYPE=GFI) definition, and Tabular definition. Ultimate tension stress and fracture energy are here identical for the two definition options shown in the figure.

3.5.2. Reinforcement steel

The steel constituting reinforcement is modelled using material values according to Table 3-3. For the plastic region, a simple ideal plastic material is assumed, in order to be able to obtain a rough estimate of the ultimate capacity of the shear wall.

Table 3-3   Reinforcement steel nominal material parameters used.

Parameter	Description	Value (20°C)
E	Modulus of elasticity	182 GPa
υ	Poisson's ratio	0.3
ρ	Density	7800 kg/m^3
σ_y	Yield stress	430 MPa
σ_u	Ultimate stress	638 MPa
ε_u	Ultimate elongation	14 %

3.6. Base numerical model overview

The base model used in the majority of the simulations presented in this report is visualized in Figure 3-12 below. The upper and lower beams are modeled using 8-node hexagonal reduced integration elements, C3D8R [4], with default hourglass stiffness. These elements have linear only material properties. The wall part, and stabilizing vertical end columns, are modeled using 10-node modified tetrahedron elements, type C3D10M [4]. The model of the wall is tied to the model of the lower and upper beams, to couple not only the end nodes of the C3D10M elements, but also the mid-point nodes.

The characteristic element side length is 25 mm for all elements in the base model.

The actual specimen construction sequence, and whether a division into different casting parts were made during construction, is unknown. It is therefore assumed that the specimens each were casted at one time, and no casting joints are present in the specimens. In the numerical model, no weak sections are included between the lower and upper beam and the wall section, and the concrete model is considered homogenous without considering differential casting effects.

Additional masses from equipment are assumed to weigh half a metric ton (500 kg). This mass is applied and evenly distributed at the top surface of the upper beam.
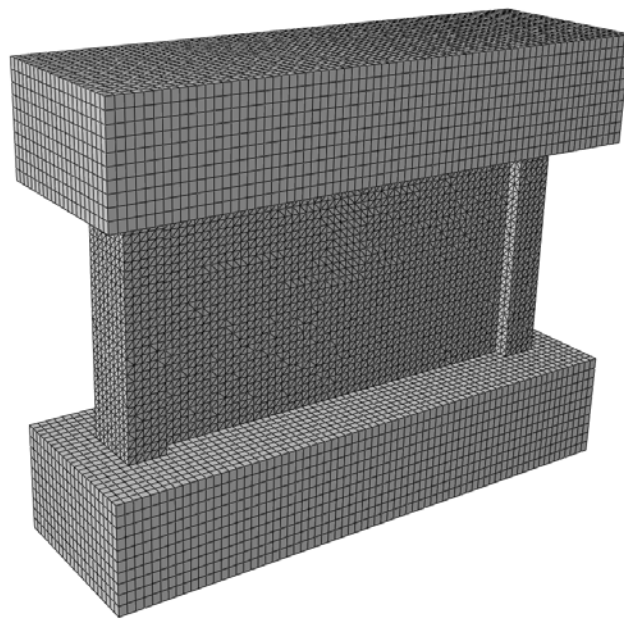
Figure 3-12 Visualization of concrete solid element model, created using the nominal measures in [10].

3.7. Model of steel reinforcement bars

The steel reinforcement described in [10] is implemented into the numerical models as discrete elements, separate from the elements representing the concrete material. The reinforcement bars are modeled using beam elements of type B31 [4], see section 4.5.8 for motivation of this choice. Element length are coordinated with the characteristic element side length of the solid elements used to model the concrete. The reinforcement is visualized in Figure 3-13.

The coupling between concrete and reinforcement elements are modeled as direct connections, using the embedded element option in ABAQUS, without any coupling interface describing non-linear effects between reinforcement and concrete in areas experiencing concrete cracking. This is an identified limitation of the used numerical model.
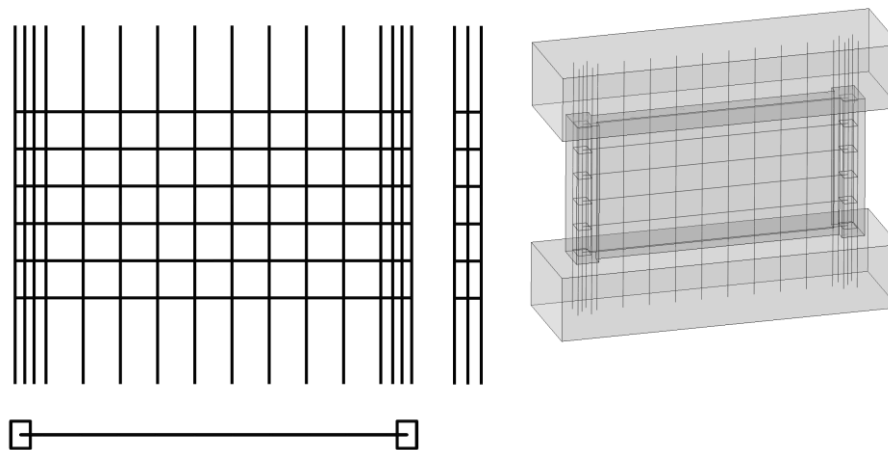
Figure 3-13 Steel reinforcement visualization, Left; reinforcement only, from 3 different orthogonal directions. Right; On place in the concrete model.

3.8. Boundary conditions

To allow for the simulation of expansion of the ASR affected concrete specimen, contact surfaces representing the floor, and hold-down system (bolt and steel plate) of the lower beam, are used. Identical models are used for the simulations of both regular and ASR affected concrete, apart from material properties and prescribed expansions discussed in section 3.11. Surface friction are kept at a zero level for the initial analysis step to allow for a stress-free expansion, see section 3.10, and ramped up to a large value in the very beginning of the second analysis step to obtain a slip-free surface contact. This possibly differ from the actual experimental setup, and is assumed to create a stiffer model than what was the case for the actual experimental test specimens. No information concerning the actual conditions during experimental tests are available at present time.

In the simulations of the ASR affected specimen the first analysis step includes the simulation of the ASR expansion, which is then free (not constrained). Contact surface definitions allow for separation after contact.

The effective boundary conditions of the numerical model of the lower beam are then constrained in all directions, including rotations. The model, including visualization of contact surfaces, is illustrated in Figure 3-14. The top beam is left without constrains. In the vertical direction both gravity loads and the prescribed additional vertical load from hydraulic jacks will be applied. The horizontal directions of the top beam are left free to allow for horizontal jack imposed displacements. The wall in-plane rotation of the top beam is left without constrains. This to allow for free rotations, which appears to likely have been the case in the physical experiments. A small study of this is included in section 4.5.1.

It should be noted that the applied restraints of the lower beam are considered overly rigid compared to actual experimentally conditions, but

still used, as no experimental data, nor other information from the specimen interactions to its surroundings during the tests are available.
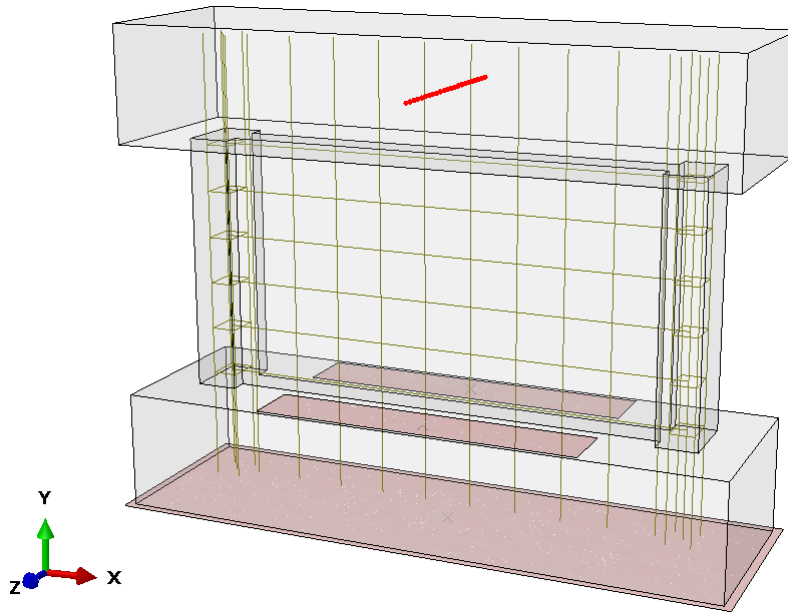
Figure 3-14 **Visualization of model. Contact surfaces used for the bottom beam are marked light red. Nodes used for application of prescribed horizontal displacement are highlighted in dark red color.**

3.8.1. Prescribed in-plane movements

The horizontal movements of the top beam, by the two horizontal jacks, having each a nominal capacity of 1000 kN [7], are modeled using displacement controlled boundary conditions of the top beam geometric center position in the x-y plane. See Figure 3-14 for model orientation with coordinate system, and the row of nodes used for application of prescribed horizontal displacement (highlighted in dark red color).

3.9. External loads applied

External loads applied are limited to the vertical actuator load, and gravity loads. These external loads are applied at an initial analysis step.

In the vertical direction, experimental force data from actuators has not been applied, as it was not available. Instead, a constant total vertical force of 800 kN [10], in the model negative Y-direction according to Figure 3-14, has been applied at the top beam, as a distributed surface load over the entire top beam surface.

In addition, gravity loading in this direction has also been applied on all elements, including an assumed additional equivalent equipment mass of 500 kg to account for steel equipment at the top beam. The actual mass of equipment on top of the top beam is not known.

3.10. Simulation types and procedures

The actual physical experiments did not include dynamic effects (inertia), but were very slow processes. See section 2.5 for load rates applied. The numerical simulations of the actual experimental events are consequently simulated using the explicit wave front ABAQUS/Explicit solver [4], as quasi-static events, including only a minimal amount of kinetic energy.

The simulations were divided into two subsequent simulation steps. An initial step, which include application of gravity load and the vertical force, and a subsequent step of the actual event of interest (monotonic push-over or cyclic event). For the ASR simulations, the expansion was also included in the first simulation step.

As complements to simulating the actual experimental events, in order to save time and evaluation efforts, monotonic static nonlinear pushover simulations have been used for the bulk of the simulations. Typical wall clock simulation times for such a monotonic pushover event is approximately 10 hours, when parallelized on 20 cores on a Linux server. The total number of variables in the numerical model is almost 500 000.

3.11. Modelling of ASR effects

Chemical processes in concrete due to alkali-aggregate reactions lead to a change of the material properties (at a macro level), which in turn cause progressive material expansion (swelling) and cracking [9]. The process is slow, and may take many years to cause substantial material and structural changes, if ever. Typically affected structures exposed to outdoor climate may experience durability issues, and combined effects from, for instance, concrete freeze-thaw [23] or reinforcement corrosion may occur. Only very few studies on the impact of ASR on safety related functions for safety significant nuclear structures are available [8]. The effects of ASR on a structural level are complex, as the changed (nominally decreased) material properties in some configurations may, on a structural level, be counterbalanced by positive confinement effects from material swelling. This may lead to non-intuitive structural shear capacity changes due to ASR, both increase and decrease, according to [8]. Most studies of ASR-affected reinforced concrete structures have indicated that the load-bearing capacity of the structures are not compromised [18].

In Sweden, no instances of ASR have been reported to the nuclear regulatory body, for NPP reactors still in production (see section 1.5). In addition, the structural effects of the ASR chemical process seem complex, and yet not fully understood. There are currently no engineering guidelines in design codes for capacity changes of structures affected, and different structural configurations may result in large, non-intuitive, variations in structural effects [8]. As a consequence, also taking into consideration the open questions regarding experimental results discussed in section 2.6.4, this phenomenon is treated using a simplistic macro-scale method in this current study.

Using numerical tools to simulate, understand and predict the structural effects of ASR may be an important part in structural verifications of

affected structures. The macro-scale modelling technique used in this study prioritize simplicity before accuracy, and results are used as conceptual indicators on the structural phenomenon of concrete material swelling. The material expansion, as well as material property degradations, are considered in this simplified approach. The method is justified based on both the uncertainty in the degradations, in terms of spatial distribution and reaction progress, for an actual nuclear structure. In the assessment of actual structures, both engineering judgement, and simplified conservative modelling approaches, are believed to be important parts, although they may not be entirely correct in a scientific perspective. For further information on some selected refined methods of modelling ASR effects, see for instance references [7] and [8].

3.11.1. Material expansion

Material expansion in the concrete is modelled using an equivalent isotropic thermal expansion. The expansion is modelled uniform in the entire test specimen, as a simplification and in absence of other information, which likely is not the case for any real structure. Conceptual explanations of material expansion due to ASR are described further in [7].

Experimentally measured free swelling of small concrete samples related to the shear wall studied here are presented in [10], and accounted for in Table 2-3. Based on this the free expansion at the ASR A1 test 250 days after casting is assumed to be 0.185 %, and a graphically roughly estimated value of 0.30 % (from Figure 2-4) is used for the ASR B2 test simulations. See Table 2-1 for information concerning the different experimental tests to be numerically simulated.

Although not explicitly stated in any of the ASCET reference documents, the entire test specimen, including upper and lower beam elements, are assumed to be of the same reactive concrete type in the numerical models.

3.11.2. Material property changes

According to [6] and [7], the tensile strength and stiffness of the concrete is more affected by AAR than the compressive material strength, which is consistent with the conclusions in the literature study [9], and in [18].

Material property changes due to ASR include stiffness and strength parameter reductions, which in the numerical simulations of the ASR A1 test specimen are selected according to the given values, specified in Table 2-2. For the numerical simulations of the ASR B2 test specimen (tested after approximately 1000 days at exhausted chemical reactions), material property changes are intended to be estimated by benchmark participants. However, as regular code equations for estimation of material parameters do not apply to ASR affected material, the same values as used for the numerical simulations of the ASR A1 tests are used. This mean that expansion effects only will be evaluated.

3.11.3. Concrete and steel reinforcement interface

The effect of ASR on the concrete and reinforcement steel interface (bond) is not considered in this work, although this is likely an important issue for the ductile behavior, and shear capacity, in some situations.

4. Results and comparisons

In this chapter, some selected results from the numerical work performed within the benchmark participation are presented. For test specimens REG A and ASR A1, numerical simulation output is compared to experimental results available, and result comparisons are discussed based on the official ASCET program goals. The official ASCET program goals of the numerical simulation benchmark is to study;

1) The ability to predict the behavior of concrete elements with ASR,
2) the difference in failure modes between ASR and sound specimen,
3) the difference in ultimate capacity,
4) the difference in ultimate displacements.

The first item in the list above is here interpreted as being able to characterize the noticeable differences observed in the experimental results between the REG A test specimen and the ASR A1 specimen. These differences include differences in ultimate capacity, and possibly different crack patterns and failure modes. It should in this context be noted that the experimental tests consist of two different individual tests, not being statistically ensured, which indicate that some caution should be used when interpreting results. The ultimate capacity is simply interpreted as the maximum whole wall shear force during the event, which make this parameter simple to evaluate. The ultimate displacement (ductility measure) is however not simple to define, and no guidance, nor criteria, for evaluating this parameter is given. In the evaluations of this parameter a subjective approach, based on visual determination of when the ultimate diagonal crack is formed, is therefore used in this chapter.

Ultimate capacity and displacement for A and B series of specimen are summarized in Table 4-1. Experimental values for the B-series of tests used in the table are from the University of Toronto presentation at the concluding ASCET Phase 2 workshop [16], which were presented after the numerical work in this report were finalized. In general, experimental and numerical ultimate capacity agree reasonably well for the regular concrete walls. Concerning the specimen having an advanced state of ASR (ASR B2), whole wall ductility has been dramatically reduced, and simplified numerical method adjustments does naturally not capture this reduction.

Table 4-1 **Ultimate capacity and displacement summary table. Numerical simulation capacity presented are calculated using best estimate material parameter input and monotonic load application.**

Specimen	Method used for deriving structural shear capacity	Ultimate capacity (kN)	Ultimate displacement (mm)
Regular A	Experimental (Section 2.6)	1180	8.2
	Numerical (Section 4.1)	1040	Approx. 8-10[2]
Regular B	Experimental (Section 2.6)	1187	7.3
	Numerical (Section 4.2)	1090	Approx. 8-10[2]
ASR A1	Experimental (Section 2.6)	1355	7.1
	Numerical (Section 4.3)	1080	Approx. 8-10[2]
ASR B2	Experimental (Section 2.6)	1243	2.6
	Numerical (Section 4.4)	1120	Approx. 8-10[2]

[1] Ductility based on crack formation of ultimate failure mode.

The general philosophy for the numerical simulations carried out is based on combining best estimate input, with a simplified engineering approach to the physics behind the ASR effects on the concrete specimen, as the actual physics of the reactive processes are considered too complex to incorporate in detail. The engineering approach used for describing the ASR effects consist of isotropic material expansion and reducing concrete material properties. This is described in more detail in section 3.11.

In this chapter, numerical results and predictions for the different test specimens (REG A, ASR A1, REG B and ASR B2) are also presented. The tests REG B and ASR B2 are completely blind predictions, as experimental data for these tests were not available. As such, little effort has been put into the work with these, as both input and output from the experimental campaign are unknown. In addition to results for the best estimate numerical models, several sensitivity analyses have been carried out for a selected set of model input parameters. These are considered to contribute with valuable information, and are presented later in this chapter. In the last part of this chapter a brief comparison to design code capacity are made for both numerical and experimental results.

Due to the used material model inability to successfully simulate the inelastic responses during the complete cyclic shear load event, discussed in section 4.1.2, quasi-static monotonic loading is used for the majority of the numerical studies presented in this report.

Result figures visualizing the predicted crack patterns in the numerical models in this chapter are mainly contour plots of resulting material damage in tension, output variable DAMAGET [4]. Displacements are magnified a factor of 20 in result figures throughout this chapter, unless stated otherwise. The comparative experimental force-displacement curves shown in the

horizontal capacity figures (named Experimental REG A, and Experimental ASR A1), is the enveloped experimental data shown in Figure 2-14.

4.1. Comparisons for regular concrete specimen REG A

In this section results from the numerical simulation of the regular concrete specimen, REG A, are presented. The experimental tests were carried out at specimen age 240 days, see section 2.2.

4.1.1. Monotonic push over simulation results

Figure 4-1 show a comparison of horizontal whole wall push over capacity functions for the REG A numerical simulation, compared to experimental data. In comparison to the experimental data, the numerical model is observed slightly too stiff in the initial elastic response. This may be due to either the seemingly large value of the concrete elastic stiffness, poor interaction or coupling modelling of adjacent structures, some result of issues related to the experimental data acquisition, or a combination of these. Boundary conditions for the model are set to entirely restrained translations and rotations at the bottom beam (see section 3.8), which normally should result in a too stiff behavior compared to an actual structure. The reason for this is that this type of absolute restraint never exists in the physical world, and likely were not the case for the experimental situation at the tests compared to. However, no information is available concerning the details for the actual concrete specimen anchoring, and this modeling approach is therefore used, although it is believed to result in an overly stiff global behavior.

As discussed in section 2.6, the experimental non-symmetrical force-displacement response of test specimen REG A does not have the expected characteristics of a structure having the given nominal data, as the idealized numerical model does. In addition, the test specimen ASR A1 has an initially stiffer response than the regular concrete specimen, despite lower elastic stiffness. This is not expected, and an explanation for this is still missing at present time.
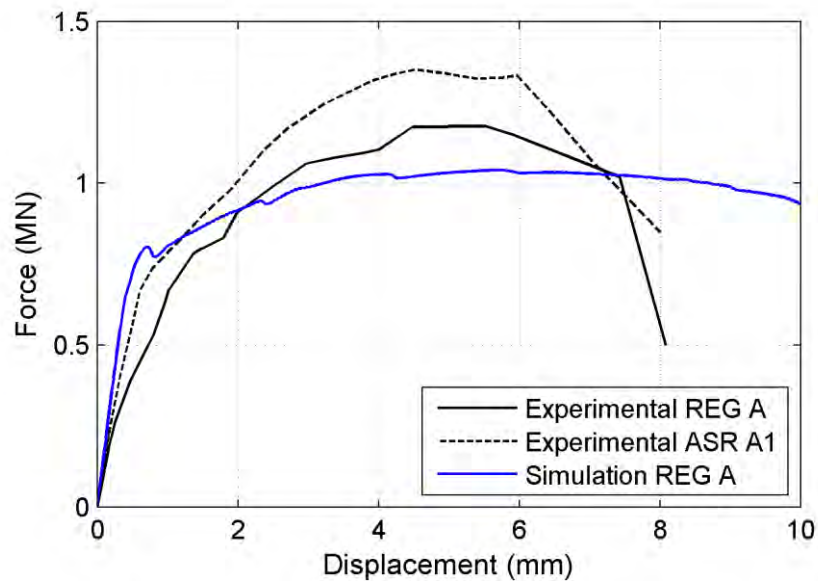
Figure 4-1   Comparison of whole wall horizontal push over capacity functions for the REG A specimen experimental test and numerical simulations.

Visualizations of crack patterns and development for the REG A numerical model are shown in Figure 4-2 and Figure 4-3. For the input used, numerical simulation output responses are initially purely elastic, up to a point where horizontal tension cracks are initiated at the interface between the wall and the lower beam at the tension side (lower left side in Figure 4-2). In-plane rotations at the upper beam is here not restrained, see section 4.5.1. As prescribed horizontal displacements increase, a shear crack form in the wall. Further displacement increase result in the development and progress of multiple cracks, parallel to the initial shear crack. The ultimate failure mode seems to be a combined shear mode, where the compression struts finally sequentially join (forming a diagonal crack) and collapse. The approximate maximum shear capacity for this loading situation is here predicted to be at a prescribed horizontal displacement of 5.4 mm, and the shear force is then 1.04 MN. The ultimate failure is estimated to begin at approximately 8.2 mm prescribed horizontal displacement, as the ultimate capacity of the right-hand side barbell side wall is reached. After that the remaining capacity is quickly reached, as one diagonal crack joins the multiple cracks previously formed in the wall. See Figure 4-4.

Minimum principal stress (compression field)   Maximum principal strain (cracked volumes)
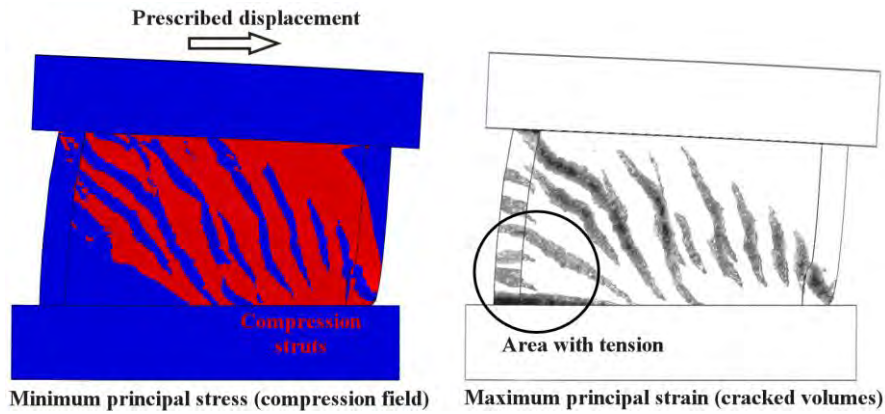
Figure 4-2   Principal response at the point of maximum shear force capacity (at 5.4 mm horizontal displacement), for the REG A specimen numerical simulations.
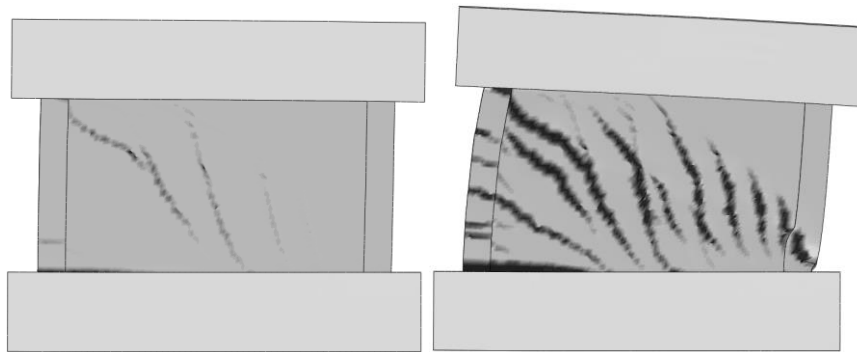
Figure 4-3   Monotonic horizontal push over response after crack initiation (at 1 mm) and at the point of maximum shear force capacity (at 5.4 mm horizontal displacement), for the REG A specimen numerical simulations.
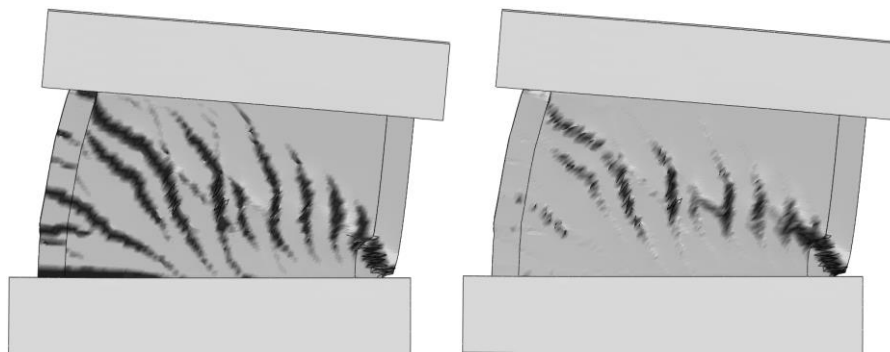
Figure 4-4   Visualization of (close to) ultimate crack pattern and failure mode for the REG A specimen, to be compared to experimental results shown in Figure 2-11. Left figure show tension damage, and right figure show compression damage, at 8.2 mm horizontal displacement.

Reinforcement stresses are shown at initial yield in Figure 4-5, and at 10 mm prescribed horizontal displacement in Figure 4-6. The yield stress is defined

45

to 430 MPa, as described in section 3.5.2. Figure 4-7 show the predicted reinforcement equivalent plastic strain at 10 mm horizontal displacement. No experimental data is available for comparisons at present time.
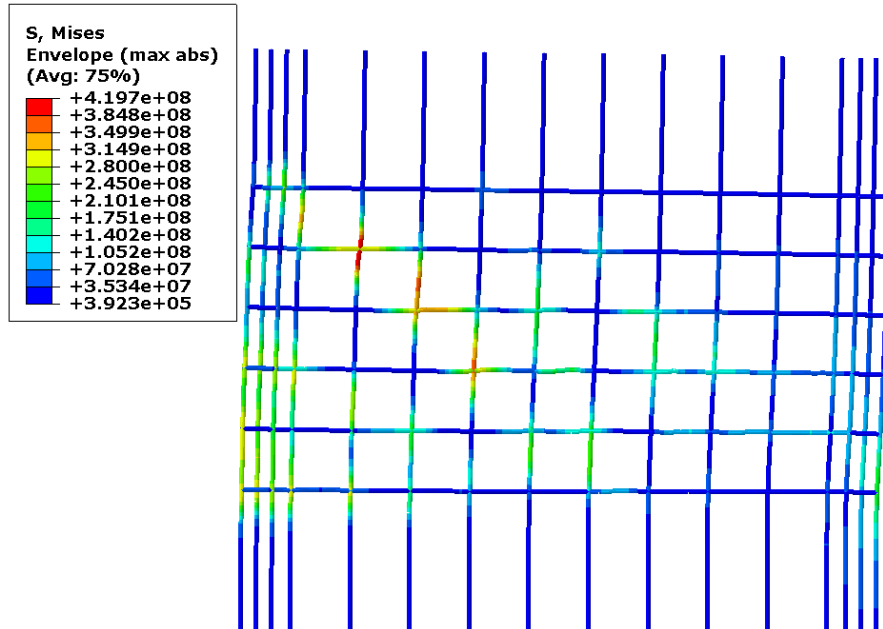
Figure 4-5   Predicted equivalent reinforcement stress, at initial yield, at 2 mm horizontal displacement, for the REG A specimen numerical simulations.
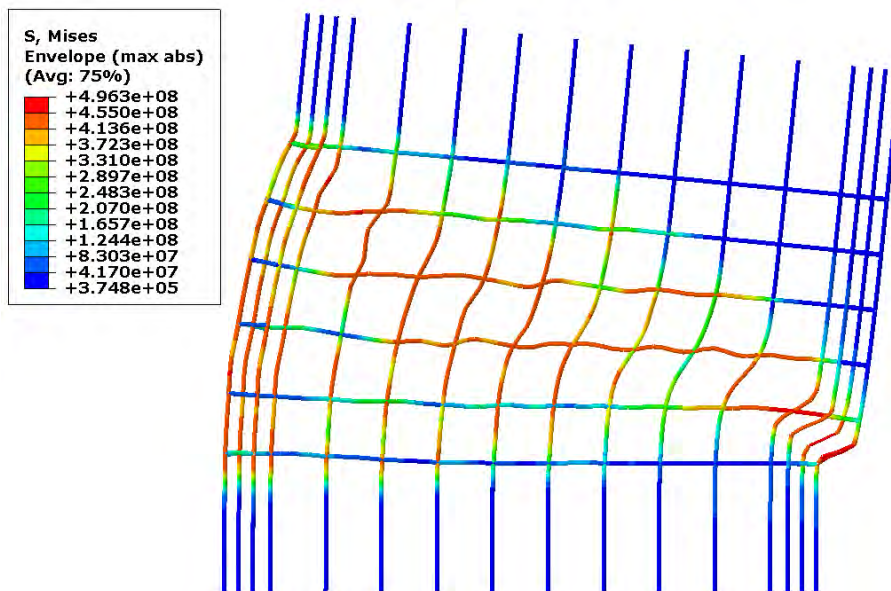
Figure 4-6   Predicted equivalent reinforcement stress at 10 mm horizontal displacement, for the REG A specimen numerical simulations.
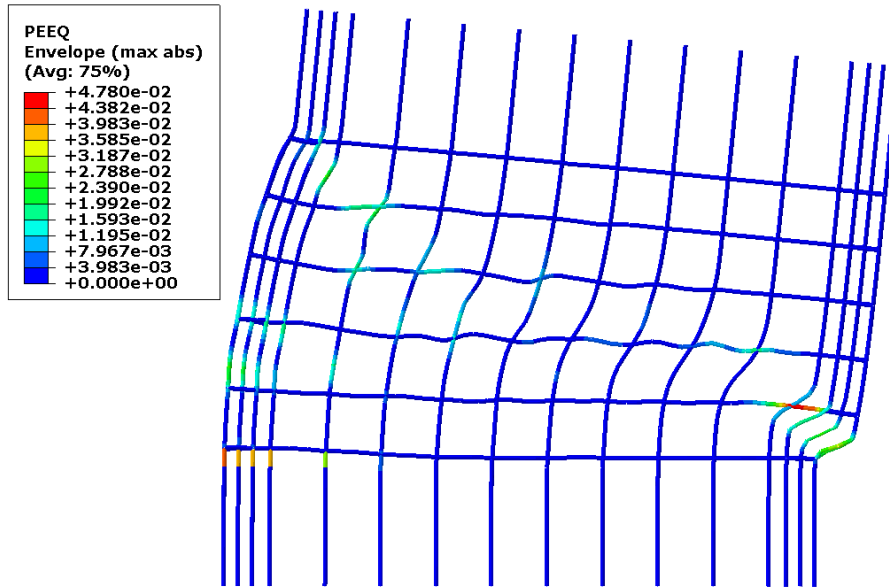
Figure 4-7 **Predicted reinforcement equivalent plastic strain at 10 mm horizontal displacement, for the REG A specimen numerical simulations.**

4.1.2. Cyclic loading simulation results

Attempts to simulate the actual cyclic load event described in section 2.5 are described in this section for the REG A specimen. The numerical model used is identical to the model used for the simulation of monotonic loading, described in the previous section. The prescribed cyclic horizontal displacement sequence used for numerical simulations is shown in Figure 4-8.

In conclusion, cyclic loading event simulations including advanced inelastic material responses, are less successfully simulated using the CDP material model in ABAQUS, for the studied shear loaded wall. The plastic damage material model exhibit an unphysical swelling effect when for exposed to repeated reversed inelastic stress states. This effect has been confirmed for 1-element numerical test cases, and the material model is believed to insufficiently represent a quasi-brittle material for the studied cyclic shear loading conditions.

Cyclic time history and push over loading (whole wall force-displacement) response for the REG A specimen numerical simulations are shown together with available experimental results in Figure 4-9. The figure show an initially fair comparison for the cyclic time history simulation, up to almost 2 mm prescribed horizontal displacement of the top beam, and then a premature and rapid loss of strength.

47
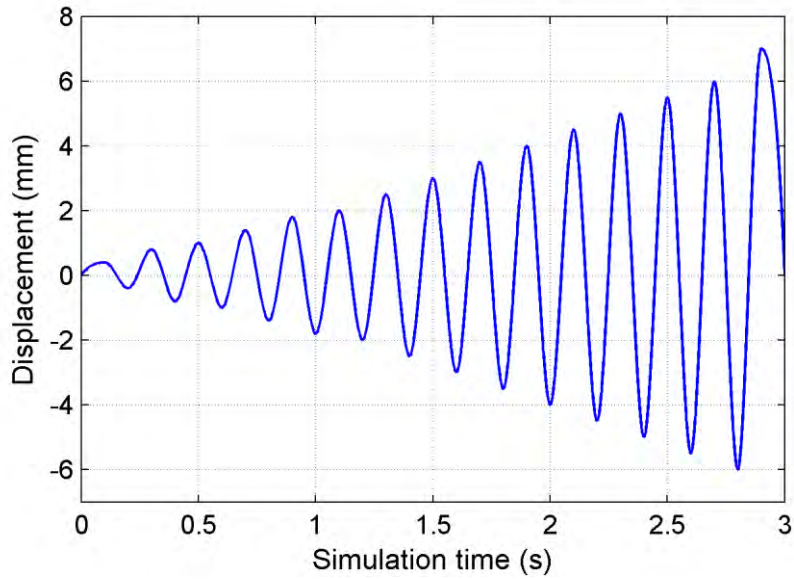
Figure 4-8   Used prescribed cyclic horizontal displacement sequence for numerical simulations.
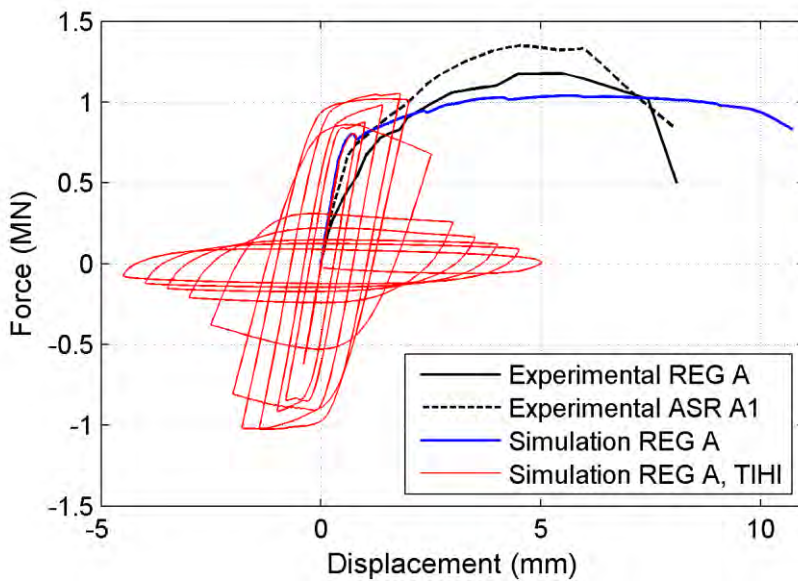
Figure 4-9   Comparison of whole wall horizontal push over capacity functions for the REG A specimen experimental test and cyclic loading numerical simulation.

In terms of crack development and pattern, Figure 4-10 and Figure 4-11 show the predictions during the first couple of load cycles. Initial crack initiation occurs as a horizontal crack plane at the lower tension side of the wall-bottom beam interface. Some of the early crack development may be termed micro-cracking, which may not be experimentally (visually) easy to detect. As crack development progress, the spurious material model swelling response induce artificial internal stress, which affect the response.

The ultimate failure mode predicted for the REG A numerical model (see Figure 4-12) is a failure mode in the shape of an inverted flat U-shape across the wall, as the last vertical load carrying capacity of the outer barbell wall sides is exhausted. Despite the apparent inability to simulate the complete cyclic event, the predicted ultimate failure mode shown in Figure 4-12 visually compare to a certain degree to the experimental results shown in picture Figure 2-11. Both tension and compression damage are shown in Figure 4-12, as the predicted ultimate failure mode is a mixed mode failure. Full access to the experimental data is however not available, which result in an incomplete comparison. Due to the observed inability of the material model to simulate the response in full, crack patterns and ultimate failure mode predictions shown here for the cyclic loading event may be of limited value, depending on the degree to which the real-world physics are violated. This is however unknown at present time.
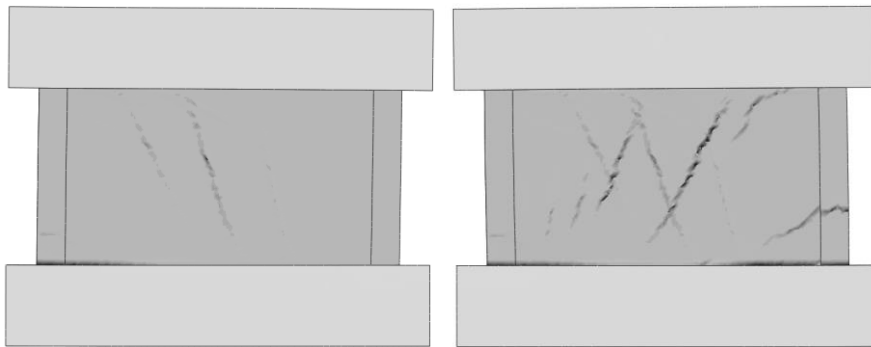
Figure 4-10 Cyclic loading response at 0.8 mm (second cycle) and -0.8 mm (second cycle reverse direction) horizontal displacement, for the REG A specimen numerical simulations.
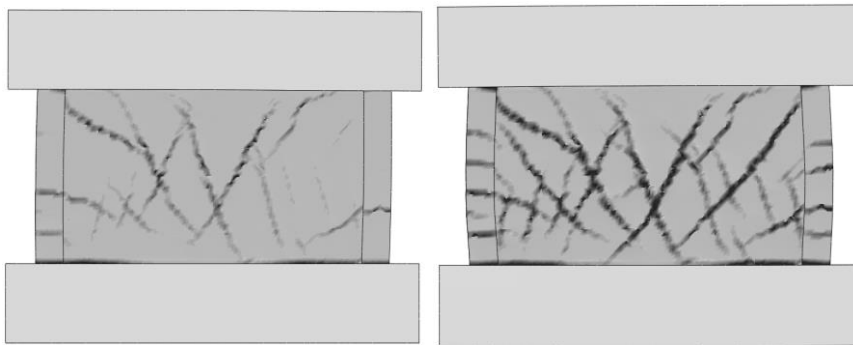
Figure 4-11 Cyclic loading response at 1 mm (third cycle) and 1.4 mm (fourth cycle) horizontal displacement, for the REG A specimen numerical simulations.
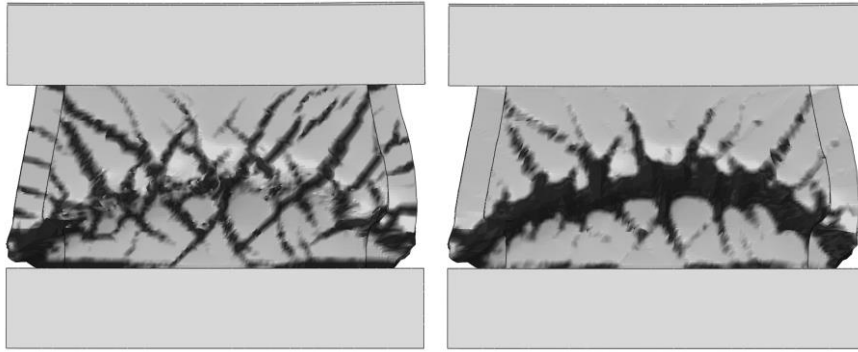
Figure 4-12 **Visualization of ultimate crack pattern and failure mode for the REG A specimen numerical simulations, to be compared to experimental results shown in Figure 2-11. Left figure show tension damage, and right figure show compression damage, at 2.5 mm total displacement (load cycle number 7).**

4.1.3. Numerical simulation energy levels

Whole model energy quantities are good simulation health indicators for the explicit numerical method used, and it's considered good practice to analyze these for each numerical simulation.

Checks for kinematic versus strain energy relations, i.e. high levels of kinetic energy indicating non static conditions, has been performed. As simulations are intended to be essentially static, the kinetic energy and viscous damping energy levels are verified to be negligible in the simulations.

The artificial (hourglass) strain energy has been notably high in some of the simulations carried out, indicating that this numerical feature has been highly activated. This is an undesirable effect, and artificial energy levels should ideally be low.

4.2. Blind predictions for regular concrete specimen REG B

In this section results from the numerical simulation of the regular concrete specimen, REG B, are presented. The test specimen was tested at an approximate age of 1000 days, see section 2.2. To account for the evolution of material properties (ultimate compression, ultimate tension, and elastic stiffness) for wall specimen REG B, some guidance from Eurocode 2 [21] may be used. However, due to the unknown concrete quality class, adjustments are here limited to increased ultimate compressive strength, corresponding to the use of the ultimate cube compressive strength. The ultimate cube compressive strength is here simply taken as the experimentally determined ultimate cylinder compression divided by the factor 0.8.

Due to the similarities between the numerical simulations of specimen REG A and REG B, the results are at large similar. The REG B specimen, having slightly higher concrete compression specified,

Figure 4-13 show a comparison of whole wall horizontal push over capacity functions for the REG B specimen experimental test and numerical simulations. Figure 4-14 show the monotonic horizontal push over response in terms of crack patterns, at crack initiation (around 1 mm) and maximum shear force capacity (at 7.4 mm horizontal displacement), for the REG B specimen numerical simulations. As differences from the REG A numerical simulation include an increased concrete compression only, differences between results from these simulations are expected to be fairly small for the loading situation studied, as only a moderate increase in capacity is predicted. The approximate maximum shear capacity for this loading situation is predicted to be 1.09 MN at 7.4 mm horizontal displacement.
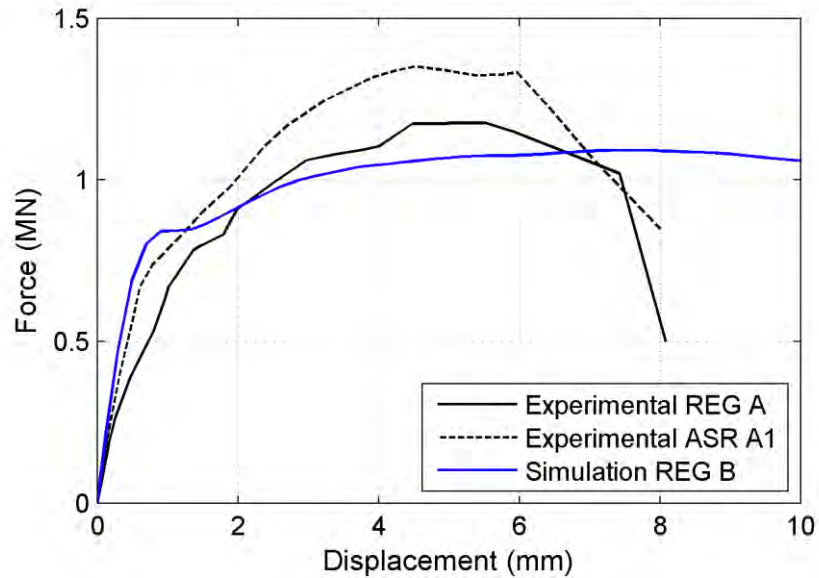
Figure 4-13   Comparison of whole wall horizontal push over capacity functions for the REG B specimen experimental test and numerical simulations.
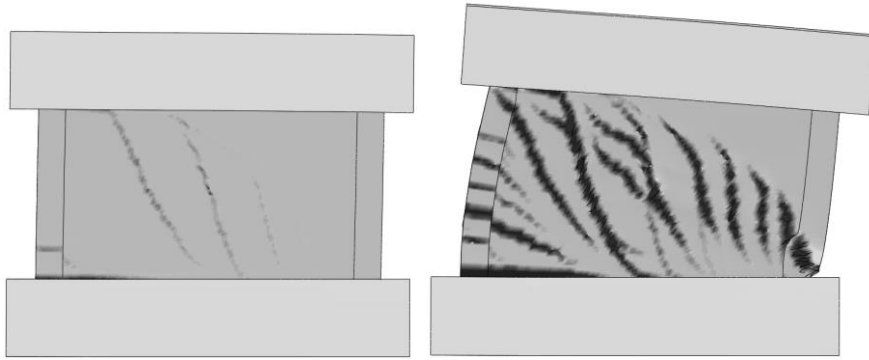
Figure 4-14 Monotonic horizontal push over response at 1 mm and 7.4 mm horizontal displacement, for the REG B specimen numerical simulations.

4.3. Comparisons for specimen ASR A1

In this section results from the numerical simulation of the affected specimen, ASR A1, are presented. Simulation input changes relative to the REG A specimen simulations include changed material parameters, and isotropic expansion, only. All other simulation input is identical between the simulations. See section 3.11 for more information about the assumed input changes for numerical simulations of ASR affected test specimen. Numerical modelling aspects of the ASR affected specimen are discussed in general terms in section 3.11. The free expansion at the ASR A1 test, 250 days after casting, is assumed to be 0.185 % in the numerical simulations, based on the experimentally measured expansion for small concrete samples presented in Table 2-2.

4.3.1. Monotonic push over simulation results

This section present results for the monotonic horizontal push over response simulation for the ASR A1 specimen. Figure 4-15 show a comparison of whole wall horizontal push over capacity functions for the ASR A1 and REG A specimen experimental tests, and numerical simulations. The numerical simulation results confirm the experimental observation that the ASR affected specimen, although having nominally weaker material properties (ultimate tension, compression and elastic stiffness), may possess a higher ultimate capacity than a structure made from regular concrete. This is confirmed to be due to the confining effects resulting from concrete material expansion, which is internally balanced by the post tensioning of the embedded reinforcement steel bars, see section 4.5.9. The whole wall initial elastic response is less stiff than the REG A structure, which is expected. This is however contradictory to the experimental results, which are currently not explained. The maximum shear capacity for this loading situation is predicted to be 1.08 MN at 4.2 mm horizontal displacement. A sensitivity study of the ASR induced confinement effect can be found in section 4.5.9.
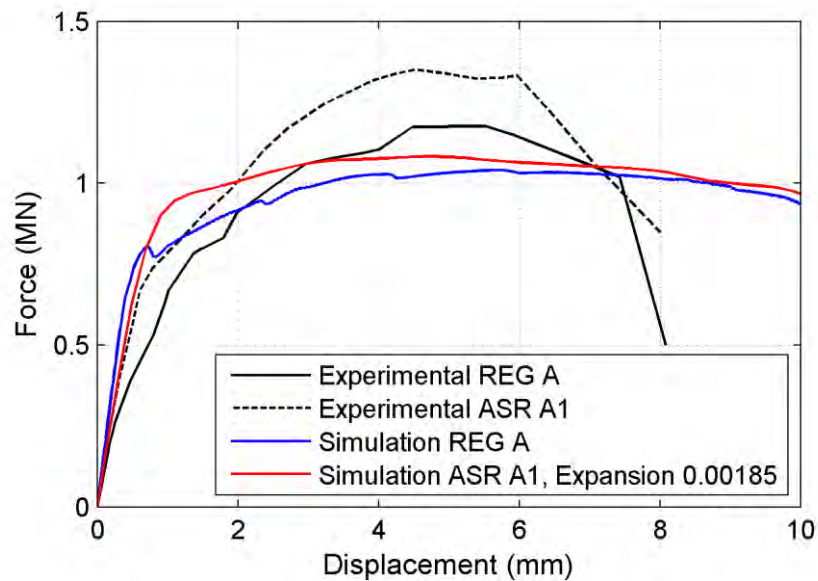
Figure 4-15 Comparison of whole wall horizontal push over capacity functions for the ASR A1 and REG A specimen experimental tests and numerical simulations.

Visualizations of crack patterns and development are shown in Figure 4-16. Horizontal tension cracks are initiated at the interface between the wall and the lower beam at the tension side (lower left side in Figure 4-16), but at a later stage and less pronounced than for specimen REG A. This is due to the confining effects of the concrete, caused by the material expansion in combination with the reinforcement. As prescribed horizontal displacements increase, a pattern of parallel shear crack form in the wall. Further displacement increase result in the development and progress of multiple cracks, parallel to the initial shear crack. The crack pattern appears to be more regular than for the REG A simulation. The ultimate failure mode seems to be a combined shear and tension mode. The visualization in Figure 4-17 is believed to compare fair to experimental crack patterns in the wall, shown in Figure 2-13. The maximum shear capacity for this loading situation is here predicted to be at a prescribed horizontal displacement of 4.8 mm, which is slightly earlier than for the REG A specimen, and the shear force is then 1.08 MN. The ultimate failure is here estimated to be slightly more ductile than the REG A specimen, beginning at approximately 10 mm prescribed horizontal displacement.
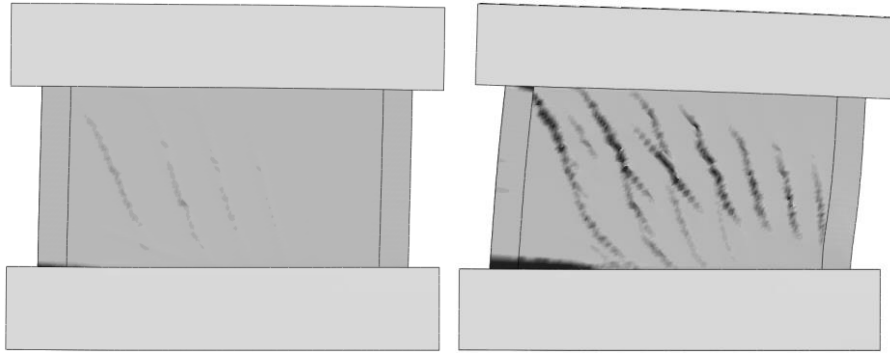
Figure 4-16 Monotonic horizontal push over response at crack initiation (1.2 mm) and maximum capacity around 4.8 mm horizontal displacement, for the ASR A1 specimen numerical simulations.
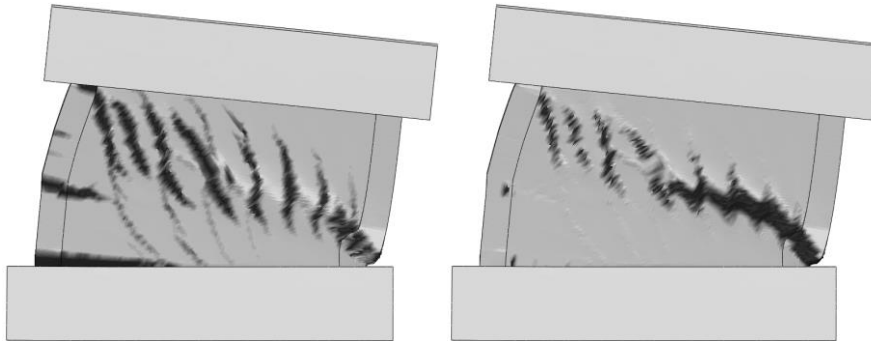
Figure 4-17 Visualization of (close to) ultimate crack pattern and failure mode for the ASR A1 specimen, to be compared to experimental results shown in Figure 2-11. Left figure show tension damage, and right figure show compression damage, at 10 mm horizontal displacement.

Figure 4-18 show the predicted equivalent reinforcement stress after isotropic concrete expansion (0.00185), and before initiation of the horizontal displacement push over event, for the ASR A1 specimen numerical simulations. Reinforcement stresses are shown at initial yield in Figure 4-19, and at 10 mm prescribed horizontal displacement in Figure 4-20. The yield stress is defined to 430 MPa, as described in section 3.5.2. Initial yield occurs at an earlier stage in the ASR affected structure, compared to the regular concrete test specimen. This is due to the prestressing effect induced by the concrete expansion, causing the initial stress state in the reinforcement. Figure 4-21 show the predicted reinforcement equivalent plastic strain at 10 mm horizontal displacement. No experimental data is available for comparisons and verification of these predictions at present time.

54
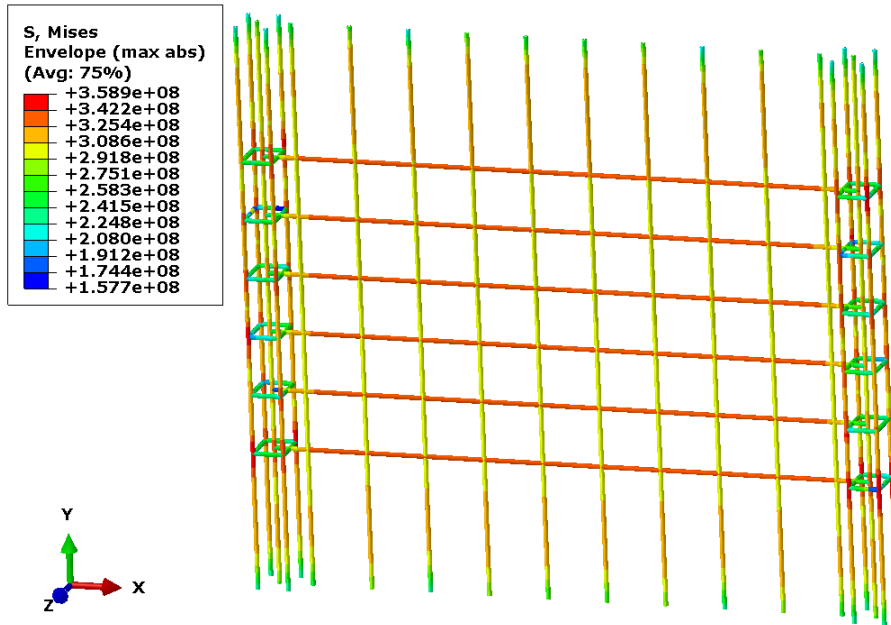
Figure 4-18 Predicted equivalent reinforcement stress after isotropic
concrete expansion (1.85 mm/m), before initiation of the
horizontal displacement, for the ASR A1 specimen
numerical simulations.
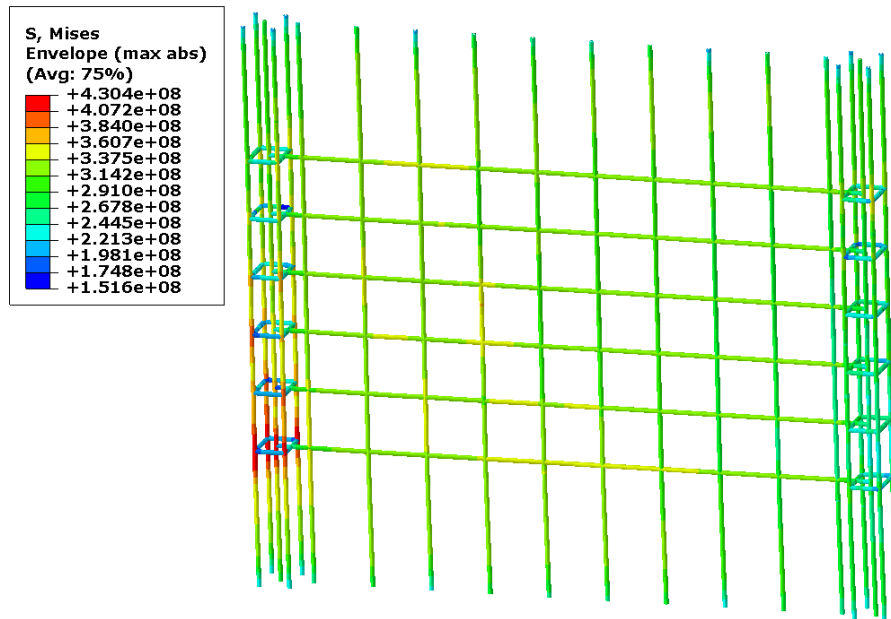
Figure 4-19 Predicted equivalent reinforcement stress, at initial yield,
at 0.8 mm horizontal displacement, for the ASR A1
specimen numerical simulations.
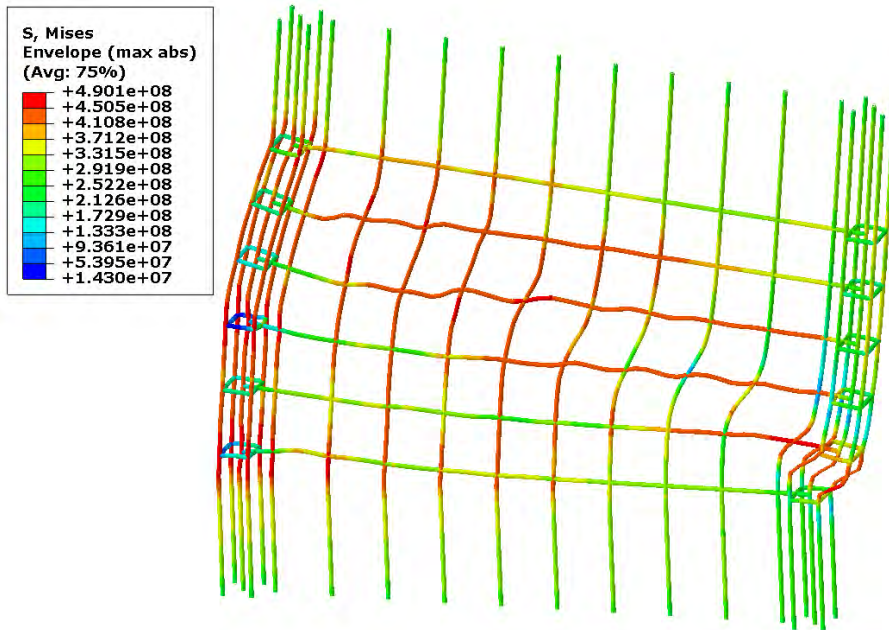
Figure 4-20 Predicted equivalent reinforcement stress at 10 mm horizontal displacement, for the ASR A1 specimen numerical simulations.
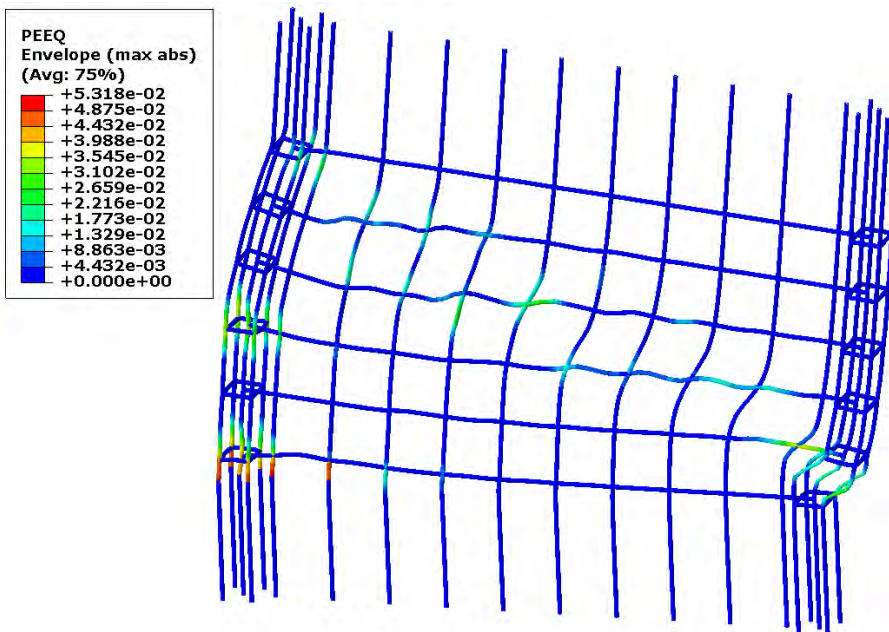
Figure 4-21 Predicted reinforcement equivalent plastic strain at 10 mm horizontal displacement, for the ASR A1 specimen numerical simulations.

4.3.2. Cyclic loading simulation results

Attempts at simulating the actual cyclic load event described in section 2.5 are described in this section for the ASR A1 specimen, analogue to the REG

A specimen described in section 4.1.2. The numerical model used is identical to the model used for the simulation of monotonic loading, described in the previous section. The prescribed cyclic horizontal displacement sequence used for numerical simulations is shown in Figure 4-8.

In conclusion, as described in section 4.1.2, cyclic loading event simulations including advanced inelastic material responses, are less successfully simulated using the CDP material model for the studied shear loaded wall. Cyclic loading (whole wall force-displacement) response are shown in Figure 4-22. Analogue to what is described in section 4.1.2, the figure show an initially fair comparison, and then a premature and rapid loss of strength.
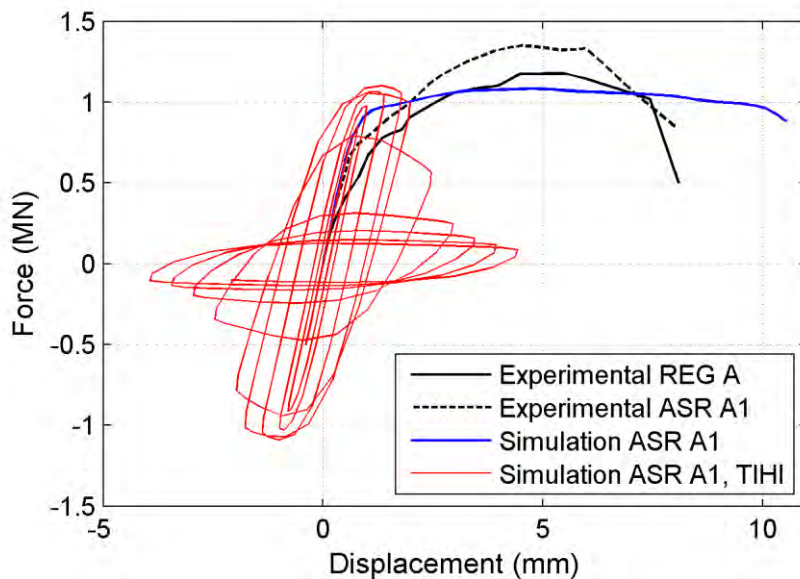
Figure 4-22 Comparison of whole wall horizontal push over capacity functions for the ASR A1 specimen experimental test and cyclic loading numerical simulation.

In terms of crack development and pattern, Figure 4-23 and Figure 4-24 show the predictions during the first couple of load cycles. One observation is that the ASR A1 specimen initiate cracking at a later stage, and to a lesser extent, than the regular concrete specimen REG A. This is due to the structural post stressing effects from the steel reinforcement, originating from the concrete material ASR expansion. This lead to formation of considerably less horizontal crack planes in the ASR A1 numerical simulation, in the wall-lower beam junction, and in the barbell wall side parts. See Figure 4-10 and Figure 4-11 for a REG A numerical result comparison to the ASR A1 numerical results in Figure 4-23 and Figure 4-24.

The ultimate failure mode predicted for the ASR A1 numerical model (see Figure 4-25) is quite similar to the REG A numerical simulation, resulting in a failure mode in the shape of an inverted flat U-shape across the wall, as the last vertical load carrying capacity of the outer barbell wall sides is exhausted.
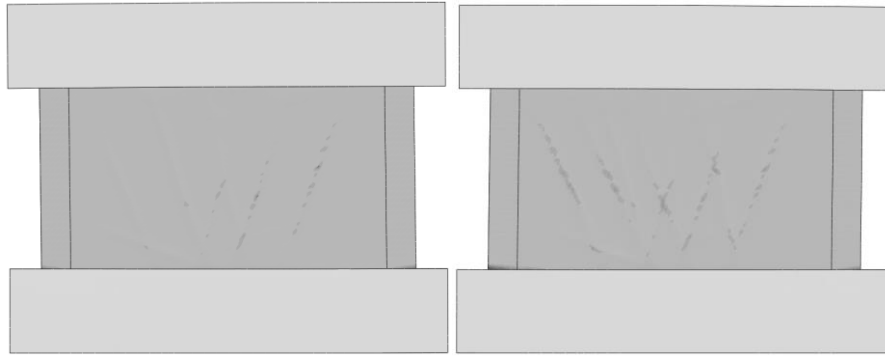
Figure 4-23 Cyclic loading response at -0.8 mm (second cycle reverse direction) and 1 mm (third cycle) horizontal displacement, for the ASR A1 specimen numerical simulations.
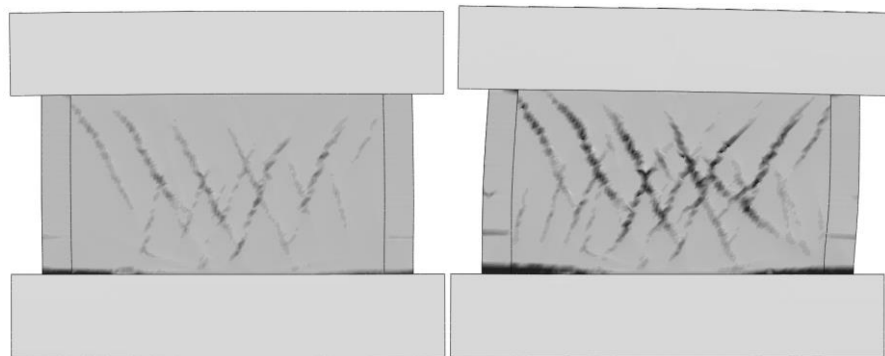
Figure 4-24 Cyclic loading response at 1.4 mm (fourth cycle) and 1.8 mm (fifth cycle) horizontal displacement, for the ASR A1 specimen numerical simulations.
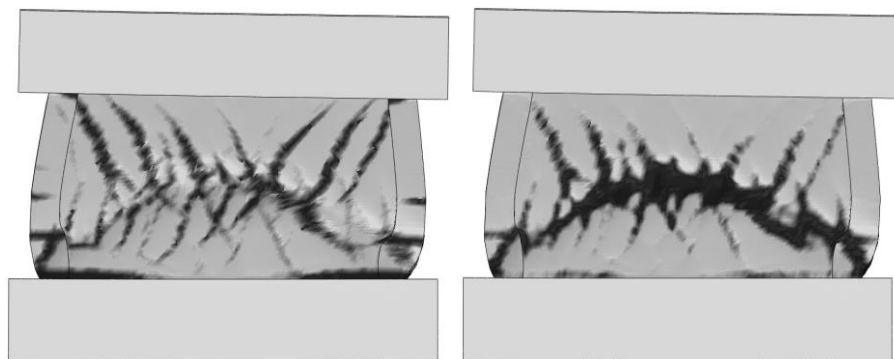
Figure 4-25 Visualization of ultimate crack pattern and failure mode for the ASR A1 specimen numerical simulations, to be compared to experimental results shown in Figure 2-11. Left figure show tension damage, and right figure show compression damage, at 2.5 mm total displacement (load cycle number 7).

4.4. Blind predictions for specimen ASR B2

In this section results from the numerical simulation of the affected specimen, ASR B2, are presented. The physical test specimen was tested at an approximate age of 1000 days, see section 2.2. Numerical modelling aspects of the ASR affected specimen are discussed in general terms in section 3.11.

As the concrete is affected by ASR, code equations for material properties evolution over time are not available in Eurocode 2 [21]. The unknown evolution of material properties over time for wall specimen REG B is therefore not accounted for, as this would result in pure guesswork. To account for changed conditions over time, the free expansion of the specimen at the test is assumed to be 0.3 % in the numerical simulations, based on simplified guessing from information in section 2.3. The expansion is considered to be the controlling factor for the ultimate capacity, although changes from the ASR A1 specimen are predicted to be small in the sensitivity analysis presented in section 4.5.9.

Due to the similarities between the numerical simulations of specimen ASR A1 and ASR B2, the results are at large similar. The ASR B2 specimen, having larger expansion and thus higher post tensioning specified, experience similar cracking but at a slightly later stage in the event.

Figure 4-26 show a comparison of whole wall horizontal push over capacity functions for the ASR B2 specimen experimental test and numerical simulations. The approximate maximum shear capacity for this loading situation is predicted to be 1.12 MN at 4.8 mm horizontal displacement.
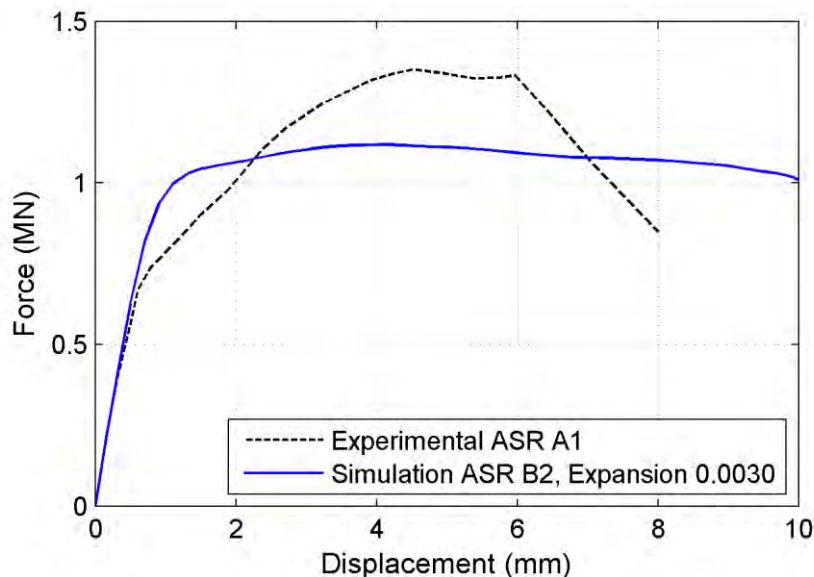
Figure 4-26 Comparison of whole wall horizontal push over capacity functions for the ASR B2 specimen experimental test and numerical simulations.

Figure 4-27 show the predicted equivalent reinforcement stress after isotropic concrete expansion (0.003), and before initiation of the horizontal

displacement push over event, for the ASR A1 specimen numerical simulations. The reinforcement in the wall is at this point in non-linear material response. The yield stress is defined to 430 MPa, as described in section 3.5.2. No experimental data is available for comparisons and verification of the predictions made at present time.
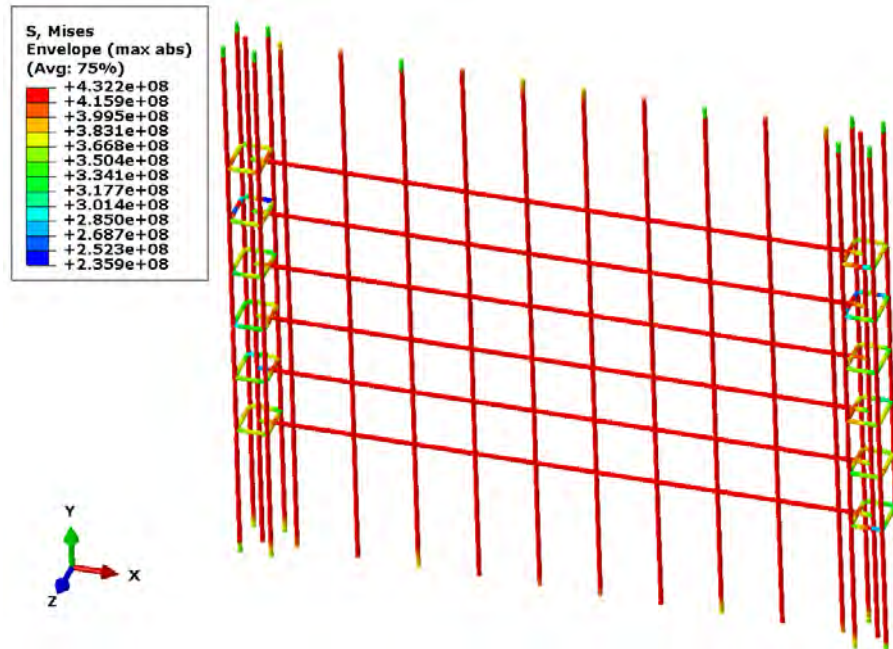
Figure 4-27 Predicted equivalent reinforcement stress after isotropic concrete expansion (3 mm/m), before initiation of the horizontal displacement, for the ASR A1 specimen numerical simulations.

4.5. Sensitivity analyses

One major benefit of using numerical simulations is the possibility to quite easily vary input parameters to study what-if-cases, something often called sensitivity analysis. Results and conclusions from selected cases of such sensitivity analyses will be presented here. Unless otherwise explicitly specified, the base state model compared to the regular concrete (REG A) model presented in section 3.6.

The general results show that numerical predictions for the studied shear wall problem in some situations may vary quite much for varied simulation input data. This result variability seems to arise due to differences in the load-path, which are here most apparent as graphical interpretations of the tensional damage parameter (here used as crack patterns). Initially stiffer whole wall response, which is not always intuitive, sometimes result in less ductile behavior.

4.5.1. Boundary conditions

Numerical model boundary conditions most often have a significant impact on simulation results, and are typically important model input parameters. In the real world however, boundary conditions are rarely as straight forward as what often is conveniently assumed in numerical simulations. To illustrate the impact of two different cases of boundary condition assumptions for the structure used within this report, this section is included. Another reason to include this particular study is because no information, data acquired concerning actual conditions at the experimental situations, are available.

Two extreme cases of rotational boundary conditions for the test specimen upper beam are selected, and presented, here. The two cases are; fully restrained in-plane rotations, and free rotation capability, as the base model described in section 3.6.

The monotonic horizontal push over response for the two different boundary conditions, and crack pattern, at 2.8 mm horizontal displacement, can be seen in Figure 4-28. It is apparent from this figure that the restrained rotational motion of the upper beam strongly governs the crack pattern developed during the event. Instead of the combined effects of both shear and in-plane moment, resulting in an inclined crack pattern and extensive horizontal cracking at the base beam, for the unrestrained rotation (to the left in Figure 4-28), the development of multiple shear cracks can be noticed for the wall responding in shear only (to the right in Figure 4-28).

Figure 4-29 is included to show the gradual increased response at 1.6 and 5.2 mm horizontal displacement, for the wall having restrained in-plane rotation at the top beam.

Figure 4-30 show a comparison of horizontal push over capacity functions for the two different extreme cases of upper beam rotation restraints models. Allowing in-plane rotations will result in a mixed mode shear and bending failure. A significant increase in whole structure ultimate capacity can be seen for the wall having restrained in-plane rotations at the top beam. This effect is valid for both elastic and in-elastic structural response. Just as for other parameters which increase the ultimate shear capacity, restrained rotations may cause a more brittle and less ductile whole wall response.

It should be noted that the two selected cases are extreme cases, and the actual behavior of the structures are likely somewhere in between this behavior, but fairly close to the top beam free rotation condition. The applied vertical load also governs this response, to some extent. Unfortunately, no experimental data to confirm the actual experimental setup in this perspective are at present time available.
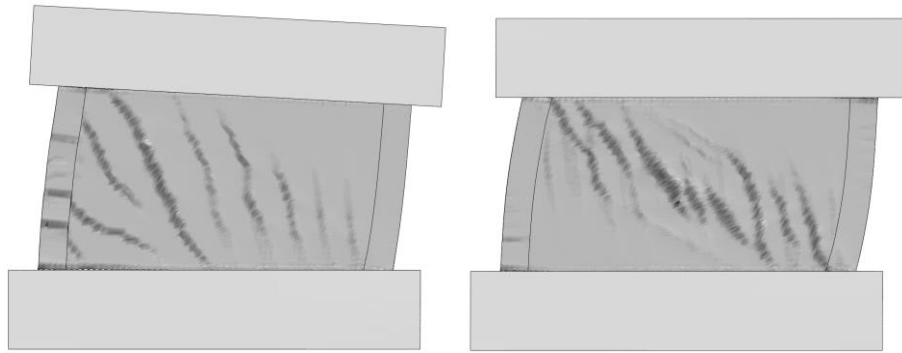
Figure 4-28 Monotonic horizontal push over response and crack pattern at 2.8 mm horizontal displacements for the free top beam rotation (left figure), and restrained in-plane rotation (right figure). Displacements are magnified 40x.
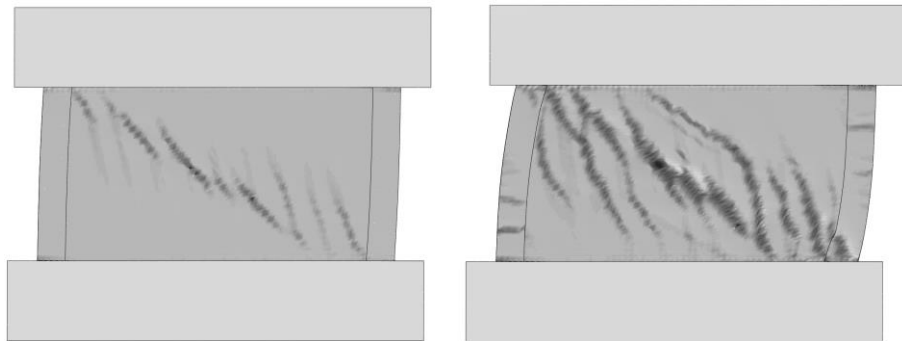
Figure 4-29 Monotonic horizontal push over response at 1.6 and 5.2 mm horizontal displacement, for the wall having restrained rotation at the top beam.
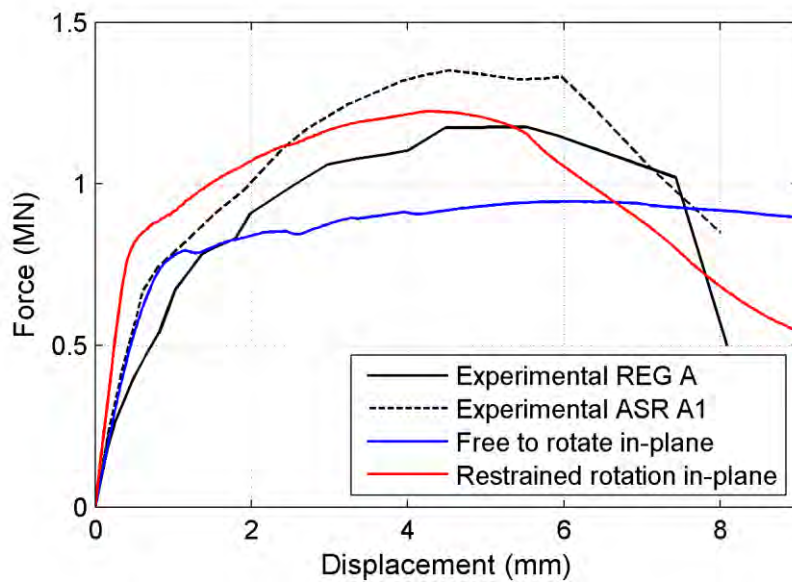
Figure 4-30 Comparison of whole wall horizontal push over capacity functions for the two different upper beam rotation capabilities.

4.5.2. Solid element selection issues

Within the work presented in this report, several types of solid element types available in the ABAQUS/Explicit solver have been tested; C3D8R (8-node brick element), C3D4 (4-node tetrahedron), and C3D10M (modified 10-node tetrahedron). These element types are described in more detail in the ABAQUS manual [4]. The reason for testing a variety of different element types were originally observed deviations in non-linear response, compared to the experimental results. The brick element model use element side lengths of 25 mm, and the tetra mesh models are split mesh from that model. Figure 4-31 show a comparison of whole wall horizontal push over capacity functions for the various tested element types. The top beam was free to rotate in-plane in all simulations, as this is expected to reflect actual conditions well.

Solid and shell elements in the ABAQUS/Explicit solver use first order (linear) reduced integration elements. For first-order elements including reduced integration, hourglass control is required to avoid hourglass modes. The reduced integration 8-node brick element, of type C3D8R, suffers from such hourglass effects for the simulated shear problem, which normally may indicate that a mesh refinement is required. In combination with the CDP material model used, this result in a substantial swelling effect in the thickness direction of the non-linear regions of the wall. This also result in a much too soft response for the wall after crack initiation. As a result, these brick elements are not selected for use for the final model.

Regular 4-node tetrahedron (type C3D4) elements are for many applications considered to result in an overly stiff structure. In addition, the resulting crack pattern formed a single diagonal band across the wall structure, which did not reflect experimental experience. The elements were not used further.

Using modified tetrahedron (type C3D10M) elements as host elements for the embedded reinforcement bars, only the corner nodes of the elements are tied to the embedded elements, by software implementation. This may result in a softer behavior than if all nodes of the element were used to tie the embedded reinforcement elements. The importance of this feature is not investigated. In the simulations carried out, the artificial strain energy was kept at a moderate level. Together with a reasonable ultimate capacity, and a realistic crack pattern, this element type was selected for further use.
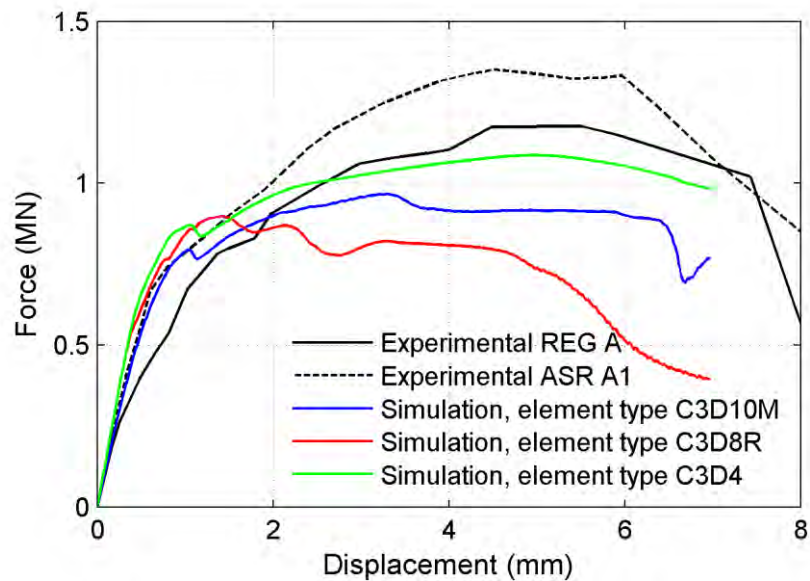
Figure 4-31 Comparison of whole wall horizontal push over capacity functions for tested element types.

4.5.3. Concrete fracture energy

Numerical simulations carried out as part of the sensitivity analyses predict that the concrete material Mode I fracture energy (GFI) influence the ductility, and crack pattern, of the studied shear wall. The ultimate shear capacity is not affected to the same degree, for the studied configurations.

The tabular definition method of the concrete uniaxial tension as a function of crack width has been used in this work, as the two-parameter definition (ultimate uniaxial tension and fracture energy) include a linear decay shape of the tension stress. The inclusion of an exponential-type decay shape has for some conditions been observed to be important, whereas for other situations this has not been an important parameter.

Figure 4-32 show a comparison of horizontal push over capacity functions for varied Mode I fracture energy of the concrete material. In the figure, it appears as defining too high fracture energy cause an excessive ductility capacity. The results may indicate that the used Mode I fracture energy, supplied from experimental data (see section 2.3), are over estimated. This may be one reason for the noted excess in ductility capacity in the REG A base numerical model used in this report. However, altering other material input simultaneously (not done here) may yield different results, which show the importance of having well defined physical material model input parameters, that are possible to determine experimentally. See discussion in section 3.5.1. The comparison in the figure also show something seen several times during the work within this project, that a seemingly logically "weaker" model (here lower GFI) may during some stage exhibit a stiffer behavior than a model that nominally should be "stronger". This is here seen as increasing GFI not consequently result in a higher capacity of the shear

64

wall, but the load paths, and crack pattern and propagation, may vary as a result of the evolution of the wall response.

Numerical predictions of the different crack patterns, crack initiation and crack propagation, for the studied cases are included below. The data shown origin entirely from numerical simulations, and how much of the response that are artefacts of the numerical implementation and material model, and how much correspond to actual physical response is not possible to determine currently. Experimental data to support, or reject, the predicted behaviors are not available at present time. However, the numerical results show that the shear loaded squat wall phenomena studied result in complex stress/strain patterns, which may be quite sensitive to input variations.
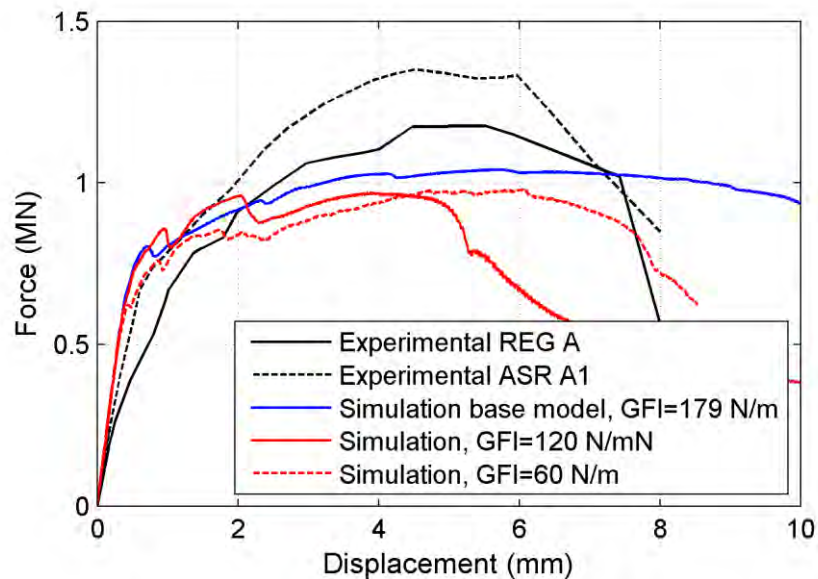
Figure 4-32 Comparison of whole wall horizontal push over capacity functions for varied Mode I fracture energy.

Figure 4-33 show visualizations of the monotonic horizontal push over response at 0.8 and 5.0 mm prescribed horizontal displacement, for the wall with a specified Mode I fracture energy of 60 N/m. Crack initiation start at the lower left junction between the bottom beam and the wall, as for all the other simulations. A 45-degree angle crack then form early in the event, reaching from the lower right side of the wall, and up to the junction with the top beam. This result in a triangle (base is upward) with primarily compression stress at the upper right side of the wall. Tensional crack progression then occurs along the lower left side of the wall, the left end barbell wall, and along the diagonal of the main wall. The final crack opens parallel to the initial 45-degree angle crack, crushing the lower base of the right barbell side wall.
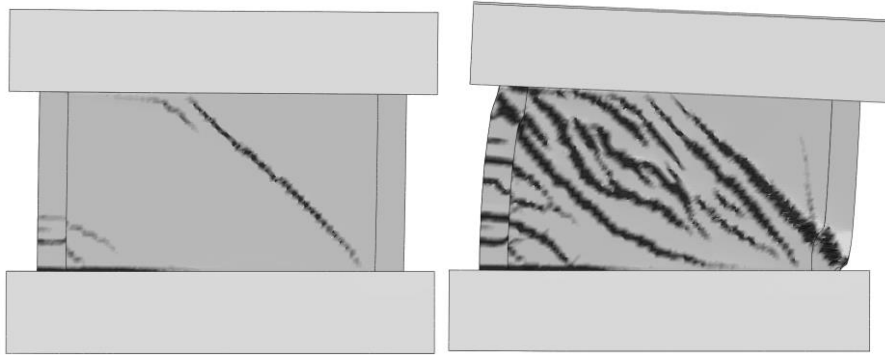
Figure 4-33 Numerically predicted crack patterns at 0.8 and 5.0 mm horizontal monotonic displacement, for concrete having Mode I fracture energy (GFI) 60 N/m.

Figure 4-34 show visualizations at 0.8 and 5.0 mm prescribed horizontal displacement, for the wall with a specified Mode I fracture energy of 120 N/m. Crack initiation and progression is here somewhat different from the case described above, in that the crack pattern consist of major cracks primarily running along, or parallel to, the wall diagonal.
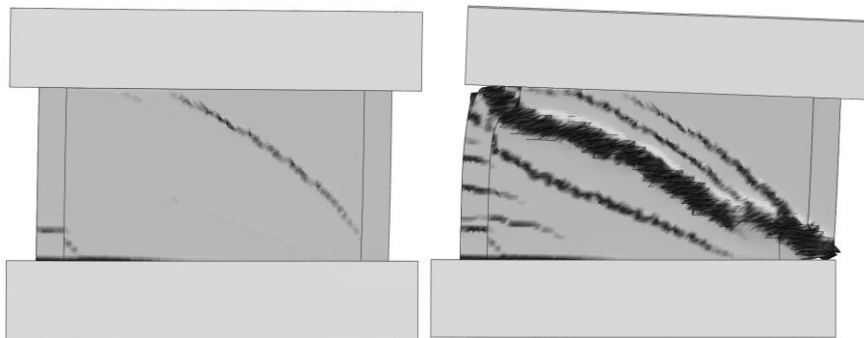
Figure 4-34 Numerically predicted crack patterns at 1.0 and 8.0 mm horizontal monotonic displacement, for concrete having Mode I fracture energy (GFI) 120 N/m.

Figure 4-35 show numerically predicted crack patterns at for the REG A test specimen base model, having Mode I concrete fracture energy of 179 N/m. The predicted crack pattern is here in general oriented at a larger angle than the other models predict. Multiple parallel cracks progressively form at the right (compressive) side of the wall. Ultimately, a band of cracks form along the wall diagonal.
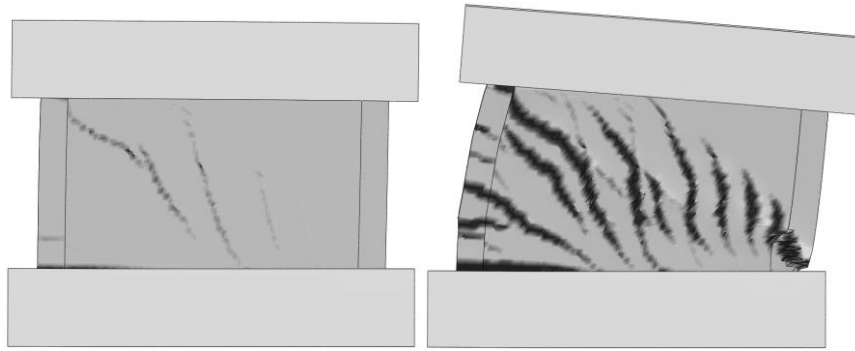
Figure 4-35 Numerically predicted crack patterns at 1.0 and 8.0 mm horizontal monotonic displacement, for concrete having Mode I fracture energy (GFI) 179 N/m.

4.5.4. Concrete compression side

Experimentally derived data for the concrete materials indicate very high ultimate compression capacity for the concrete materials used. A limited study of the influence of the ultimate compression is included. Figure 4-36 show a comparison of horizontal push over capacity functions for varied material ultimate compression in the numerical model.

The base numerical model has a specified ultimate compression of 79 MPa (see experimental data in section 2.3), and the material assigned a low compression have a specified ultimate compression of half of that. This is a very big material parameter change, and the sensitivity study is carried out on a conceptual level, not indicating that the lower ultimate compression value must necessarily represent an actual concrete material, but more to illustrate the importance of the compression side in terms of entire wall capacity.

Simulation results for ultimate compression specified from an equivalent cube test is also included. Here a rough assumption that the ultimate compression from a cylinder test is approximately 80 % of that of a cube test, has been used. Differences to the specified ultimate compression value from cylinder tests are seemingly small, for the configuration in this example, but may be important for other configurations. See section 3.5.1 for further discussion on material model input.
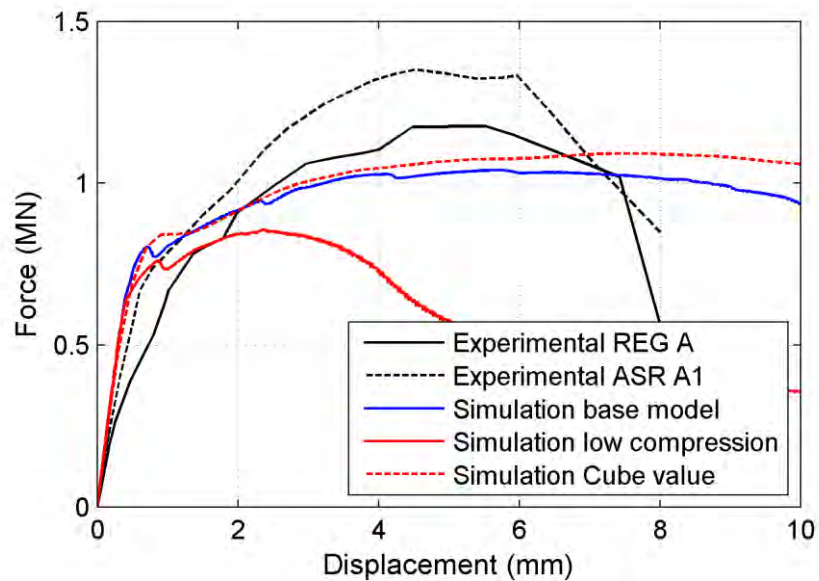
Figure 4-36 Comparison of horizontal whole wall push over capacity functions for varied material ultimate compression in the numerical model.

4.5.5. Concrete elastic stiffness

Experimentally derived data for the concrete materials indicate very high elastic stiffness for the concrete materials used. A limited study of the influence of the elastic stiffness is therefore also included. Figure 4-37 show a comparison of whole wall horizontal push over capacity functions for varied concrete material elastic stiffness in the numerical model.

The base numerical model has a specified elastic stiffness of 47 GPa (see experimental data in section 2.3), and a model using a lower elastic stiffness of 40 GPa has been included. This is a realistic material parameter change, and illustrate the (low) importance of the elastic material stiffness in terms of entire wall capacity.
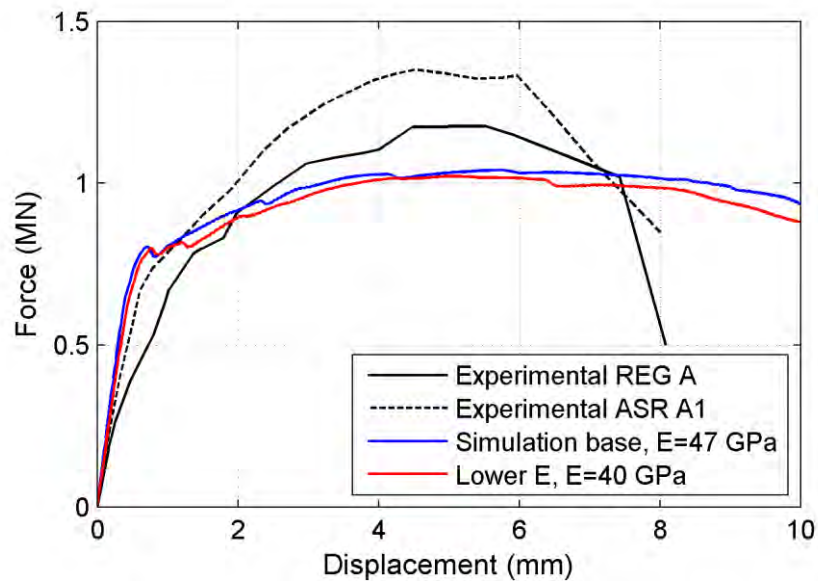
Figure 4-37 Comparison of horizontal whole wall push over capacity functions for varied concrete material elastic stiffness in the numerical model.

4.5.6. Influence of vertical load

The external vertical load has an influence on the ultimate shear capacity for the studied shear problem. Figure 4-38 and Figure 4-39 show a limited comparison of predicted horizontal push over capacity functions and crack patterns for varied vertical load. The base simulation has an external vertical load of 800 kN, and in the sensitivity analyses this load have been varied with a value of ±200 kN, to show example result differences.

The most note-worthy result change is for the numerical simulations of the decreased vertical load. The ductile behavior has here reached a threshold value (cliff-edge effect) as the normal force were lowered. The resulting failure mode is here predicted to be in the form of a distinct diagonal crack, parting the wall in two relatively equal triangle shaped parts. The increased vertical load seems to result in more evenly spaced crack pattern than the case for the base simulation configuration, REG A. The predicted resulting crack patterns are shown in Figure 4-39.
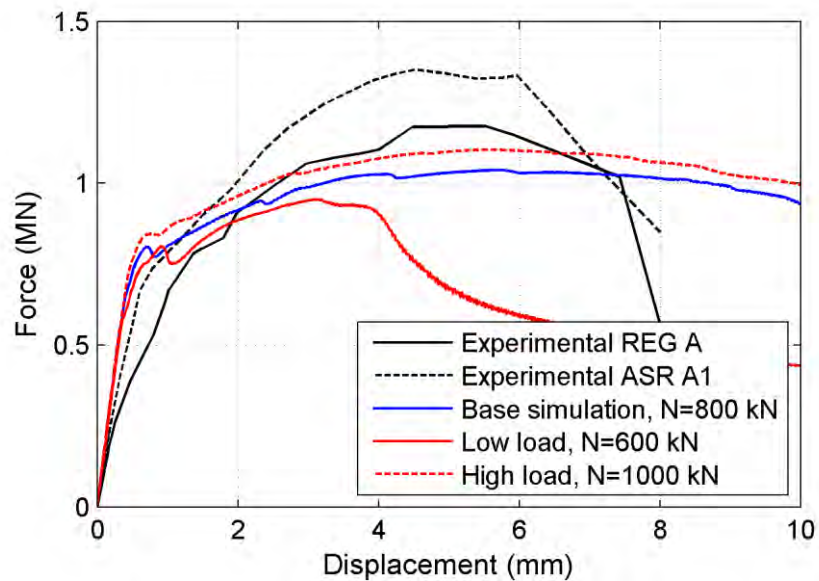
Figure 4-38 Comparison of horizontal whole wall push over capacity functions for varied vertical load.
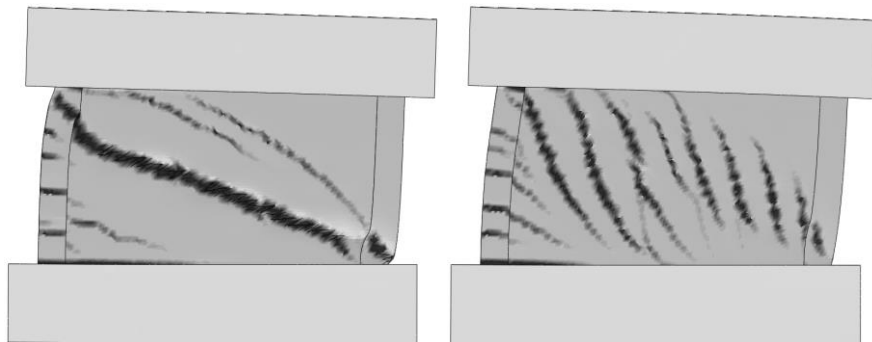
Figure 4-39 Numerically predicted crack patterns at 4 mm horizontal monotonic displacement. Left figure show simulation result for decreased vertical load, and right figure increased load results.

4.5.7. Shell element model

For engineering simulations of entire nuclear structures, practical aspects, as for instance model size, and convenient concrete cross section output availability, sometimes make shell element models an attractive option. To consider this practical aspect of numerical model refinement level, shell element models has been created to compare results, in terms of shear failure mechanism and ultimate capacity, to the solid element model otherwise used and presented in this report. The shell models are not described in much detail here, but are created to be equivalent to the solid element base model otherwise used in this chapter. To illustrate the effects of FE mesh refinement, three different spatial discretizations are selected, using the S4R

4-node general purpose shell element with reduced integration and hourglass control [4]. Element side lengths selected are; 100 mm, 50 mm, and 25 mm.

The upper beam is free to rotate, as the base model described in section 3.6 and 4.5.1. This free rotation result in a mixed bending and shear structural response where the prescribed horizontal motion, translating the upper beam to the right in the figures below, give tension on the left side and compression at the right side in the figures.

The implementation of steel reinforcement modelling differs in the shell model, from the solid element model. In the solid element model, discrete bar elements are embedded into the solid elements, whereas in the shell element model this approach is not supported. Instead, smeared rebar layers are used. This result in a model in which reinforcement is available in every concrete element, and localized effects from cracking are less pronounced.

Results from this study include the observation that even a fairly course spatial discretization for the shell element model, to some degree, capture the overall structural response, compared to models using short element sides. Responses in the walls are initially elastic, until crack initiation at the tension side (left in Figure 4-40) at the wall and lower beam junction. After that, a diagonal crack area propagates from the wall upper left side to the lower right (compression side), dividing the rectangular shaped wall into two triangles, as the horizontal movement of the upper beam progress. In the models using short element sides, an initial diagonal crack with an angle of more than 45° form, but as the horizontal force increase an entire band of such cracks develop, and the final horizontal crack span over the entire wall width. This final diagonal crack then has a much more slanted angle. As the lower end of the right end wall break in compression, the whole wall structural capacity is rapidly decreasing. For course element discretization, crack patterns are naturally smeared over a larger geometric area. As element size decrease, crack patterns tend to be more localized, which can be seen in Figure 4-40.

Figure 4-41 show a comparison of horizontal whole wall push over capacity functions for the different tested spatial discretizations of the shell element numerical model. For the studied load case, the in-plane shear motion activates a considerable amount of artificial strain energy in the model due to the element formulation of the 4-node reduced integration shell elements. This result in unphysical non-linear responses in the numerical model for the load situation, which is the major contributing factor to the discrepancy between the observed numerical response and the experimental results. A typical indication of this problem, coarse element discretization give a softer structural behavior than fine element discretization, can be seen in the figure. In addition, for the coarse 100 mm element side model, the whole structure stiffness increase as damage progress, which is also an (un-physical) indication of this effect. The effect of dominating artificial strain energy for the problem may also result in an insensitivity to material parameter changes, not seen when using the C3D10M elements to model the wall. In conclusion, for the studied shear wall case, the used shell element modelling technique result in the prediction of a low ultimate nominal shear capacity for all the different spatial discretizations used, compared to the experimentally measured capacity. However, structural ductility may be overestimated, and a suitable ultimate shear deformation criterion should be

used to avoid this. As a consequence of the above, great care should be taken when using the studied reduced integration shell elements result in non-linear material response, for structural assessments of in-plane shear dominated problems for squat concrete walls.

As a practical note, for the three-dimensional shell elements available in ABAQUS/Explicit, transverse confining effects from ASR expansion are not possible to model.
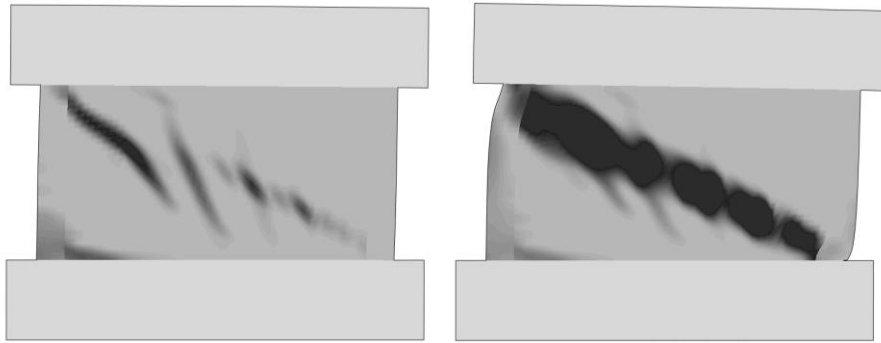
Figure 4-40 **Monotonic horizontal push over response at 1 and 3 mm horizontal displacement, for a wall shell model using element side length 25 mm.**
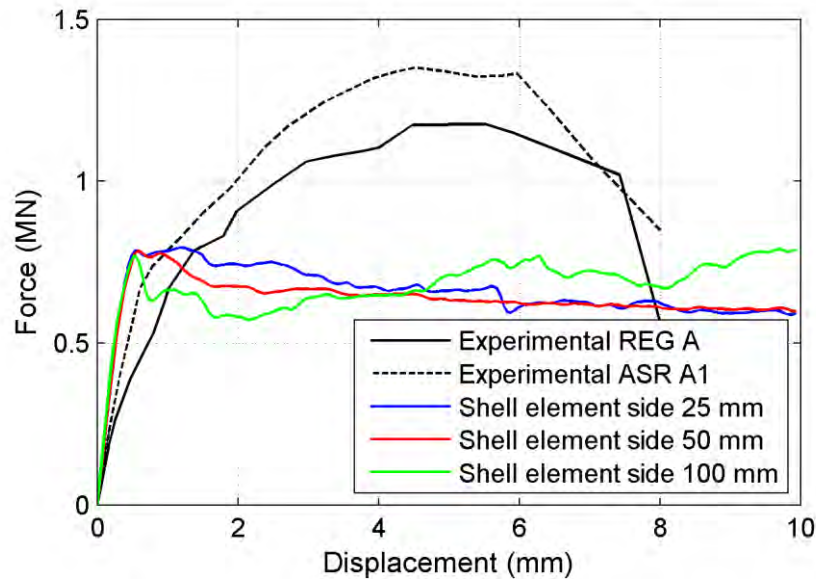
Figure 4-41 **Comparison of horizontal whole wall push over capacity functions for the different spatial discretizations of the shell element numerical model.**

4.5.8. Type of reinforcement modelling

For the solid element model, two types of elements have been tested for the steel reinforcement model of the concrete structure; truss elements (type

T3D2 [4]), and beam elements (type B31 [4]). The truss element of type T3D2 is essentially equivalent to a spring element.

Normally truss elements, having the capability to transfer forces in tension or compression only, are often used to model reinforcement in structural assessments. For most applications, this is an appropriate approximation of the steel reinforcement intended load transfer capability. Beam elements, being computationally somewhat more expensive but capable to transfer moment, are often not used because they are unnecessarily complex for the task. However, in the case of a shear dominated load situation for a relatively slender wall segment, and ultimate capacity evaluation, the beam element is here considered a more appropriate element selection due to differences in both ultimate capacity and crack patterns between the two modelling alternatives. This difference has been noted to be small, or large, depending on the specific problem conditions.

Figure 4-42 show an example comparison of horizontal push over capacity functions for the two different reinforcement models. The models here compare well until the damaged volume in the wall is unable to transfer forces across the concrete material alone. For situations where this effect becomes important, most likely localized concrete-reinforcement interaction effects may also be of interest. The used numerical model does not include any interface nor bond-effects.
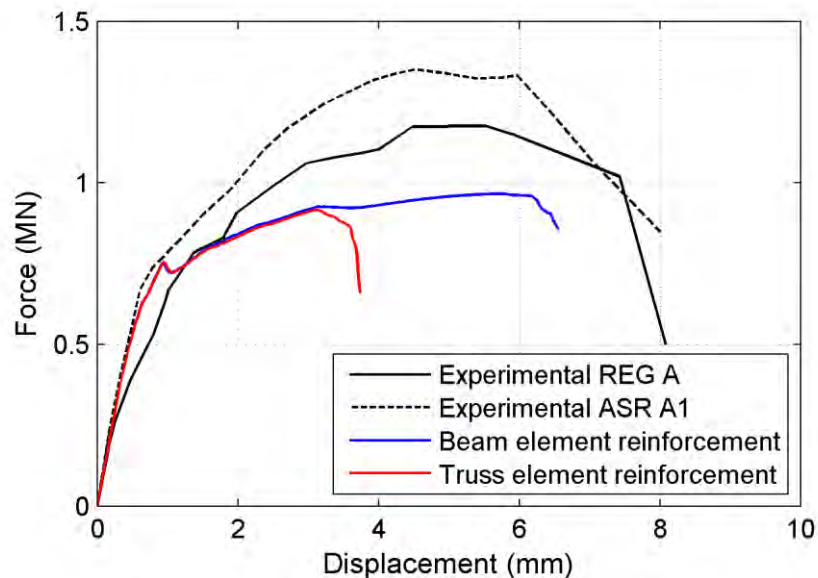
Figure 4-42 Example comparison of horizontal whole wall push over capacity functions for the two different reinforcement model alternatives.

4.5.9. Confining effects - ASR concrete expansion

General conditions for the used numerical modelling of ASR effects are discussed in section 3.11. In the used numerical model, all concrete volumes including the elastically modelled upper and lower beams, are assumed to be

of the same reactive concrete type concerning the expansion. Uniform and isotropic material expansion is used in this study.

The effects of including the ASR concrete expansion, to capture confinement effects, has been studied for the shear wall configuration under investigation. The over-all effects on structural shear resistance of ASR affected structures are not straight forward for the general case, but determined by material strength losses, combined with the possible positive effects of structural element confinement from material swelling in combination with structural element restraints. The structural element restraints are here limited to the reinforcement, as no external boundary conditions are applied (model free to uniformly expand during expansion phase).

A few different uniform and isotropic material expansion ratios have been simulated, ranging from 0.05 %, to 0.3 % (see section 3.11), using the experimentally derived material parameters of the ASR A1 test specimen (see Table 2-1). In addition, expansion up to a very large value of 1 % has been simulated, to study the potential effects for the wall of this extreme. Figure 4-43 show a comparison of horizontal whole wall push over capacity functions for different ASR expansions. Expansion up to around 0.3 % increase the ultimate capacity of the shear wall in this limited study. Around that level of expansion, the reinforcement steel utilization become a limiting factor for the wall, and further expansion become negative for the wall ductility, and to a lesser extent for the ultimate capacity. This seem natural, as the yield stress often is related to the 0.2 % strain value. It appears as very large expansion is needed for the reinforcement to become a limiting factor. For practical applications, the long-term confining effect may decrease due to relaxation of the reinforcement steel. Note that no material parameters have been adjusted in this numerical study.
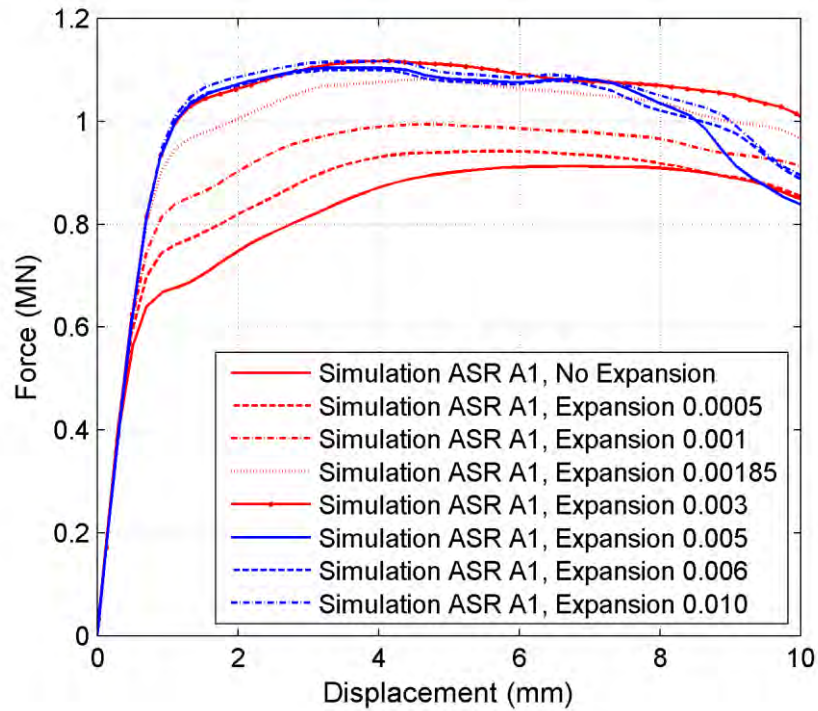
Figure 4-43 Comparison of horizontal whole wall push over capacity functions for the different ASR expansions.

4.5.10. Influence of dilatation angle

The dilation angle of the material model alters the volumetric behavior of the material model, and has an influence on the studied shear wall problem. The dilation angle ψ is measured in the p-q plane at high confining pressure, and indicates the ratio between the volume change and the shear strain. The dilation angle value for concrete is commonly specified in the range of 30° to 40°, according to [4]. This material model input parameter is considered difficult to experimentally determine, and is not by any means a usual material parameter to determine for concrete. See sections 3.4.2 and 3.5.1 for further discussions.

The angle is chosen to be 38° for the base simulation otherwise used in this report, based on the work in [4]. In the sensitivity analyses carried out this value have been varied between 10° and 56°, to show example result differences. Figure 4-43 show a limited comparison of predicted horizontal push over capacity functions for varied input values of the dilation angle. It is concluded that the maximum shear force capacity of the wall seems to be less sensitive for variations of the dilation angle input parameter than the evolution of whole wall force-displacement function.

The most note-worthy result change is for numerical simulations of chosen dilation angles between a range below and above around 34°. The resulting crack pattern and failure mode is in this range predicted to be substantially different for small changes of this parameter. Numerically predicted resulting crack patterns are shown in Figure 4-44. The two very different

responses of the shear wall seem to develop already in the earliest states of non-linear response, and the initial stress field is believed to have a great influence on the yield surface and this behavior. Whether this is purely a numerical feature, significant to the used material model, or if it may also be experimentally confirmed, is not known at present time. This issue is noted for this studied shear wall problem, and considered a great concern, but not pursued further within the work presented in this report.
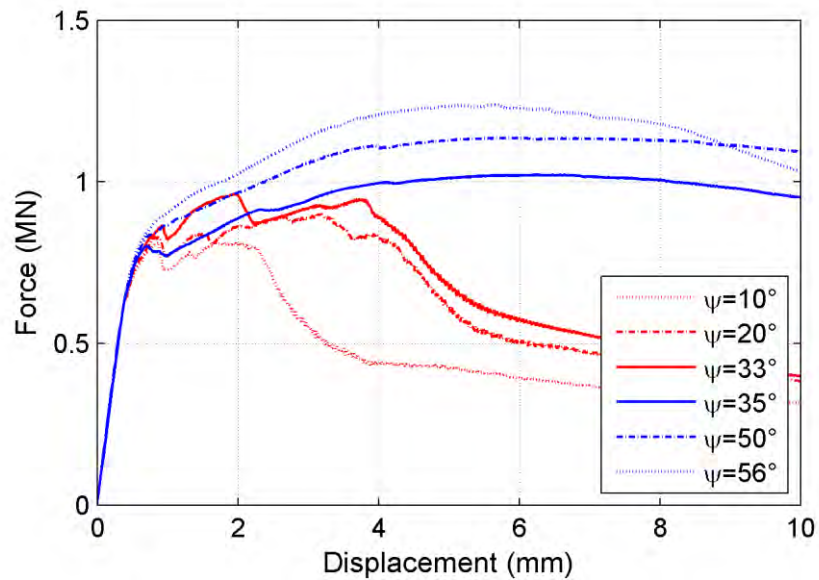
Figure 4-44 Comparison of horizontal whole wall push over capacity functions for selected input values of the dilation angle.
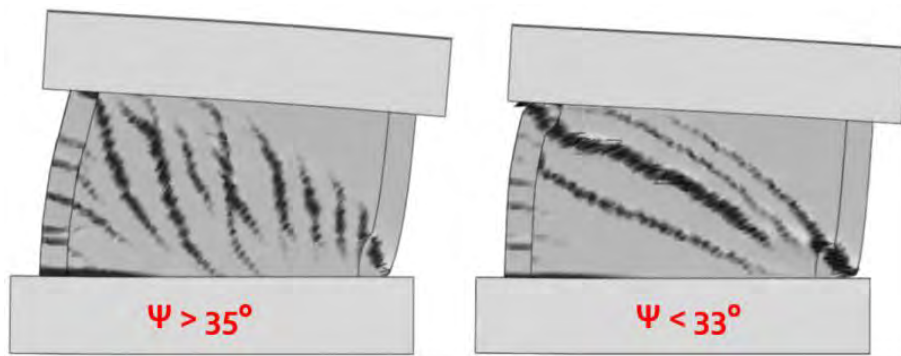
Figure 4-45 Numerically predicted crack patterns for horizontal monotonic displacement. Left figure show simulation result for dilation angle set to 35°, and right figure 33°.

4.6. Comparisons to conventional design

4.6.1. Introduction

To assess design code margins for the studied case, experimental and numerical results are compared to a limited set of conventional design code shear capacity. For Swedish conditions design code is selected according to recommendations in the design guide DNB [24]. The studied wall was designed using code equations for shear friction, according to [2]. However, the studied experimental test specimens were constructed (cast) in one piece with no division into different casting parts during construction.

There are no specific design code provisions for squat reinforced concrete shear walls included in the Eurocode EC2 [21], nor EC8 [25], design codes [26]. It should also, in this context, be mentioned that Eurocode for seismic design, EC8 [25], explicitly does not apply to nuclear structures.

Code calculations in this section include regular, e.g. non-ASR affected, structures only, as no code equations for ASR degraded nuclear structure are currently available. Concrete material properties used in the calculations reflect equivalent design values estimated based on the 28-day experimental material data presented in section 2.3. The favorable compressive vertical force of 800 kN is accounted for in the calculations.

4.6.2. Result summary

The design code shear capacity according to section 6.2.5 in EC2 is calculated to 1360 kN for the wall as a whole (see section 4.6.3). Conservatisms lowering the capacity include the decrease of the parameter c by a factor of 2 (dynamic loads), and a conservative assumption of active wall reinforcement in the barbell end walls, see section 4.6.3. The fact that this value still exceeds the experimentally measured shear force capacity (see Table 4-1) may come from the actual load situation in the experiments, and the resulting fracture mode, as this appears to have been a combination of shear and a bending moment. This due to the unrestrained in-plane rotation of the top beam as discussed in section 4.5.1 and visualized in Figure 4-2. This load situation is quite different from an assumed uniform shear stress in the capacity calculations. Nevertheless, this loading situation may be realistic for a shear wall as the one studied, and the code equation capacity here exceed the experimentally derived capacity of the studied wall. Using the shear friction design option is consequently non-conservative, and not recommended for the studied design situation.

The beam shear capacity for a compressed section, $V_{Rd,c}$ is calculated to 230 kN for the studied case (see section 4.6.4). This value is considerably lower than the value obtained using the formula for shear friction, partly due to the uncertainty in the shear fracture mode, and considered a lower bound value for the shear capacity. This calculated shear capacity is also considerably less than the experimentally derived shear capacity.

4.6.3. Shear friction in SS-EN 1992-1-1

No explicit design code provisions for shear capacity of reinforced concrete squat shear walls are included in the Eurocode 2 (EC2) [21]. However, in line with the work presented in [26], section 6.2.5 of EC2, "Shear at the interface between concrete cast at different times", may provide an approximation of the design shear capacity between the wall and base beam part of the specimen. This EC2 design provision showed the highest sensitivity to the wall normal stress (vertical load) of the design equations studied in [26], and the highest shear capacity, regardless of concrete strength or reinforcement content in the wall. The fracture mode considered is an even shear fracture along the entire casting interface.

To derive a conventional design shear capacity per EC2, a concrete quality class of a fairly high strength concrete, corresponding to C45/55 according to Table 3.1 in EC2, is assumed here for the calculations. This choice is based on the 33-day test results presented in [13], where the cylinder strength is given to 53 MPa. Calculations of the shear capacity using the shear stress at the interface between concrete cast at different times, section 6.2.5 of EC2, are included below.

v_{Rdi} is the design shear resistance at the interface, given by equation 6.25 in EC2:

$$v_{Rdi} = c\,f_{ctd} + \mu\,\sigma_n + \rho\,f_{yd}\,(\mu\,\sin\alpha + \cos\alpha) \leq 0.5\,\nu\,f_{cd}$$

The design shear resistance in this equation consist of three parts, governed by; 1) the design concrete tensile strength ($c\,f_{ctd}$), 2) the normal stress at the interface ($\mu\,\sigma_n$), and 3) the reinforcement crossing the interface ($\rho\,f_{yd}$). With values discussed below, v_{Rdi} is calculated to 8.85 MPa for the studied case. This in turn give a whole wall design shear force capacity of ($V = v_{Rdi} \times A_i$) 1360 kN. Design shear resistance per equation 6.25 in EC2, divided into the different parts of the equation are shown in Table 4-2. Values used in equation 6.25 in EC2 are presented below. It is noted from the values in the table that the vertical load and the reinforcement content have large impacts on the wall capacity, and the tensile strength influence less.

Table 4-2 **Design shear resistance per equation 6.25 in EC2, divided into the different parts of the equation.**

Shear resistance part of equation 6.25 in EC2 [21]	Shear stress at interface (MPa)	Shear force at interface (kN)
Design tensile strength dependent part	0.56	87
Normal stress dependent part	4.77	734
Reinforcement dependent part	3.52	542
Summary	8.85	1360

Calculation input variables

The two factors depending on the roughness of the interface, c is set to 0.5, and μ to 0.9, to obtain the maximum allowable shear transfer capacity, as the section considered is not an actual construction joint, but rather cast at one

time. Under fatigue or dynamic loads, the values for c in should be divided by a factor of 2 (i.e., c = 0.5 / 2 = 0.25). The used reduction of c reduces the wall shear capacity.

The design compressive strength, $f_{cd} = \alpha_{cc} f_{ck} / \gamma_C = 37.5$ MPa (equation 3.15 in EC2), is calculated as defined in section 3.1.6 (1)P, where f_{ct} is 45 MPa. α_{cc} is a coefficient taking account of long term effects on the compressive strength and of unfavorable effects, resulting from the way the load is applied. The recommended value in the National Annex is 1.0. The partial factor for the reinforced concrete material for ultimate limit state in an accidental design situation, γ_C, is 1.2, according to Table 2.1N.

The design tensile strength, $f_{ctd} = \alpha_{ct} f_{ctk,0.05} / \gamma_C = 2.25$ MPa (equation 3.16 in EC2), is calculated as defined in section 3.1.6 (2)P, where $f_{ctk,0.05}$ is 2.7 MPa. α_{ct} is a coefficient taking account of long term effects on the tensile strength and of unfavorable effects, resulting from the way the load is applied. The recommended value in the National Annex is 1.0.

A_i is the area of the joint/interface (0.154 m^2), here calculated as the wall section width ($b_i = 0.1$ m) times the wall length (1.3 m), and including the thickness of the barbell end walls (2 x 0.12 m). The wall length l_w, is then 1.54 m. Barbell sections outside of the wall thickness is disregarded from here, although this material does contribute slightly to the structural capacity. Geometric dimensions of the test specimen are visualized in Figure 2-1.

σ_n is stress per unit area caused by the minimum external normal force across the interface that can act simultaneously with the shear force, positive for compressive forces. The normal stress is calculated as the total vertical force divided by the interface area. The vertical forces at the lower wall-beam interface are the external vertical force (800 kN) plus the weight from the wall and the top beam (16 kN), in all 816 kN. σ_n is then calculated as 816 / A_i = 5.3 MPa. This stress is considered relatively high, and at the end contribute considerably to the final shear capacity of the wall.

A_s is the area of reinforcement steel crossing the interface. In all, 20 vertically oriented M10 reinforcement bars exist in the wall, 12 bars in the actual wall element, and 4 bars in each of the two barbell end walls. The reinforcement here considered is the reinforcement of the wall element only, as this reinforcement is evenly distributed over the wall length. However, in practice, the vertical reinforcement of the barbell sections interacts with the wall and do increase the capacity to some extent. The radius of each M10 bar is 5.65 mm. A_s is then 12 cm^2. In case all 20 bars are considered, A_s would increase to 20 cm^2, and the shear capacity of the structure would increase.

The reinforcement ratio, ratio between steel and concrete cross section area, ρ, is calculated as: $\rho = A_s / A_i = 0.0012 / 0.154 = 0.0078$

The reinforcement steel design yield stress, f_{yd}, is defined as $f_{yd} = f_{yk} / \gamma_S$. f_{yk} is here set to 500 MPa. The partial factor for the reinforcing steel material for ultimate limit state in an accidental design situation, γ_S, is 1.0, according to Table 2.1N in EC2. f_{yd}, is then 500 MPa.

The condition that $v_{Rdi} \leq 0.5 \, v \, f_{cd}$ (11.1 MPa) is fulfilled. v is a strength reduction factor for concrete including shear cracks (see section 6.2.2 (6) in EC2), calculated as (equation 6.6N) $v = 0.6 (1 - f_{ck} / 250) = 0.59$.

The angle of reinforcement, α, is 90 degrees relative to the interface surface.

4.6.4. Beam shear capacity SS-EN 1992-1-1

As a lower bound of the design shear capacity, section 6.2.2 of EC2 [21], "Members not requiring design shear reinforcement", is used as a complement to the calculations above. This expression is valid for beam type of structural members, which this wall not fulfill the geometric properties of. In addition, the expression does not consider the capacity increase due to shear reinforcement.

The shear resistance of regions cracked in bending, of prestressed single span members without shear reinforcement, may be calculated using the expression (6.2a in EC2):

$$V_{Rd,c} = [C_{Rd,c} \, k \, (100 \, \rho_I \, f_{ck})^{1/3} + k_1 \, \sigma_{cp}] \, b_w \, d$$

With values discussed below, $V_{Rd,c}$ is calculated to 230 kN for the studied case.

The calculation input variables used in the formula above (expression 6.2a in section 6.2.2 of EC2) are specified in section 4.6.3 above and therefore nor repeated here.

4.6.5. Numerical simulation capacity comparison

To compare the design code equation shear capacity to the predicted shear capacity using numerical simulation, a simulation using 28-day material parameters corresponding to the EC2 C45/55 concrete was carried out. This information is given as a compliment to the result otherwise given in this report, where best estimate material input are used for the numerical simulations.

Concrete strength values used are given above. The elastic stiffness was set to 36 GPa, according to EC2. The concrete material was assigned a mode I fracture energy of 107 N/m for the used material model in the numerical simulation. Guidance for this material model parameter is not available in EC2.

Figure 4-37 show a comparison of horizontal whole wall push over capacity functions between the experimental results, numerical results for the best estimate material, and the EC2 design code based C45/55 concrete material in the numerical model. The ultimate shear capacity of the studied wall is here 860 kN, using EC2 code based material input values for the numerical simulation. This value is concluded to result in a conservative estimate compared to code equations and experimental results.
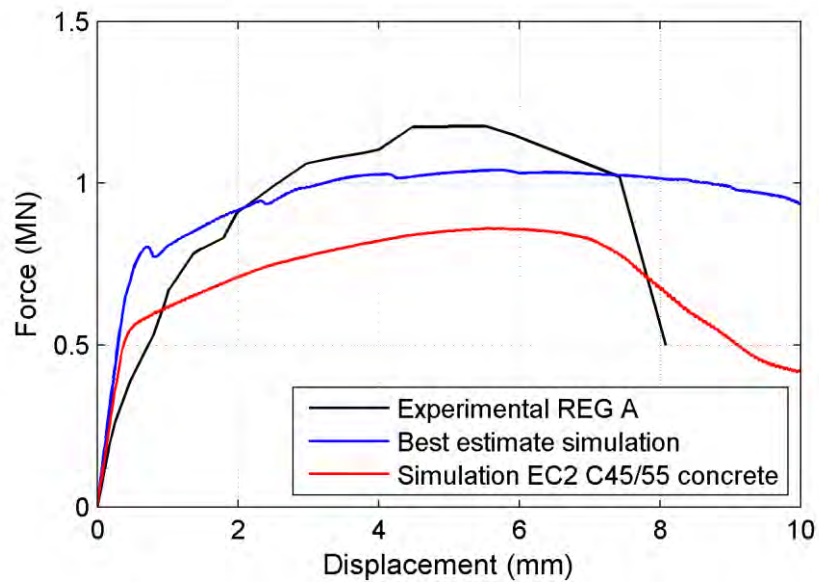
Figure 4-46 Comparison of horizontal whole wall push over capacity functions between the experimental results and numerical results for the best estimate material and the EC2 design code based C45/55 concrete in the numerical model.

5. Discussions

5.1. Overview comparisons between experimental and numerical results

Shear response of reinforced concrete structures include complex stress states, and a combination of experimental testing and numerical simulations may significantly increase the understanding of the phenomenon involved. In this report, presented results indicate a capability of the used numerical tool (ABAQUS/Explicit and CDP material model) to simulate the experimentally observed effects of advanced non-linear material behavior for a monotonic shear load event, see section 4.1. For a cyclic load event, the numerical prediction capability of the studied shear problem seems to be less satisfactory, depending on spurious features of the used material model.

The intentions for the numerical simulations have been to accept experimentally derived and delivered material properties as is, and to consider these values best estimate material properties, without modifying these. Some questions related to experimentally derived material properties do however remain, and possibly the preformed sensitivity analyses indicate that different material property input would result in better correlation between experimental and numerical results. This path has however not been pursued, as experimental data and results are not statistically assured, and the experimental data has been considered as indicative results. This non-adjustment of the material model input to some extent explains the ductile behavior seen in many the numerical simulations, when compared to experimental results.

In addition, the use and acceptance of the commonly accepted material parameters as input for numerical simulations is also an open question, which is perhaps mostly interesting in the case of best-estimate numerical simulations (as opposed to a design situation, where conservative assumption are targeted). The only parameter investigated in some depth is here the use of the ultimate compressive stress from cylinder test specimens (see section 3.5.1). This is concluded not to be a material parameter, but a combined value from both material and specimen geometric shape, which can never be considered a material parameter to be used in a constitutive model. Instead, the compressive strength from cube specimen tests appear to be close to a true material parameter. For a design situation, the lower ultimate compression value produced by using cylinder specimen tests, instead of cube tests, may for most situations be considered a reasonable conservative approach for structural assessments. The same type of material model input assessments must however be made for all other input material parameters used, to provide the possibility to make informed decisions when selecting model input.

Another very important, and not resolved issue, is the question of the exact interactions with surrounding structures and loading equipment during physical testing. This issue has been proven to affect numerical simulation output to a certain degree, and need to be understood quite well. This is an

observed factor of uncertainty in the comparisons between experimental and numerical results.

5.2. Relevance for assessments of an actual NPP structure

The studied, reduced scale, 100 mm thick shear wall specimens used in the experiments include a single layer of orthogonal web reinforcement, located at the wall center surface. For the ASR affected concrete walls in the experiments this mean no, or very little, confining pressure in the wall thickness direction. This reinforcement design differs from current design practice of reinforced concrete walls in safety related structures at nuclear power plants, but may agree better with the design of structures at some existing plants.

The purpose of this numerical work is however to study to what extent the results produced by the used numerical tool compare to experimental results, to evaluate the suitability of the used numerical method for shear wall problems. In doing this, the limited amount of experimental results, not being statistically assured, should also be kept in mind. At a whole, it appears as the ultimate capacity in this shear wall problem may be predicted satisfactory, and crack patterns and the failure mode compare reasonably well in visual comparisons. The ductility of the wall for some input choices have been overestimated, which is a concern, and in practical cases some strain limitation criteria may be used to prevent this.

5.3. Comparisons to design code shear capacity

A limited study, including EC2 only, to assess conventional design code margins compared to experimental and numerical results for the studied case, were included in this work (section 4.6). It is concluded that the design shear friction code equation capacity exceeds the experimentally derived shear capacity of the studied wall. The reason for this is different load and fracture mode assumptions. It is recommended that further work along this direction is pursued, preferably including also nuclear codes ASCE 43-05 [27] and ACI 349 [28].

5.4. Comparisons between regular and ASR affected structure

The experimental observations of the ASR affected structures, here meaning the increase in shear capacity although having a weakened material (see sections 2.3 and 2.6), were numerically confirmed, even for the simplified engineering approach used. Conceptual differences were studied and explained as mainly resulting from confinement effects due to the internal swelling induced by the chemical reactions. See sensitivity analysis in sections 4.5.9 and 4.3. The confinement effect origin from the post stressing of the embedded reinforcement steel, not from boundary concrete elements.

5.5. Numerical shear wall result variability

It is noted in the numerical sensitivity analysis (section 4.5) simulations that sometimes fairly small input changes result in noticeable changes in output (wall response primarily in terms of crack pattern and wall ductility). An increase in shear capacity have for some situations been noted to simultaneously result in a decrease in whole wall ductility, which for some situations may be unfavorable. The working hypothesis for this result variability is that for this quasi-brittle material, the load path and progression over the event is dependent on the formation of initial crack pattern and crack propagation. This variability effect has been noticed on several occasions before, both for experimental and numerical work [8].

5.6. Experimental result variability

Variability in experimental results are not investigated in the test campaign, as only one test specimen of each configuration was tested (see section 2.2). This situation is noted, and experimental data are regarded as indicative only.

5.7. Wall ultimate ductility capacity

The precise determination of the ultimate displacement (ductility measure) is non-trivial, and some criteria should ideally be used for evaluating this parameter. In the evaluations of this parameter within this report, a subjective approach is used, based on when the ultimate diagonal crack is formed. It should be noted that for implicit FE methods, the ultimate displacement capacity is not the same as non-convergence of the solver.

5.8. Boundary conditions

Because of what seems to be a free, almost unrestrained, rotation of the top beam during the experiments, pure shear response of the wall is not achieved at the physical tests. Instead, an in-plane bending motion develop, and a mixed mode failure is obtained. This phenomenon is clear from the boundary condition sensitivity analysis presented in section 4.5.1. The effects from this can easily be implemented in a numerical model, but choosing the correct design code equations to adjust for this response may not be as straight forward.

5.9. Sensitivity analysis

The studied shear load problem is a good example of the benefits of using sensitivity analysis for practical engineering problems. The variability of the problem results has shown that important cliff-edge effects may be discovered using varied input, and using sensitivity analysis are considered to be of good engineering practice.

5.10. CDP material model used

The CDP material model seems to capture the monotonic loading well for this type of shear wall problems. Responses for cyclic loading of this squat wall is however less satisfactory for this shear dominated problem.

The used CDP material model is quite complex, as virtually all other existing non-linear material models, and include several non-intuitive input parameters. When using such a model for practical cases, specialist knowledge is required. In addition, sensitivity analyses may help in understanding the implications of various input options chosen for the specific situation. This may however not be entirely sufficient, and comparative validation examples for the load situations analyzed should preferably be available.

5.11. Requirements on material model input data

It has not been possible, within the work presented in this report, to in detail investigate requirements on experimentally derived material test data and relevant test methods for the material input parameters needed for the used material model. However, it is concluded that well informed decisions need to be made and justified for all material model input parameters. Using experimentally derived material parameters, it is important to be aware of what is an actual material parameter, appropriate as material model input, and what is merely considered to be a material property by force of conventional practice.

5.12. Reinforcement steel modelling

The non-linear response of the reinforcement steel material is modelled in a rough fashion here, using an idealized plastic behavior. This may have a slight effect of the ultimate capacity, and more so on the ultimate ductility. The effects of this is not pursued within the scope of the work presented in this report.

Reinforcement bars are here modelled using bar elements (including bending stiffness), instead of using truss elements (transfer force along element only), as this for some configurations proved to be an important factor for both the crack pattern and ultimate ductility in the numerical wall simulations. Using truss elements consistently resulted in lower ductile capacity for the affected configurations, which is then considered to result in a conservative ductile prediction.

It should also be noted that the bond interaction between the concrete volume and the reinforcement bar model is completely tied together. This may be important for the numerical results, and maybe primarily so for the ASR affected models. The incorporation of bond-slip effects into a numerical model is non-trivial, and not regarded as current common engineering practice.

6. Conclusions

The ability of the Concrete Damaged Plasticity material model in ABAQUS to simulate the behavior of the studied shear wall were investigated, and found to be reasonably adequate in the case of monotonic pushover loading, for the studied shear dominated problem. For a simulation of the reverse loading cyclic event, numerical result comparison to experimental results is however concluded to be less satisfactory. The reason is mainly due to the basic nature of the used material model, which does not mimic the behavior of real-world reinforced concrete well for this type of loading condition, although this approximation has been proven to work well for other loading situations.

It should be noted that only a limited amount of information concerning the experimental test results are known to the ASCET Phase 2 benchmark participants. In addition, due to both the unresolved questions regarding the given experimental results for the reference shear wall specimen (discussed in section 2.6), and unknown interactions and boundary conditions as well as used material model input, it is considered not possible to in full validate that the used numerical model satisfactory reflect the actual experimental test setup.

The research project participation has however resulted in the following observations and conclusions, mainly concerning numerical simulations of the studied squat shear wall:

1. **General:** Not ignoring the statements concerning validation of models in [29], it appears as if the general structural behavior of the numerical model monotonic push over load simulations of the studied shear wall compare well to the limited experimental results available. The maximum shear force capacity of the wall seems to be predicted with better accuracy than the evolution of whole wall force-displacement function. The general response and failure of reinforced concrete shear walls may consequently be simulated with some level of confidence, using similar configurations of finite element analyses. It should be noted that the non-linear shear response of the squat wall studied appear to be quite complex, and sensitive to several of the model input parameters, both material, loads and restraints.

2. **Experimental result comparison:** Numerical simulation results confirm the experimental observation that ASR affected wall specimens, although having nominally weaker material properties, may possess a higher ultimate capacity than a structure with regular concrete material. This appear to be the result of confining effects resulting from the concrete ASR material expansion. Numerical sensitivity studies, based on evenly distributed isotropic material expansion and limited to the studied structure, indicate that the positive confining effects may increase the shear capacity up to material expansion levels beyond the reinforcement steel yield

strain. Experimental validation of this is yet to be confirmed.

3. **Material input:** Due to the very complex structural response of the wall for the shear load, quite different crack patterns, and failure modes, may develop for seemingly small variations in structural or material input. In addition, all of the required material input parameters needed for advanced numerical models are seldom experimentally derived. To further complicate the situation, material tests conventionally used and normally considered to produce material specific parameters, including the characteristics of the material only, must be challenged and investigated if appropriate as numerical material model input. For example, the use of concrete compressive strength from tests on cube specimens in the concrete damaged plasticity constitutive model seems to be most appropriate, for a best estimate simulation of the physical response of concrete structures. This as compressive strength derived from testing of standard cylinder specimen are the combined result of the material and the geometry of the specimen tested. For design code based simulations of actual structures, the conservatively lower cylinder specimen derived values given in the codes should be used. For the example problem studied here, unresolved questions regarding the suitability as numerical model input of the given material properties from material tests, remain. Shear load situations seem to be more sensitive to material input than situations dominated by bending moments. The use of sensitivity studies when numerical simulation tools are used in design situations are recommended.

4. **Ultimate shear capacity:** The wall ultimate shear capacity was consistently underestimated in the numerical monotonic push over simulations, compared to available experimental data. This means that the wall structural capacity may be predicted in a conservative way, as the predicted shear capacity is less than in the experiments. However, using this numerical technique and the concrete damage plasticity material model for dynamic events, where high accelerations are capacity limiting, meaning to derive floor response spectrum for systems and components in nuclear structures, the used technique may result in non-conservative results.

5. **Design code margins:** It is concluded that shear capacity, calculated as per section 6.2.5 in EC2, exceeds the experimentally derived shear capacity of the studied wall.

6. **Boundary conditions:** The global boundary conditions and interactions, as restraints on the top specimen beam, are important to model correctly. Restrained in-plane rotation of the top beam significantly increase structural maximum shear stiffness for the specimen. Allowing in-plane rotations will result in a mixed mode shear and bending failure. Just as for several other parameters which increase the nominal value of the maximum shear capacity, restrained rotations (which increase the maximum shear capacity) cause a more brittle and less ductile whole wall response. No

information concerning the actual experimental conditions are currently available.

7. For **Swedish conditions**, compiled operational experiences [5] for nuclear reactor containments include no instances of suspected or confirmed ASR at units still in operation. Consequently, with current knowledge, AAR related problems should be of no practical concern for nuclear reactor containments in Sweden.

8. **Material model:** The concrete damaged plasticity (CDP) constitutive model in ABAQUS is found to work reasonably adequate for the simulation of the failure modes investigated, for a monotonic pushover load. However, careful specification of the material model input parameters is essential for this shear load situation, to a higher degree than for other types of loading conditions. For reversed load cycles, in combination with progressive non-linear material response, the response and associated plasticity induced swelling of elements appear to produce unphysical results.

9. **Reinforcement modelling:** The sensitivity analysis show that reinforcement modeled using beam elements, as an alternative to truss elements, for some configurations proved to be an important factor for both the crack pattern and ultimate ductility in the numerical wall simulations. Using truss elements consistently resulted in lower ductile capacity for the affected configurations, which is then considered to result in a conservative, less ductile, prediction.

10. **Element type selection:** This section may be particularly specific to element implementations in ABAQUS software. Sensitivity analyses show that 8-node reduced integration brick elements (C3D8R) were inappropriate for the studied in-plane shear dominated problem. This was also concluded to be the case for the 4-node reduced integration shell element (S4R). For these element types, excessive amounts of artificial strain energy resulted from the imposed in-plane shear deformation in the wall. First order four-node tetrahedron elements (C3D4) are usually considered to result in overly stiff structural response, which were confirmed in the elastic range. The 10-node modified tetrahedron element (C3D10M) performed well both in the elastic range, and resulted in conceivable crack patterns, although this has not been possible to in detail confirm with experimental data. The element type was finally considered the better element choice for the simulations. The used characteristic element length was approximately 25 mm for this 100 mm thick wall.

7. Acknowledgement

8. References

[1] OECD/NEA/CSNI, Final Report of ASCET Phase 1, 2016.

[2] N. Orbovic, D. Panesar, S. Sheikh, F. Vecchio, C. Lamarche and A. Blahoianu, "Alkali Aggregate Reaction in Nuclear Concrete Structures, Part 1: A Holistic Approach," Transactions SMiRT-23, Division I, Paper ID 202, Manchester, United Kingdom, August 10-14, 2015.

[3] B. Thunell, "Bedömning av degraderade betongkonstruktioner, Assessment of structures subject to concrete pathologies (ASCET)," SSM publikation 2015:50, Report number: 2015:50 ISSN: 2000-0456, http://www.stralsakerhetsmyndigheten.se/, 2015.

[4] Dassault Systémes, "Abaqus Documentation, Version 6.14," 3DS Simulia, 2015.

[5] B. Thunell, "CONSAFESYS - Barsebäck NPP, Main Project Summary Report," Report SCTE/09416/B1:R-06, Revision 0, 2015-10-20.

[6] J. Tcherner and T. S. Aziz (Atomic Energy of Canada Limited), Effects of AAR on Seismic Assessments of Nuclear Power Plants for Life Extensions, Division 7, Paper 1789, SMiRT 20, Augist 9-14 2009.

[7] Anca-Cristina Jurcut, "Modelling of alkali-aggregate reaction effects in reinforced concrete structures (Master thesis)," University of Toronto, Department of Civil Engineering, 2015.

[8] Saouma, V.E., et al., Effect of alkali–silica reaction on the shear strength of reinforced concrete structural members. A numerical and statistical study, Nucl. Eng. Des. (2016), http://dx.doi.org/10.1016/j.nucengdes.2016.10.012.

[9] A. Farhang, Inverkan av ASR på betongens bärförmåga En litteraturstudie, Energiforsk rapport 2016:256, 2016.

[10] D. Panesar, S. A. Sheikh and F. J Vecchio, "Details of two walls tested under axial load and lateral cyclic excursion," E-DOCS-#5015738-v1-ASCET_Phase_II_Input_Data.pdf, SAS20160605.

[11] D. Panesar, S. A. Sheikh and F. J Vecchio, "Addendum to Report SAS20160605 related to sizes of specimens for material properties," June 26, 2016.

[12] D. Panesar, S. A. Sheikh and F. J. Vecchio, "Mix Design for concrete shear walls," SAS20160609.

[13] B.P. Gautam, D.K. Panesar, S.A. Sheikh, F. J. Vecchio, and N. Orbovic, "Alkali Aggregate Reaction In Nuclear Concrete Structures: Part 2: Concrete Materials Aspects," Transactions, SMiRT-23, Division I, Paper ID 043, Manchester, United Kingdom, August 10-14, 2015.

[14] F. Habibi, S. A. Sheikh, N. Orbovic, D. K. Panesar, and F. J. Vecchio, "Alkali Aggregate Reaction In Nuclear Concrete Structures: Part 3: Structural Shear Wall Elements," Transactions, SMiRT-23 Division I, Paper ID 044, Manchester, United Kingdom, August 10-14, 2015.

[15] A. C. Jurcut, F. J. Vecchio, S. A. Sheikh, D. K. Panesar, and N. Orbovic, "Alkali Aggregate Reaction In Nuclear Concrete Structures: Part 4: Modelling And Analysis," Transactions, SMiRT-23, Division I, Paper ID 045, Manchester, United Kingdom, August 10-14, 2015.

[16] S.A.Sheikh (University of Toronto), Shear Wall Elements (Presentation at ASCET Phase 2 Workshop in Ottawa), May 8 2017.

[17] A. Sellier (Université de Toulouse), V. Saouma (University of Colorado, Boulder), S. Multon (Université de Toulouse), Y. Le Pape (Oak Ridge National Laboratory), N. Orbovic (Canadian Nuclear Safety Commission), "RILEM Technical Committee 259-ISR, ASR Prognosis of deterioration and loss of serviceability in structures affected by alkali-silica reactions, WG 2 Benchmark/Round Robin Analyses," v. 1, January 2016.

[18] Center for Transportation Research at the University of Texas at Austin, Non-Destructive Evaluation of In-Service Concrete Structures Affected by Alkali-Silika Reaction (ASR, or Delayed Ettringite Formation (DEF) - Final Report , Part I, Report FHWA/TX-13/0-6491-1, 2012.

[19] J. Lee and G. L. Fenves, "Plastic-Damage Model for Cyclic Loading of Concrete Structures," Journal of Engineering Mechanics, vol. 124, no.8, pp. 892–900, 1998.

[20] J. Lubliner, J. Oliver, S. Oller and E. Oñate, "A Plastic-Damage Model for Concrete," International Journal of Solids and Structures, vol. 25, pp. 299–329, 1989.

[21] Swedish Standards Institute, SS-EN 1992-1-1:2005, Eurocode 2: Design of concrete structures - Part 1-1: General rules and rules for buildings, 2005 with corrections and national amendments.

[22] M.R.A van Vliet and J.G.M van Mier, Softening behaviour of concrete under uniaxial compression (Proceedings FRAMCOS-2), Stevin Laboratory, Delft University of Technology, 1995.

[23] B. Lagerblad, J. Trägårdh, Alkalisilikareaktioner i svensk betong, ISSN

0346-8340, CBI rapport 4:92.

[24] Swedish Radiation Safety Authority (SSM), "2015:25 Design Guide for Nuclear Civil Structures (DNB)," 2015.

[25] Swedish Standards Institute, SS-EN 1998-1:2004/AC:2009, Eurocode 8: Design of structures for earthquake resistance – Part 1: General rules, seismic actions and rules for buildings, 2013-02-27.

[26] N. Orbovic, et. al., The Capacity of Reinforced Concrete Squat Shear Walls Under Seismic Loading for the Design of the ACR-1000 NPP, Transactions, SMiRT 19, Toronto, August 2007.

[27] ASCE 43-05, "Seismic Design Criteria for structures, Systems and Components in Nuclear Facilities," American Society of Civil Engineers, 2005.

[28] American Concrete Institute, Code Requirements for Nuclear Safety-Related Concrete Structures (ACI 349-13) and Commentary, 2014.

[29] N. Oreskes, K. Shrader-Frechette, K. Belitz, "Verification, Validation, and Confirmation of Numerical Models in the Earth Sciences," Sciense, New Series, Volume 263, Issue 5147 (Februari 4, 1994), 641-646.

2018:17

The Swedish Radiation Safety Authority has a comprehensive responsibility to ensure that society is safe from the effects of radiation. The Authority works to achieve radiation safety in a number of areas: nuclear power, medical care as well as commercial products and services. The Authority also works to achieve protection from natural radiation and to increase the level of radiation safety internationally.

The Swedish Radiation Safety Authority works proactively and preventively to protect people and the environment from the harmful effects of radiation, now and in the future. The Authority issues regulations and supervises compliance, while also supporting research, providing training and information, and issuing advice. Often, activities involving radiation require licences issued by the Authority. The Swedish Radiation Safety Authority maintains emergency preparedness around the clock with the aim of limiting the aftermath of radiation accidents and the unintentional spreading of radioactive substances. The Authority participates in international co-operation in order to promote radiation safety and finances projects aiming to raise the level of radiation safety in certain Eastern European countries.

The Authority reports to the Ministry of the Environment and has around 300 employees with competencies in the fields of engineering, natural and behavioural sciences, law, economics and communications. We have received quality, environmental and working environment certification.